Volume 19
Number 1
7 January 2017
Pages 1-896

PCCP
Physical Chemistry Chemical Physics
rsc.li/pccp

ISSN 1463-9076

PAPER
H.-P. Loock et al.
Determination of the thermal, oxidative and photochemical
degradation rates of scintillator liquid by fluorescence EEM
spectroscopy.

ROYAL SOCIETY
OF CHEMISTRY

This is an Accepted Manuscript, which has been through the Royal Society of Chemistry peer review process and has been accepted for publication.

Accepted Manuscripts are published online shortly after acceptance, before technical editing, formatting and proof reading. Using this free service, authors can make their results available to the community, in citable form, before we publish the edited article. We will replace this Accepted Manuscript with the edited and formatted Advance Article as soon as it is available.

You can find more information about Accepted Manuscripts in the Information for Authors.

ROYAL SOCIETY
OF CHEMISTRY

rsc.li/pccp

PCCP

ARTICLE TYPE

Development of Discrete Interaction Models for Ultra-fine Nanoparticle Plasmonics†

Lasse K. Sørensen,^{a,b} Valeriy S. Gerasimov,^{c,d} Sergey V. Karpov,^{e,c} and Hans Ågren^{f}

Plasmonics serves as a most outstanding feature of nanoparticle technology and is nowadays used in numerous applications within imaging, sensing and energy harvesting, like plasmonically enhanced solar cells, nanoparticle bioimaging, plasmon-controlled fluorescence for molecular tracking in living cells, plasmon-controlled electronic molecular devices and surface enhanced Raman spectroscopy for single molecular detection. Although plasmonics has been utilized since ancient times, the understanding of its basic interactions has not been fully achieved even under the emergence of modern nanoscience. In particular, it has been difficult to address the "ultra-fine" $1-10$ nm regime, important for applications especially in bioimaging and biomedical areas, where neither classical nor quantum based theoretical methods apply. Recently, new approaches have been put forward to bridge this size gap based on semi-empirical discrete interaction models where each atom makes a difference. A primary aim of this perspective article is to review some of the most salient features of these models, and in particular focus on a recent extension – the extended discrete interaction model (Ex-DIM), where the geometric and environmental are extended, - and highlight a set of benchmark studies using this model concerning size, shape, material, temperature dependence and other characteristics of ultra-fine plasmonic nanoparticles. We also analyze new possibilities offered by the model for designing ultra-fine plasmonic particles for applications in the in the areas of bioimaging, biosensing, photothermal therapy, infrared light harvesting and photodetection. We foresee that future modelling activities will be closely connected to collaborative experimental work including synthesis, device fabrication and measurements with feedback and validation in a systematic fashion. With this strategy we can expect that modelling of ultra-fine plasmonics particles can be integrated in the development of novel plasmonic systems with unprecedented performance and applicability.

1 Introduction

Few scientific endeavors have transformed our perception of nature like the development of nanotechnology. Materials structured at the nanoscale possess unique physicochemical attributes and provide unprecedented capabilities that nowadays are exploited in many important societal areas, like healthcare, environmental research and energy conversion. Much of the success of nanotechnology can be traced to two outstanding properties of nanoparticles: quantum confinement, leading to discrete energy states — quantum dots, and the ability to support collective electron oscillations — plasmons. The localization of the strong local fields is associated with collective electron excitations generating surface plasmon resonances (SPR) that depend on the geometric properties of the particles[1]. Plasmonics or plasmonic field enhancement serves as the most outstanding feature of nanoparticle technology and is nowadays used in numerous applications for imaging, sensing and energy harvesting, like plasmonic enhanced solar cells, nanoparticle bioimaging, plasmon-controlled fluorescence for molecular tracking in living cells, plasmon-controlled electronic molecular devices, and surface enhanced Raman spectroscopy for single molecular detection, to mention a few out of many examples. Plasmonic enhancement of the incoming electromagnetic field also offers a great opportunity to substantially increase the efficiency of light conversion nanoparticles. Nanoplasmonics plays a crucial role as a means to produce concentration of optical energy at the nanoscale as localized surface plasmon os-

^{a} *Department of Physics, Chemistry and Pharmacy, University of Southern Denmark, Odense M DK-5230, Denmark; E-mail: lasse.kragh.soerensen@gmail.com*

^{b} *University Library, University of Southern Denmark, DK-5230 Odense M, Denmark; E-mail: laks@bib.sdu.dk*

^{c} *International Research Center of Spectroscopy and Quantum Chemistry, Siberian Federal University, Krasnoyarsk, 660041, Russia.; E-mail: valkrsk@gmail.com*

^{d} *Institute of Computational Modelling, Federal Research Center KSC SB RAS, Krasnoyarsk, 660036, Russia.*

^{e} *L. V. Kirensky Institute of Physics, Federal Research Center KSC SB RAS, Krasnoyarsk, 660036, Russia.; E-mail: sergei.v.karpov@gmail.com*

^{f} *Department of Physics and Astronomy, Uppsala University, Box 516, SE-751 20 Uppsala, Sweden.; E-mail: hans.agren@physics.uu.se*

cillations and integrated plasmonic functionality provides various mechanisms for manipulating the optical response of engineered materials[2–4].

The optical properties of colloidal metal nanoparticles have been extensively reviewed and it has been shown that custom tailoring of optical properties requires relatively inexpensive manipulation of size, shape and composition of plasmonic nanoparticles[1,5]. Plasmonic materials of metal elements that are nanostructured can generate very strong electric fields in their vicinity through the interaction with electromagnetic radiation, leading to the possibility of detecting signals of single molecules on the nanoparticle surface. There is a need for matching the frequency of the incident light with that of the oscillating surface electrons that in turn, depends on electronic structure, and thereby also on the size, shape, and material or alloy of the nanoparticles. The important aspect is here the combination of a giant enhancement of the electromagnetic fields generated by nanoparticles and their strong localization. Plasmonic nanoparticles have therefore been frequently employed as modifiers of the optical properties of various optically sensitive objects and materials, such as molecules, their aggregates, and quantum dots.[6] At the same time, the properties of localized plasmons critically depend on the shape of the nanoparticles, which makes it possible to tune their resonance system to interact effectively with light or other elementary quantum objects. Such properties have enabled the discovery of a number of new effects associated with plasmonic nanoparticles. For instance, giant local fields near nanoparticles result in an increase in the Raman cross section by 10–14 orders of magnitude, making it possible to observe individual molecules and to determining their structure[7,8]. Plasmonic nanoparticles provide simultaneous enhancement of both extinction and emission of light and, thus, make up for effective fluorophores and nanoscale light sources, including nanolasers[9–13].
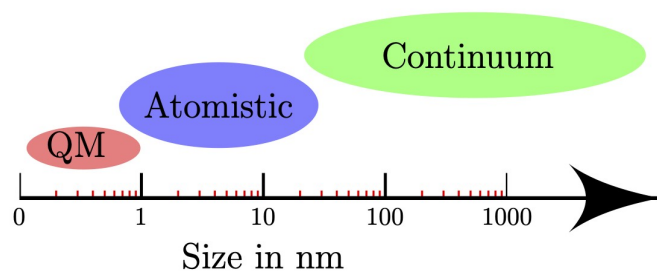

Fig. 1 Size range of applicability of quantum mechanical (QM), Atomistic models and classical continuum methods.

The plasmonic optical response thus depends on the material, the shape and the size of the nanoparticle, something that can be used to tune the optical properties of a molecular dye located in the vicinity of the surface of the metallic particle. The locally enhanced fields are the basis for increasing the sensitivity of spectral methods for determining the chemical composition of impurity materials up to the level of single molecules. This fact also lays the basis for a number of applications in bioimaging[14–16], nanosensing[7,8,17,18], nanophotonics[19–21] and medicine[22–26], see

also reviews by Halas[27] and Linic et al.[28]. An additional important characteristics of plasmonic nanoparticles is that the localized surface plasmon wavelength relates also the characteristics of a surrounding medium, a factor that can be used in, e.g., refractive index sensitivity measurements for biosensing.

The applications alluded to above have been greatly boosted by the advance in synthesis procedures which have made it possible to control the variation of shape, size of particles and their material content[29]. Traditional technologies based on colloidal systems for the chemical synthesis of nanoparticles, have been complemented by fabrication by pulsed laser ablation of bulk materials in liquid media, and in gaseous media by synthesis of self-organizing nanoparticles making it possible to fabricate nanoparticles upon their deposition on a substrate[30–33]. Moreover, fabrication of nanoparticles and synthesis of periodic arrays is now possible by both sputtering onto a substrate from the gas phase through nanomasks and by directional etching of various shapes on the faces of single-crystal samples[34–37]. The tuning of plasmonic properties are well-known for larger particles (> 20 nm); red shifting deep into the infrared region can easily be manipulated by just adjusting size, blue shifting is more challenging but can be introduced by alloying[38,39], while field anisotropy and multiple resonances can be introduced by using non-spherical particles with different aspect ratios[40], the simplest case is here nanorods[40]. An important concept is the ultra-strong field enhancement in terms of so-called "hot spots" can be triggered by field concentrations at sharp edges[41,42]. This is, for example, utilized in scanning tunneling microscopy (STM) where the plasmon fields are mostly located at the very top of the tips creating there an ultra strong field enhancement[43]. All these aspects, which thus are supported by modern controlled synthesis, have opened important perspectives in terms of optical applications in a wide wavelength range.

From a theory or modeling point of view, the great challenge is to find quantitative forms of relationships between structure and plasmonic properties, that is structure-property relationships. This would further promote the possibilities of designing plasmonic nanoparticles for a specified purpose and so to boost the utility of nanoparticle plasmonics for applications like detection, sensing and imaging. Modeling, with experimental feedback and validation, has indeed boosted the utility of plasmon techniques, however, it still remains a great challenge to design active plasmonic nanomaterials with arbitrary size, composition and structure. Classical electrodynamics methods serve in general as viable approaches for prediction of the optical properties, including plasmonic generation[44–46]. One can here identify here a variety of approaches where perhaps the most commonly used one is the is FDTD — the Finite Difference Time Domain method — a numerical approach which applies finite element propagation of the time-dependent Maxwell's equations[47] and FEM – the Finite Element Method – which has frequently been used for both time- and frequency-domain calculations. The FEM has been implemented in the package COMSOL Multiphysics[48] among many commercial solvers. A combination of both the FDTD and the FEM retaining the advantages has been introduced, based on a variation of the so-called Galerkin method[49]. These methods have

been applied in several contexts, e.g. for designing plasmonic metal shells of quantum dot nanoparticles, to enhance the electromagnetic field either inside to strengthen absorption, or for enhancing the field outside for the purpose of sensing, and of course for surface enhanced Raman scattering. Furthermore, Mie theory[44] is frequently used for scattering problems involving nanoparticles that are sufficiently large that the concept of a classical dielectric constant remains valid. Other classical electrodynamics methods, such as the discrete dipole approximation or coupled dipole approximation[45] and T-matrix method[46] have also been widely useful for calculation optical properties of nanospheres, nanodiscs, nanorods and other complex geometrical configurations. A popular approach in modeling the dielectric constant of metal for subsequent calculation of the plasmon absorption spectra of nanoparticles is the Drude[50] model, applicable for a finite metal spherical cluster much smaller than the wavelength of light. For very small sizes, towards the ultra-fine region considered in this review, there are abundant contributions to what might be called mesoscopic electrodynamics[51–53]. Here the concept of electron spill-out[54] has been frequently applied with extensions to account for size-dependent damping and the self-consistent interplay between screening and spill-out. Furthermore, various modified Drude models for the non-local effects have been put forward, for instance the nonlocal hydrodynamic Drude model of electron gas[55]. Also semiclassical non-local optical response theory has a been advocated in the framework of hydrodynamic models, that involve induced charge diffusion kinetics as well as quantum pressure effects[56].

The efficiency of the above mentioned methods has been confirmed many times, nevertheless there are losses in accuracy for small particles with a diameter less than 12 nm and where quantum size effects[57] can play a crucial role. While some corrections for these models that take into account the quantum size effects improve the results, these methods still use the dielectric constants of bulk materials, obtained empirically[58], and do not consider the discrete atomic structure of the nanoparticles. It is thus obvious that the dielectric constant will vary with size and become unpredictable for small clusters with broad plasmon resonances or for clusters with more complex shapes. Here the particle size can be smaller than the mean free path of the conduction electrons and the surface to volume ratio can become so large that significant deviations from a non-local, bulk value, description of the dielectric constant can be expected. All these methods rely on the principles of classical electrodynamics and have limited applicability to smaller nanosystems with pronounced quantum size effects[57,58]. In the continuous medium models the classical approach to accounting for quantum size corrections to the dielectric constant of spherical metal nanoparticles was formulated in Kreibig's early works by incorporating the size-dependent contribution of the surface scattering effects in the electron damping constant as follows $\Gamma(R) = \Gamma^{(bulk)} + A v_F / R$. Here v_F is the Fermi velocity, R is the particle radius, A is the numerical parameter that is adjusted to take into account the particle surface properties, usually taken equal to 1.

It is clear that there is a breaking point in size where quantum mechanics based descriptions, accounting also for electronic

structure, are necessary and where classical electrodynamics becomes too crude. Full quantum methods, such as the time-dependent density functional theory (TDDFT), can be useful for calculating the absorption spectra of small clusters of noble metal with the number of atoms $N \approx 10 - 20$[59,60]. Plasmon oscillations have accordingly been addressed for noble-metal clusters [61] and charged gold clusters[62] using TDDFT. However, due to obvious limitations for first-principles calculations, they can not be performed for a large number of atoms. Thus, to calculate the optical properties of particles with $N > 10^6$ and diameter of particle $d < 10$ nm it is necessary to use complex methods. If the all electronic degrees of freedom explicitly considered in an *ab initio* treatment the scalability is drastically reduced. For the smallest clusters, up to 20–30 atoms, very accurate multi-configurational self-consistent field and coupled cluster methods can provide a reference state for time-dependent perturbation theory, for instance linear response theory in the form of the equation-of-motion coupled cluster (EOM-CC) method[63] or the Bethe-Salpeter equation[64]. These, very accurate methods also make it possible for a hierarchical assessment between models that converge to the final spectrum without referring to experiment. However, the particle sizes are too limited to generate strong plasmon excitations, and definitely too small to explore the their size-convergence. TDDFT based methods[65,66] cannot be applied in such a convergent manner since there are no formal relations between the functionals used, but can on the other hand reach considerably larger clusters than the pure *ab initio* methods. With modern density functional theory methods, using more advanced functionals, it is a realistic proposition to treat clusters of the size that show strong plasmonic excitations. Here, any type of symmetry or periodicity in the cluster reduces the computational effort. As even small metal clusters often show multiple conformations and energy minima with low transition state barriers an integrated dynamical approach that couples (quantum or classical) dynamics to the quantum spectral calculations becomes almost mandatory. The development of pure quantum methods towards larger systems is rapidly expanding, including linear scaling technology. An example is the work of Nobusada and coworkers who in a series of paper developed and applied a highly efficient first principles TDDFT computational program for electron dynamics solved in real-time and real-space (a coupled Schrödinger-Maxwell approach), thereby reaching optical response of gold clusters with more than 1000 atoms, including plasmonic excitations, though never being close to the accuracy seen for classical methods on large particles. One can here emphasize orbital-free DFT as a powerful DFT variant for plasmonics[67,68]. A few direct comparisons between classical atomistic models and TDDFT have been reported, as an example we can here mention the work of Giovanni et al[69] showing a favorable comparison of results from their ωFQ model with TDDFT for large clusters in the 1000 atom range. As an intermediate, the jellium model can be joined with density functional theory where the ionic background charge of the particles is replaced by a uniform charge density[70]. When implemented with the so-called time-dependent local density approximation form of DFT, it can treat large clusters. In this case a meaningful comparison with pure

classical results can be obtained. The jellium model thus introduces significant simplifications for quantum mechanical calculations of plasmonics. It is here notable that DFT and TDDFT has been implemented together with plasmonic models (n.b. discrete interaction models) in the form of QM/MM, thus as DFT/DIM or TDDFT/DIM. Here TDDFT is applied to simulate properties in the DIM plasmonic fields, like surface-enhanced Raman optical activity[71], plasmonic circular dichroism[72], surface-enhanced hyper-Raman scattering[73] and two-photon absorption[74].

It thus still remains a great challenge to design active plasmonic nanoparticles with arbitrary size, composition and structure in the "ultra-fine" region with the dimension of a few nanometers. This situation has been unfortunate considering the great number of applications such particles bring about, for instance in the bioimaging and biomedical areas where ultra-fine plasmonic particles provide a number of distinct advantages like size compatibility of small clefts, pockets and other compartments of the target biostructures. They can more easily pass though membrane channels and can, moreover, be effectively cleaned in kidney and rinsed from the body. This alleviates, although not removes, the nanotoxicity problem of using nanoparticles for in-vivo studies and is especially important when using them as a part of complex therapy of oncological diseases and during early diagnosis of disease.

In this perspective article we will review recent work addressing the lower nanoscale region for plasmonic nanoparticles, where classical bulk models have limited applicability or where the particles are yet too large for quantum mechanics, so that the gap between classical and quantum treatments for plasmonic particles potentially can be closed. This is accomplished by implementing atomistic models for plasmonic excitation and optical properties of metallic nanoclusters, which are parameterized using quantum chemical calculation results as well as empirical results for larger clusters. The models are based on a general atomistic complex polarizability parameterization of the metal atoms, where the atomistic parameters are obtained from a mix of experimental data and classical models. The atomistic parameters can be made local environment dependent by introducing explicit atomistic parameter dependence on atom coordination number, and by introducing explicit induced dipole-induced dipole interaction tensor on atoms types. In the extended discrete interaction model (Ex-DIM)[75] the total optical properties, the complex polarizability and the plasmonic excitation of a cluster is atomically dependent, and therefore dependent on arbitrary composition and geometric characteristics of the cluster. Calculations for the full polarizability and optical spectrum, including plasmonic resonances, are made with and without the topology awareness of the parameters and compared, for small clusters, with *ab initio* data. The role of size, form shape, aspect ratios, and other geometric factors, down to the atomic level, is explored in order to design plasmonic particles with particular strength and field distribution. It follows that the model makes it possible to do such calculations also for any alloy composition of the constituting metal elements as also shown in this review. The model is at present practically implementable for clusters also above 10 nanometers thus covering a significant part of the gap between the scales where pure

quantum calculations are possible and where pure classical models based on the bulk dielectric constant apply. Before outlining the discrete interaction models, it is here relevant to mention the existence of other atomistic models based on different physical backgrounds, like the frequency-dependent Fluctuating Charges model (ωFQ) first proposed by Giovannini et al.[76] which is based on the Drude model of conduction and describes the plasmonic response in terms of classical charges only.

In the following section we review some basic elements of discrete interaction models addressing merits and limitations. We then present the Ex-DIM and give a survey of its applications. Finally, we highlight some of the important results and make an outlook for future research possibilities using the proposed approach.

2 Discrete Interaction Models

For intermediate-sized clusters an atomistic approach, where the polarizability can be obtained from the atoms of the particle, could fill an important gap in the description of nanoparticle plasmons between the quantum and classical extremes. Here, the classical dipole approximation can be applicable, since it can be used to construct the total polarizability (or the dielectric constant) from a set of interacting, complex polarizable, atomic dipoles.[69,77–83] However, the polarizability is represented by fixed constants for each type of chemical element, obtained either from bulk measurements or electronic structure calculations. This neglects, e.g., any charge rearrangement that takes place in the real cluster, on formation or by a molecular sensitization. An obvious complication of a metallic particle is the almost free motion of charges within the metallic cluster, and that the interaction with a surrounding should regulated by the "atomic capacitance" rather than by fixed charges. An elaborate model to deal with this, but yet very simple compared to quantum chemical calculations, is the so-called interaction model[84]. In simplest form it is a set of atomic polarizabilities that interact in accordance with classical electrostatics without external electric field. This model has been significantly expanded by inclusion of a damping term of the internal electric field[85,86] extended also to the frequency dependence of the dipole polarizability[87,88] and capacitance-polarizability interaction model (CPIM)[89]. One of the significant drawbacks of interaction model is, however, that the atoms on the surface and inside of the cluster do not differ very much. In order to differentiate between surface and bulk atoms a coordination number can be assigned to each atom in the cluster[90,91]. The coordination number will have an effect on the distribution of the charge density around every atom, depending on it's geometric position in the cluster. The charge density will be slightly compressed for atoms inside of the cluster, and slightly stretched for atoms on the surface. Here atomic parameters can be optimized for small clusters and interpolated for bigger systems.

The aim of the discrete interaction model (DIM) has been to describe the polarizability and optical properties of small to large molecules, metallic nanoparticles and carbon nano-structures by representing the nanoparticle as a collection of interacting atomistic charges and dipoles. We note that the DIM can be gen-

eralized to include higher order moments such as quadrupole moments where also higher order hyperpolarizabilities are included. Including higher order terms, however, increases both the complexity of fitting and computational demand of the DIM significantly.[92,93] We therefore here only review the DIM's using charges and dipoles.

The starting point of most DIM's used[69,75,77–83,87,89] are the energy expression Lagrangian for interacting fluctuating charges and dipoles in an external electric field subject to a charge equilibration constraint

$$
\begin{aligned}
L[\{\mu, q\}, \lambda] = {} & E[\{\mu, q\}] - \lambda \left(q^{tot} - \sum_i^N q_i \right) \\
= {} & \frac{1}{2} \sum_i^N q_i \mathbf{c}_{ii}^{-1} q_i + \frac{1}{2} \sum_i^N \sum_{j \neq i}^N q_i \mathbf{T}_{ij}^{(0)} q_j \\
& + \frac{1}{2} \sum_i^N \mu_i \alpha_{ii}^{-1} \mu_i - \frac{1}{2} \sum_i^N \sum_{j \neq i}^N \mu_i \mathbf{T}_{ij}^{(2)} \mu_j \\
& + \sum_i^N q_i \mathbf{V}^{ext} - \sum_i^N \mu_i \mathbf{E}^{ext} \\
& - \sum_i^N \sum_{j \neq i}^N \mu_i \mathbf{T}_{ij}^{(1)} q_j - \lambda \left(q^{tot} - \sum_i^N q_i \right).
\end{aligned}
\tag{1}
$$

q_i is the fluctuating charge assigned to the i-th atom, μ_i is the fluctuating dipole assigned to the i-th atom, the $\mathbf{c}_{ii}$ is the i-th charge self-interaction tensor, the α_{ii} is the i-th dipole self-interaction tensor, the $\mathbf{T}_{ij}^{(0)}$, $\mathbf{T}_{ij}^{(1)}$, and $\mathbf{T}_{ij}^{(2)}$ are the electrostatic interaction tensors, $\mathbf{V}^{ext}$ is the external scalar potential, $\mathbf{E}^{ext}$ is the external time-independent electric field, q^{tot} is the total charge of the nanoparticle, λ is the Lagrangian multiplier and N is the number of atoms.

The first line in Eq. 1 describes the self-interaction energy of fluctuating charges and the interaction energy between fluctuating charges, respectively. The second line contains the self-interaction energy of fluctuating dipoles and the interaction energy between fluctuating dipoles in that order. In the third line the interaction energy between fluctuating charges and the external potential along with the interaction energy between fluctuating dipoles and the external field listed. The last line describes the interaction energy between fluctuating charges and dipoles and in the last term the charge equilibration condition is expressed via the Lagrangian multiplier λ.

The exact expression for the electrostatic interaction tensors $\mathbf{T}_{ij}^{(0)}$, $\mathbf{T}_{ij}^{(1)}$, and $\mathbf{T}_{ij}^{(2)}$ depends on how the charges and dipoles are represented and discussed in Sec. 2.3. The external scalar potential $\mathbf{V}^{ext}$ can be determined from the external electric field $\mathbf{E}^{ext}$ and the choice of gauge. The self-interaction tensors $\mathbf{c}_{ii}$ and α_{ii} are model specific and the expression for α_{ii} is discussed in greater detail in Sec. 2.2 and for the Ex-DIM in Sec. 3. The effect of the different terms on the spectra from particles with different geometries will be discussed in Sec. 3.4.2.

The minimization of the energy $E[\{\mu, q\}]$ in which the fluctuating charges and dipoles are determined can be cast into a matrix

problem of solving a set of linear equations[89]

$$
\begin{pmatrix} \mathbf{A} & -\mathbf{M} \\ -\mathbf{M}^T & -\mathbf{C} \end{pmatrix} \begin{pmatrix} \mu \\ \mathbf{q} \end{pmatrix} = \begin{pmatrix} \mathbf{E}^{ext} \\ \mathbf{V}^{ext} \end{pmatrix}.
\tag{2}
$$

The column vector μ, in Eq. 2, is the collection of N atomic dipoles μ_i and the column vector $\mathbf{q}$ is the collection of N atomic charges q_i with the constraint of the charge equilibration condition. The matrix elements of $\mathbf{A}$, $\mathbf{C}$, and $\mathbf{M}$ matrices are defined as

$$
\begin{aligned}
\mathbf{A}_{ij} &= \delta_{ij} \alpha_{ij}^{-1} - (1 - \delta_{ij}) \mathbf{T}_{ij}^{(2)}, \\
\mathbf{C}_{ij} &= \delta_{ij} \mathbf{c}_{ij}^{-1} + (1 - \delta_{ij}) \mathbf{T}_{ij}^{(0)}, \\
\mathbf{M}_{ij} &= (1 - \delta_{ij}) \mathbf{T}_{ij}^{(1)}.
\end{aligned}
\tag{3}
$$

where $\mathbf{A}$ describe the interaction between the fluctuating dipoles, $\mathbf{C}$ the interaction between the fluctuating charges and $\mathbf{M}$ the interaction between the fluctuating dipoles and charges. The numerical solution to Eq. 2 will be discussed in more detail in Sec. 2.1.

The DIM's are flexible models so a DIM which only involve charges[77]

$$
-\mathbf{C}\mathbf{q} = \mathbf{V}^{ext}
\tag{4}
$$

or dipoles[75,94]

$$
\mathbf{A}\mu = \mathbf{E}^{ext}
\tag{5}
$$

are frequently used. All elements in Eqs. 4 and 5 are defined in Eqs. 2 and 3.

The polarizability of the nanoparticle can be computed from the derivative of $E[\{\mu, q\}]$ with respect to external field $\mathbf{E}^{ext}$.[89,95] The polarizability of a nanoparticle is defined as

$$
\alpha^{np} = \sum_i^N \frac{\partial \mu_i}{\partial \mathbf{E}^{ext}} = \sum_i^N \alpha_i,
\tag{6}
$$

which is the sum of the individual atomic polarizability α_i.

The above described scheme for determination of the polarizability is generic and has been employed in the original, co-ordination dependent and extended discrete interaction models[1,69,74,75,77–83,85–87,88,88,94–98]. Model differences originate from the functional form employed to describe the fluctuating charges and dipoles and from the parameterization of the self-interaction and electrostatic interaction tensors.

2.1 Scaling considerations for linear equations

Eqs. 2,4 and 5 are all examples of linear systems

$$
\mathbf{A}\mathbf{x} = \mathbf{b}
\tag{7}
$$

where the simplest solution is the inversion of $\mathbf{A}$. The inversion of $\mathbf{A}$ is, however, only possible for small systems since the inversion scales as m^3, where m is the dimension of $\mathbf{x}$.

For larger systems iterative approaches scaling as m^2 are needed. Here the conjugate gradient method, Generalized Minimal Residual iteration, Minimum Residual iteration along with

other methods can be used. We here found that the conjugate gradient method from Scipy was very slow to converge, if at all, but found the LGMRES algorithm [99], which is a modified version of the Generalized Minimal Residual iteration from Scipy, both fast and robust in converging for the Ex-DIM. The Fast Fourier Transform (FFT) methods used in the Discrete Dipole Approximation is in general not applicable since the geometries used in the Ex-DIM are often taken from molecular dynamics simulations where there are no perfect lattices. [45] Combined with the distinction between surface and bulk atoms, which will be discussed in Sec. 2.3.2, where the individual dipoles will differ slightly limits methods based on symmetry of the lattice.

For very large systems the relay matrix in Eq. 2 will either have to be constructed on the fly or created using sparse matrix algebra. In the sparse matrix approach the screening of the relay matrix will typically be on distance or interaction strength, where the latter is used in the Ex-DIM. [98] The best effect of the sparse matrix algebra is seen in 1- and 2D systems like rods and thin films whereas 3D systems like spheres the savings from sparse matrix screening are less effective.

The system size that can be reached by the DIM's are also very dependent on the order of the moments included. For a charges only DIM, as seen in Eq. 4, the dimension of m is N, where N is the number of charges. In the dipole only moments DIM, see Eq. 5, $m = 3N$ while in the charge and dipole DIM, see Eq. 2 $m = N + 3N$. Including quadrupole moments adds an additional $9N$ to m. From these scaling considerations of the Relay matrix it is seen that the maximum number of atoms in a given system drops by about a magnitude every time a higher order moment is included. Very large systems, where computational memory considerations have to be taken into account, for the charge, dipole and quadrupole moments models are approximately $+500.000$, $+50.000$ and $+5000$ atoms, respectively, depending on the computational hardware available.

2.2 Representation of the polarizability

The representation of the polarizability usually follows one of two methods. Either the frequency dependent polarizability is computed from experimental values of the dielectric constant or from the simulation of the polarizability from a Lorentz oscillator model.

Lorenz and Lorentz showed that the refractive index of a material can be directly related to the polarizability of the individual atoms through a simple relation

$$\frac{n^2 - 1}{n^2 - 2} = \sum_i \frac{N_i \alpha_i}{3\varepsilon_0} \tag{8}$$

where n is the refractive index, N_i is the number of atoms per volume i, α_i the mean polarizability of the atoms in volume i and ε_0 the permittivity of free space. Usually the Clausius-Mossotti relation, which relates the dielectric properties and the atomic polarizability, is used

$$\frac{\varepsilon_r - 1}{\varepsilon_r - 2} = \sum_i \frac{N_i \alpha_i}{3\varepsilon_0} \tag{9}$$

where ε_r is the dielectric constant. The coordination-dependent discrete interaction model (cd-DIM) from Chen *et al.* [95] is an example of a DIM method which uses the Clausius-Mossotti relation to compute the frequency dependent polarizability. The clear advantage of the experimental values of the frequency dependent dielectric constant is the very wide frequency range for different atoms where these measurements are available. The disadvantage for small particles is the difficulty in creating size-, temperature- and media-corrections since the frequency dependent dielectric constant are bulk values at fixed temperature and media.

The dielectric function from the a Lorentz oscillator model can describe a resonance where the complex dielectric function is given by

$$\varepsilon(\omega) = 1 + \frac{4\pi N e^2}{m} \frac{1}{\omega_0^2 - \omega^2 - i\Gamma\omega} \tag{10}$$

where $\frac{4\pi N e^2}{m} = \omega_p^2$ and ω_p is the plasma frequency, ω_0 the resonance frequency and Γ the relaxation constant. N is the density of charges, e the elementary charge and m the effective mass of a charge. The polarizability of a single Lorentz oscillator is given by

$$\alpha(\omega) = \frac{e^2}{m} \frac{1}{\omega_0^2 - \omega^2 - i\Gamma\omega}. \tag{11}$$

The disadvantage of modelling the polarizability of the individual sites is the limitation in the frequency range. This can be overcome by adding more Lorentzian oscillators which extends the frequency range though each of these oscillators will then have to be fitted. The clear advantage of modelling the polarizability is that it is easy to add size-, temperature- and media-corrections.

2.3 Representation of charges and dipoles

We will here briefly review the two most common ways to mathematically represent the fluctuating charges and dipoles. The charges and dipoles are meant to represent the individual constituents of the physical system irrespective of the composition of the constituents. This means that these charges and dipoles should be able to describe an aggregate of unit cells, atoms and all the way down to individual atoms.

The interaction tensor of order n is in general defined as the n-th derivative of the charge interaction or some other charge distribution

$$\mathbf{T}^n = \nabla_{\mathbf{r}} \mathbf{T}^{n-1}. \tag{12}$$

This definition of the n'th order interaction means that the dipoles and higher orders will be described as exactly overlapping charge distributions of opposite charge that can be polarized. This physical description of the charge distribution of the individual constituents from Eq. 12 therefore comes closer to aggregates than atoms. For aggregates the physical charge distribution is more evenly distributed over the space of the individual constituents than for atoms since atoms are made of two spatially distinct charge distributions, one from the very localized charge distribution of the nuclei and one for the large and more diffuse charge distribution of the electrons, while these atomic charge distribution evens out over larger aggregates.

2.3.1 Thole damping of point charges

The initial approach to represent charges and dipoles in the DIMs was to consider point particles. In the physical picture of the point particle DIM the charges are monopoles and the dipoles are thought to be built up from two infinitesimally shifted monopoles.[86] This representation can unfortunately lead to infinite polarizabilities when the distance r between two dipole approaches $(4\alpha_p\alpha_q)^{1/6}$, where α_p and α_q are the polarizability of site of site p and q respectively.[100] In order to eliminate the problematic behaviour of the polarizability Thole modified the interaction tensor $T^{(2)}$ with a shape function which was independent of the sites p and q. As Thole noted, the modification of the interaction can also be thought of going from the point particles to modelling of the charge distribution $\rho(r)$.

Since it is not evident which well behaved charge distribution shape $\rho(r)$ that represents molecular systems best Thole tried several different charge distributions of which two survived[86]:

$$\rho(u) = \begin{cases} \frac{3(a-u)}{\pi a^4} & u < a, \\ 0 & u \geq a \end{cases} \tag{13}$$

$$\rho(u) = \frac{a^3}{8\pi}\exp[-au], \tag{14}$$

where $u = r_{ij}/(\alpha_i\alpha_j)^{1/6}$ and α the polarizability of i and j, respectively. Both the linear charge distribution in Eq. 13 and exponentially decaying charge distribution in Eq. 14 have shown good numerical results and are actively used today.[101–105]

2.3.2 Gaussian electrostatics

The Gaussian charge representation from Mayer[106,107] have also gained popularity in numerous methods and codes including the Ex-DIM.[75,94,95,108] We will here use normalized Gaussian charge distributions which depend on the local environment of the atoms as defined from the coordination number dependent radius a_{cn}

$$G(\mathbf{r};f_{cn},\mathbf{C}) = \left(\frac{a_{cn}}{\pi}\right)^{3/2}\exp[-a_{cn}(\mathbf{r}-\mathbf{C})^2]. \tag{15}$$

The inclusion of the coordination number is intended to give a better description not only of surface and bulk atoms but also for surface atoms for structures with more complex surface topology where the electronic charge is less confined. The coordination number of atoms in a rod is shown in Fig. 4 where it is clearly seen that the atoms on the surface are not all treated the same but are dependent on the number of close neighbors.

The chemical environment radius a_{cn} is defined as

$$a_{cn}(f_{cn}) = r_{atom}\left(1 - \frac{f_{cn}}{12}\right) + r_{bulk}\frac{f_{cn}}{12}, \tag{16}$$

which regulates the charge distribution radii of the atom depending on the coordination number f_{cn} from the atomic radii r_{atom} to the bulk radii r_{bulk}. Both r_{atom} and r_{bulk} are tabulated.

In the Ex-DIM the Grimme[59] scheme is used where the atomic coordination number f_{cn}^i is computed as

$$f_{cn}^i = \sum_i^N\sum_{j\neq i}^N\left[1 + exp[-k_1(k_2(R_i^{cov}+R_j^{cov})/r_{ij}-1)]\right]^{-1}, \tag{17}$$

where R_i^{cov} and R_j^{cov} are the scaled covalent radius of the i-th and j-th atoms, respectively, r_{ij} is the distance between the i-th and j-th atoms, k_1 and k_2 are empirical parameters equal to 16.0 and 4.0/3.0, respectively.[90] Since the coordination number is not a measurable quantity several other definitions exists which all differs slightly.[109]

The electrostatic interaction tensors, $\mathbf{T}_{ij}^{(0)}$, $\mathbf{T}_{ij}^{(1)}$, and $\mathbf{T}_{ij}^{(2)}$ from two Gaussian charge distributions, $G(\mathbf{r};f_{cn},\mathbf{C})$ and $G(\mathbf{r}';f_{cn}',\mathbf{D})$ centred on the i-th and j-th atoms with position vectors $\mathbf{C}$ and $\mathbf{D}$, following A. Mayer[107], can be computed as

$$\mathbf{T}_{ij}^{(0)} = \int\int\frac{G(\mathbf{r};f_{cn},\mathbf{C})G(\mathbf{r}';f_{cn}',\mathbf{D})}{|\mathbf{r}-\mathbf{r}'|}d\mathbf{r}'d\mathbf{r} = \frac{erf(\gamma r_{ij})}{r_{ij}} \tag{18}$$

$$\gamma^{-1} = \sqrt{a_{cn}^2+a_{cn}'^2} \text{ and } r_{ij} = |\mathbf{C}-\mathbf{D}|.$$

From the derivate of $\mathbf{T}_{ij}^{(0)}$ the higher order electrostatic interaction tensors, $\mathbf{T}_{ij}^{(1)}$, and $\mathbf{T}_{ij}^{(2)}$, can be derived

$$\mathbf{T}_{ij}^{(1)} = -\nabla_{\mathbf{r}_i}\mathbf{T}_{ij}^{(0)} = \frac{\mathbf{r}_{ij}}{r_{ij}^3}\left[erf(\gamma r_{ij}) - \frac{2\gamma r_{ij}}{\sqrt{\pi}}exp(-\gamma^2 r_{ij}^2)\right], \tag{19}$$

$$\mathbf{T}_{ij}^{(2)} = -\nabla_{\mathbf{r}_i}\otimes\nabla_{\mathbf{r}_j}\mathbf{T}_{ij}^{(0)}$$

$$= \frac{3\mathbf{r}_{ij}\otimes\mathbf{r}_{ij}-r_{ij}^2\mathbf{I}}{r_{ij}^5}\left[erf(\gamma r_{ij}) - \frac{2\gamma r_{ij}}{\sqrt{\pi}}exp(-\gamma^2 r_{ij}^2)\right] \tag{20}$$

$$- \frac{4\gamma^3\mathbf{r}_{ij}\otimes\mathbf{r}_{ij}}{\sqrt{\pi}r_{ij}^2}exp(-\gamma^2 r_{ij}^2).$$

In this way the electrostatic interaction between different Gaussian charge distributions, dependent on the topology, can be calculated. Regardless if the charges and dipoles are derived from different charge distributions or not Eqs. 18 to 20 can be used directly. Eqs. 18 to 20 are also directly applicable for alloys and molecules once the charge distributions are known.

The tensors $\mathbf{T}_{ij}^{(0)}$, $\mathbf{T}_{ij}^{(1)}$, and $\mathbf{T}_{ij}^{(2)}$ describe every interaction between two sites i and j in the DIM as defined in Eq. 2 and explicitly seen in the matrix definition in Eq. 3. The interaction between sites in the DIMs are therefore determined by the choice of charge distribution and here in particular the radii of the charge distributions. While the radii only have a minor influence on the position of the plasmon resonance for spherical particles, the resonance position for non-spherical particles like rods even a small change in the radii of the charge distribution can give very large shift in the resonance. Choosing a good representation for the charge distribution and fit for the radii in the DIM is crucial for the description of geometric distortions from spherical particles.

2.4 Relations to the Discrete Dipole Approximation

The discrete-dipole approximation (DDA) was developed by De-Voe as a flexible and powerful technique for computing scattering and absorption by targets of arbitrary geometry and as a method of discretization of Maxwell's equations for a particle in a field.[110,111] Purcell and Pennypacker later included retardation effects into the DDA which means that the aggregates no longer have to be small in comparison to the wavelength of the incoming field.[112] The DDA algorithm assumes that any arbitrary object is replaced by a set of finite cubic elements small enough so that only dipole-dipole interactions induced by the incident field in neighboring elements occur. This helps to reduce Maxwell's equations to an algebraic problem involving many coupled dipoles. The appropriate choice of the polarizability of each element leads to an accurate simulation of electric fields within the number of dipoles used to approximate the object. The main advantage of DDA is the flexibility it offers in describing arbitrarily shaped objects.[113]

The DDA is an approximation of a particle by a finite array of polarizable dipole moments. The dipole moments respond to the local electric field and interact with one another via their electric fields and numerically the DDA is represented by Eq. 5. For a particle of arbitrary geometry the DDA requires choices for the locations and the polarizability of the point dipoles in order to represent the particle. Each dipole in the DDA represent the local polarizability of a particular subvolume of a particle. The spacial resolution of the DDA depends on the volume of each subvolume for every dipole. Since there are no restrictions on the volume of the individual dipoles weaker closer spaced dipoles can be used to describe a complex surface topology and larger dipole volumes for the body of the particle. While the spacial resolution of the DDA in this way can be improved this method quickly becomes prohibitively expensive.[45] Secondly using the experimental values of the frequency dependent dielectric constant also limits the subvolume size to a volume where the bulk dielectric constant makes physical sense.

The DIM is a DDA method where each subvolume is an atomic volume and the dipoles are placed on the nuclei of each atom. The DIM is, in some sense, the minimum subvolume for a material since the spacial resolution of the DIM is atomic. We here notice that the DDA of course can be extended to include both charges and higher order moments seen in the DIM.[92] The strengths and weaknesses of the DDA and the DIM are therefore also similar. The cd-DIM is an example of where the DDA method is applied down to the atomistic level.[95]

3 Review the Ex-DIM model

Since all interactions between different sites in the DIM's are determined by the choices of charge distributions the differences in DIM's are primarily in self interaction part described in the diagonal. From the Lagrangian in Eq. 1 the self interaction of the charge and dipole are described by c_{ii} and α_{ii}. The self interaction is, however, essential in describing the position, width and magnitude of a resonance, size dependence, medium and temperature shift in position and magnitude of the resonance. The Ex-DIM is a dipole only model because the charges are not parameterized,

which means that the diagonal only consists of α_{ii}. In the parameterization of c_{ii} the same effects as in α_{ii} would also have to be considered and effects should emerge in a similar form.

The different effects such as temperature, size and media all requires modification of the polarizability α_{ii}. Each effect and term in α_{ii}

$$\alpha_{ii,kl}(\omega, \mathbf{P}, T, f_{cn}, n) = \left(\frac{a_i(f_{cn})}{r_{\text{bulk}}} \right)^3 \alpha_{ii,s,kl} n^2 L(\omega, \mathbf{P}, T, n) + \alpha_{ib}. \quad (21)$$

will be described in separate sections. In equation 21 $\alpha_{ii,kl} = \alpha_{ii}\delta_{kl}$ for $k, l = x, y, z$, $\alpha_{ii,s,kl}$ is the frequency independent polarizability and specific for each atom, α_{ib} the interband transition, $L(\omega, \mathbf{P}, T, n)$ a Lorentzian while $(a_i(f_{cn})/r_{\text{bulk}})^3$ and n^2 are environment modifications that will be explained in the subsequent sections.

3.1 Multiplicative environment factors

Surface topological effects related to the coordination number not only effects the radii of the charge distribution as seen in Sec. 2.3.2 but also the polarizability of the individual atoms. The scaling of the individual atomic polarizability as $(a_i(f_{cn})/r_{\text{bulk}})^3$ is inspired by studies of small gold clusters where the atomic polarizability is shown to be very dependent on the topology.[114,115] In $(a_i(f_{cn})/r_{\text{bulk}})^3$ the nominator $a_i(f_{cn})$ is calculated from Eq. 16.

The $(a_i(f_{cn})/r_{\text{bulk}})^3$ term ensures that surface atoms, depending on the coordination number, will have a larger intrinsic polarizability than bulk atoms and hence increase the total polarizability for clusters with more surface atoms. $(a_i(f_{cn})/r_{\text{bulk}})^3$ primarily shift the total polarizability and gives only a minor shift in resonance position which is dominated by the charge distribution as discussed in Sec. 2.3.2.

n^2 is the square of the refractive index n of the media for the particles and is similar to the expression from DDA.[45,116] The media is known to give significant polarizability shift along with some shift in the position of the plasmon resonance. The major shift in the value polarizability from the media, however, stems from the change in the relaxation constant as described in Sec. 3.2.2. n^2 as a multiplicative factor here mainly ensures the shift in the resonance frequency.

3.2 Lorentzian

The Lorentzian $L(\omega, \mathbf{P}, T, n)$ in Eq. 21 regulates the size-, geometric-, temperature- and media dependence. The geometric part of the size dependence comes in via the size dependent resonance frequencies of three size-dependent Lorentzian oscillators

$$L(\omega, \mathbf{P}, T, n) = N(L_x(\omega, P_x, T, n) + L_y(\omega, P_y, T, n) + L_z(\omega, P_z, T, n)), \quad (22)$$

where each Lorentzian:

$$L_i(\omega, P_i, T, n) = \frac{1}{\omega_i^2(P_i) - \omega^2 - i\Gamma_i(P_i, T, n)\omega}, \quad (23)$$

depends on the frequency ω, the plasmon length P_i along the direction i[117], the temperature T and the refractive index of the

media n. $L(\omega, \mathbf{P}, T, n)$ is normalized in the zero frequency limit ($\omega = 0$)

$$N = \left(\frac{1}{\omega_x^2(P_x)} + \frac{1}{\omega_y^2(P_y)} + \frac{1}{\omega_z^2(P_z)} \right)^{-1}. \quad (24)$$

The plasmon length is defined as the length over which the oscillations take place in a given direction and the aim of using the plasmon length is to give a differentiated directional size correction which reflects the geometry of the particle. In practice the plasmon length is a measure of the maximum distance between any two atoms plus the radius of those atoms in each of the x, y, z directions. We notice that the plasmon length is not invariant to rotations of the particle, since the P_x, P_y, P_z will change slightly with such rotations. The plasmon length is a pragmatic approach to describe size correction for all particle shapes. This means that regular shaped particles such as rods, films and other shapes where there are clear choice of directions should be rotated to align with the coordinate system while for irregular shapes the size correction is more unclear. It should, however, be noted that the effect of the size correction will rapidly decrease with size, and the charge distribution, described in Sec. 2.3.2, is significantly more important than the size correction for irregular shapes or shapes with uneven lengths.

3.2.1 Size-correction of the frequency

The size-dependent resonance frequency $\omega_i(P_i)$ is in the Ex-DIM written as

$$\omega_i(P_i) = \omega_a \left(1 + \frac{A}{P_i}\right), \quad (25)$$

where ω_a and A are atom specific fitted parameters and P_i the plasmon length in the i direction. The size correction for the frequency is the same as that for classical methods, as described in the introduction, and tends to zero in the bulk limit and remain finite in the smallest physical limit for the DIM, which is where P_i equals the atomic radii. This use of the plasmon length, as shown in Eq. 25 is consistent with the experimental work on both gold and silver spherical nano particles.[117–123] Adjusting ω_a and A in order to match the experimental size correction is straight forward.

3.2.2 Relaxation corrections from media

The size-, temperature- and media- dependent relaxation constant in the Ex-DIM is[124]

$$\Gamma_i(P_i, T, n) = [\Gamma(P_i) + \Gamma_{e-ph,d}(T)]/n^2 \quad (26)$$

the sum of a size- and temperature-dependent relaxation constant $\Gamma(P_i)$ and $\Gamma_{e-ph,d}(T)$), respectively. n^2 is the refractive index of the medium n and drives the large increase in the polarizability seen in media shift.

3.2.3 Size-dependent relaxation constant

The size-dependent relaxation constant $\Gamma(P_i)$:

$$\Gamma(P_i) = K_s/P_i \quad (27)$$

is proportional to the inverse plasmon length P_i which is the same functional form as the size-dependent relaxation constant from classical models and the size-dependence of the resonance frequency in Eq. 25. K_s is a chemical element specific constant obtained from fitting. The size-dependent resonance frequency and relaxation constant are very important for particles below 8 nm as seen in Fig. 17. Above 8 nm the size-corrections become more linear.

3.2.4 Temperature-dependent relaxation constant

The temperature-dependent relaxation constant describe the dampening and broadening of the plasmon resonance with respect to temperature due to scattering of electrons on phonons and lattice defects. In the Ex-DIM the phonon spectrum and the temperature dependence of the relaxation constant is described with a Debye model[125,126]:

$$\Gamma_{e-ph,d}(T) = K_0 T^5 \int_0^{T_D/T} \frac{z^4 dz}{e^z - 1}. \quad (28)$$

T_D is the Debye temperature and K_0 is a constant which includes the total scattering cross section of an isolated atom, the ion mass, the ion density, the Debye wave number, the Debye temperature, and other universal constants. K_0 is a fitted constant.

The specific resistance of gold exhibits a sharp jump in the relaxation constant when transitioning from the solid to the liquid phase[126]:

$$\Gamma_{e-ph,d}^{(l)}(T_m) = 2.4 \cdot \Gamma_{e-ph,d}^{(s)}(T_m), \quad (29)$$

where T_m is the melting temperature and l and s denote here the liquid and solid phase, respectively, see further the section below.

3.2.5 Melting temperature in Ex-DIM

The melting of particles are often performed using molecular dynamics simulations where the geometries from different snapshots at different geometries are used in the Ex-DIM. If the molecular dynamics simulation can reproduce the sharp shift in mobility seen upon melting and shown in Fig. 27 the Ex-DIM can adjust the relaxation constant of the individual atoms depending on the mobility. This gives an atomistic resolved two phase particle in the Ex-DIM.

If the melting temperature cannot be directly derived from the molecular dynamics simulations the melting temperature can be calculated from the plasmon length using the generalised Gibbs–Thomson equation[127,128]:

$$0 = L_m \left(\frac{T_m}{T_m^*} - 1 \right) + \Delta c \left[T_m \ln \left(\frac{T_m}{T_m^*} \right) + T_m^* - T_m \right] + \frac{2\sigma_{sl}\kappa}{\rho_s}, \quad (30)$$

where the effect of pressure is omitted in the Ex-DIM. In Eq. (30) L_m is the latent heat in the phase change for melting, T_m the temperature at which the phase change occurs (in the case of a curved surface of a body), T_m^* the bulk phase change temperature, Δc is the difference in the specific heat between the liquid and solid phase, $\Delta c = c_l - c_s$, where the subscripts indicate the phase, σ, the surface tension, ρ_s is the density of the metal, and κ is the mean curvature radius of the surface. The generalised Gibbs-Thomson equation from Eq. (30) accurately describes the melting temperature of spherical nanoparticles in the 1–12 nm range. Eq. 30 is in

the Ex-DIM primarily used to determine the phase of the particle which accordingly adjusts the relaxation constant in Eq. 29.

3.3 Interband transition

Since the plasmon resonance and the interband transitions in many materials partially overlap it is often not sufficient to model the polarizability of the plasmon resonance only due to the interference of the two close resonances. In the Ex-DIM the interband transition α_{ib} for gold is modelled by two size- and media-dependent Lorentzians extrapolated from the fit to the experimentally measures interband transitions[129]

$$L(\omega, R, n) = \sum_j^2 k_j n^2 \frac{1}{\omega_j^2(R) - \omega^2 - i\Gamma_j(R,n)\omega}. \quad (31)$$

In Eq. 31 k_j is the fitted multiplication factor for the j'th Lorentzian and R the radius. In the size-correction of the interband we assume that the particle is spherical and R is the input parameter for the fit. The media correction of $\Gamma_j(R,n)$ follow that of Eq. 26. Since the experimental data was limited at 300 nm for the interband transitions the Ex-DIM spectra is therefore limited at 300 nm for gold.

3.4 Parameterization of Ex-DIM

The parameterization of any method under continuous development often needs to be parameterized anew every time a new effect is introduced and the Ex-DIM is here certainly no exception. One of the fundamental problems with the DIM is the lack of available data both experimental and calculated along with which input parameters should be fitted and which can reliably be taken from table lookup of experimental data.

We will here discuss the different parameters in the Ex-DIM, finding data for the fitting of the parameters along with the actual fitting procedure.

3.4.1 Data for fitting

A major problem for the DIM, with respect to plasmonics, is getting reliable data for which all parameters can be uniquely determined. Since the atomistic DIM methods fulfill a gap between the QM and the classical continuum methods as shown in Fig. 1 getting fitting data from other numerical methods with an accuracy seen for the classical continuum methods for larger particles is difficult.

The only QM method, which can reach the particle size needed for plasmonics, in reasonable time is DFT. The accuracy of DFT is, however, not comparable with the classical methods and is therefore not suited for data extraction for small particles with a diameter between one and two nanometers.[75] Secondly extrapolating from particles with $50 \approx 150$ atoms also have the added difficulty from magic numbering due to the shell structure effect seen for small particles.

Classical methods have proven to be very accurate in predicting the position of the resonance frequency for large particles but size-correction from fitting to experimental data seems to be better than a purely theoretical approach.[130] The result from the classical methods also depends on the choice of experimental data
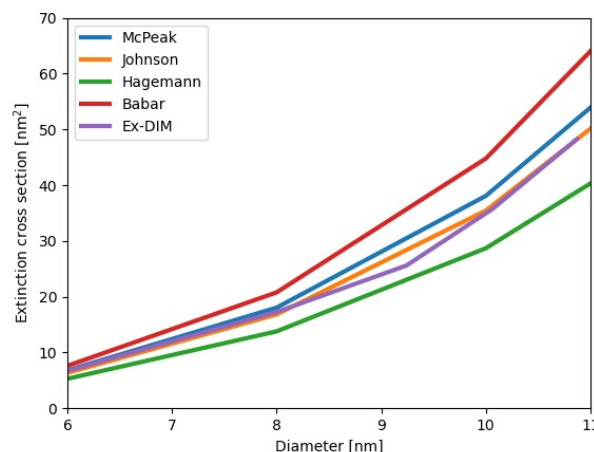

Fig. 2 The extinction cross section as a function of size for the Ex-DIM and Mie theory with different experimental inputs for the dielectric constant. The size correction in the Mie theory is taken from Karimi et al.[130]. The different experimental input data are from bulk or thick film from McPeak et al.[133], Johnson and Christy[134], Hagemann et al.[132] and Babar et al.[131].

used as can be seen for the extinction cross section in Fig.2. In Fig.2 all parameters such as the plasma frequency and relaxation constant are kept the same for the classical Mie method and only the experimental data of the dielectric constant is varied. This variation in the experimental data results in a significant shift in the absolute value of the extinction cross section where the experimental data from Babar et al.[131] is 1.6 times larger that the extinction cross section from the experimental data from Hagemann et al.[132] with the data from McPeak et al.[133] and Johnson and Christy[134] nested in between the Babar and Hagemann data. Secondly the position of the plasmon resonance also shifts $7\,cm^{-1}$ depending on the choice of experimental data.

Experimental data where a single effect is systematically examined for particles in the 1–15 nm size range are scarce. The effect of plasmon resonance as a function of particle size have been examined for some plasmonic materials like gold and silver but there is a lack of systematic studies for other effects.[120–123,135]

3.4.2 Parameters for fitting

In the Ex-DIM several parameters needs to be fitted or determined from theory for the method to work. We will here list these parameters, discuss their effect and discuss what data is needed to fit or determine the parameters.

r_{atom} and r_{bulk} from the radius of charge distribution and polarizability in Eqs. 16 and 21, respectively, are often set to the experimental radii which can be looked up. However, as discussed in Sec. 2.3.2 the charge distribution from the overlapping Gaussian model differ significantly from the atomic charge distribution and using r_{atom} and r_{bulk} directly from experiment without any scaling may not be wise. A scaling of r_{atom} and r_{bulk} will not change the polarizability in Eq. 21 and only change the off-diagonal elements describing the interaction between the charge distributions. Determining a scaling factor for r_{atom} and r_{bulk} requires data from ge-
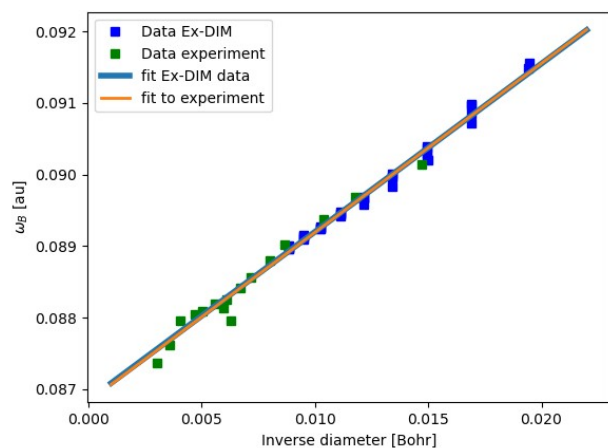
Fig. 3 Fitting the size correction in the Ex-DIM by comparison with experimental data. [120–122]

ometries different than spherical since the scaling factor for r_{atom} and r_{bulk} is responsible for the large shift in the longitudinal and transverse resonance frequency and extinction cross section observed in rods and thin films.

The frequency independent polarizability $\alpha_{ii,s,kl}$ in Eq. 21 only gives a minor shift in resonance frequency but is instrumental in setting the absolute value of the extinction cross section. Getting the absolute value of the extinction cross section right is crucial in getting the absolute value of the local electric field right and hence the effect on any surroundings.

ω_a and A from Eq. 25 regulates the position of the resonance frequency as a function of size and can easily be fitted for materials where there are systematic data of the size dependence.

K_s and K_0 are the size- and temperature-dependent relaxations constants from Eqs. 27 and 28 where knowledge of the absolute value of the extinction cross section as a function of size and temperature is needed.

For the interband transition k_j, the fitted multiplication factor for the j'th Lorentzian and R the radius needs to be determined. In the size-correction of the interband we assume that the particle is spherical and R is the input parameter for the fit. The media correction of $\Gamma_j(R,n)$ from Eq. 31 in Sec. 3.3

3.4.3 Fitting of the Ex-DIM

For the size-correction experimental data is used where a set of representative spherical particle are chosen. Since the number of atoms in spherical particle with a given plasmon length can vary several particles for each plasmon length are chosen. The fitting of the size correction of the Ex-DIM is performed by comparing the fit of the inverse diameter of the experimental data and Ex-DIM calculations as seen in Fig.3. Getting the size correction fit correct is surprisingly easy but only fixes ω_a and A from Eq. 25 and can be performed with many other parameters varying greatly.

The absolute value of the extinction cross section is fitted to the absolute values from Mie theory using the Johnson and Christy [134] experimental data and the Karimi et al. [130] size correction for the dielectric constant as shown in Fig. 20. Using

Johnson and Christy data for the fit gives an absolute value of the extinction cross section which lies in the middle of all the experimental values as seen in Fig. 2. The atomic polarizability and the size correction to the relaxation constant K_s can in this way be determined. K_0 the temperature-dependent relaxations constant is determined indirectly since a too large or small K_0 will increase the size sensitivity of K_s.

All fits in Figs. 3 and 20 can be performed with very different charge distributions since all particles used in those fits are spherical. In order to fit the charge distribution the resonance shift in FDTD and Ex-DIM have been compared for thin film since the longitudinal plasmon is here significantly red shifted and this red shift is primarily caused by the charge distribution.

4 Survey of Representative Ex-DIM model Studies

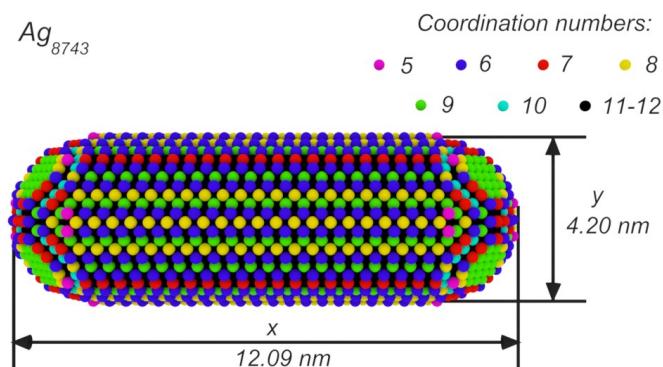### 4.1 Test of the model – silver nanoparticles

Fig. 4 Coordination numbers, longitudinal and transverse plasmon length and for an Ag nanorod containing 8743 atoms. Reproduced from Ref. [75] with permission from ACS, copyright 2019.

As a first set of applications beyond spheres, cubes and rods were also considered in Ref. [75]. Figs. 5 and 6 of that paper indicate substantial red shifts for nanorods along the long axis, in fact much stronger (with respect to aspect ratio defined as the ratio between the plasmon length in the longitudinal and transverse directions) than the red shifts for spherical particles with respect to the radius. This significant red shifting property is the basis is for the common utility of nanorods in imaging and sensing, as it easily can be manipulated by fabrication. Furthermore, the plasmon magnitude of the shifted peak is also greatly enhanced with increasing aspect ratio. In addition, the nanorods show plasmonic bands along the short transverse axis which typically are only slightly blue shifted in comparison to a spherical cluster with the same plasmon length. Notably, for the smallest of the two rods shown, Fig. 5, the transverse plasmon is split into two peaks, something that yet has to be experimentally confirmed for such small rods.

In Ref. [75] the interplay between the aspect ratio and diameter was further studied with respect to the plasmon resonance. A series of nanorods where each end is formed a half sphere connected by a cylinder, as shown in Fig. 4, were studied. In this rod figure one discerns a great variation of coordination numbers - the top layer of atoms with coordination number below $11 - 12$

and edge atoms with the lowest coordination numbers $5 - 6$ on the edges. As the surface atom polarizability is directly affected by the changes introduced by the coordination the plasmon generation is delicately dependent on the coordination numbers as also recognized by the parameterization in the Ex-DIM (as well as in the cd-DIM[82]) models.
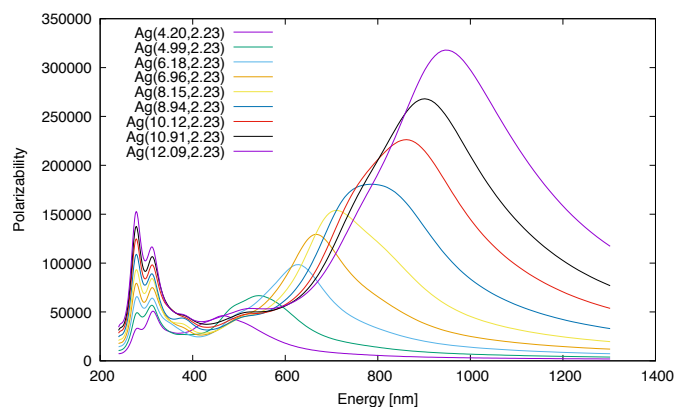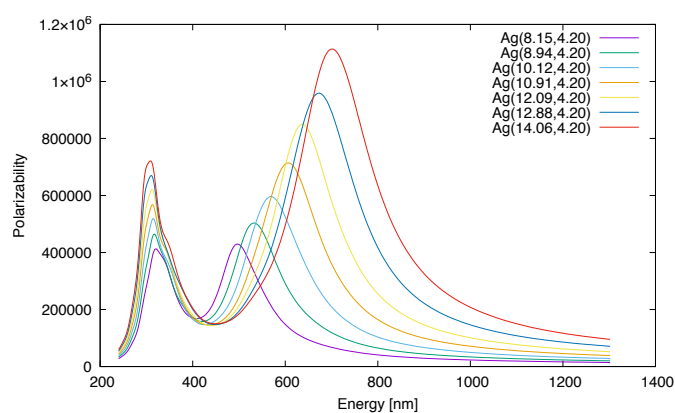

Fig. 5 Polarizability versus incident energy for $Ag(x, 2.23)$ nanorods with different longitudinal plasmon lengths. Reproduced from Ref.[75] with permission from ACS, copyright 2019.

Fig. 6 Polarizability versus incident energy for $Ag(x, 4.20)$ nanorods with different longitudinal plasmon lengths. Reproduced from Ref.[75] with permission from ACS, copyright 2019.

The red shift of the transverse plasmon is directly proportional to the aspect ratio and the difference in the longitudinal plasmon resonance changes with the diameter of the nanorod. The dependence on the diameter of the nanorods observed for gold nanorods of bigger dimensions [136–138]. Jakab et al. [139], show (experimentally) red shifts that are directly proportional to the aspect ratio and with a slight increase in slope compared to the Ex-DIM results — here the differences in the refractive index of the medium plays a role.

The relative polarizability and peak width between longitudinal and transverse plasmons increase significantly with increasing aspect ratio, actually the polarizability per atom increases linearly with the aspect ratio, while the dependence on the diameter of the nanorod is quite small, see Ref.[75]. Thus both the maximum and the absorbance of the longitudinal SPR can in this way be
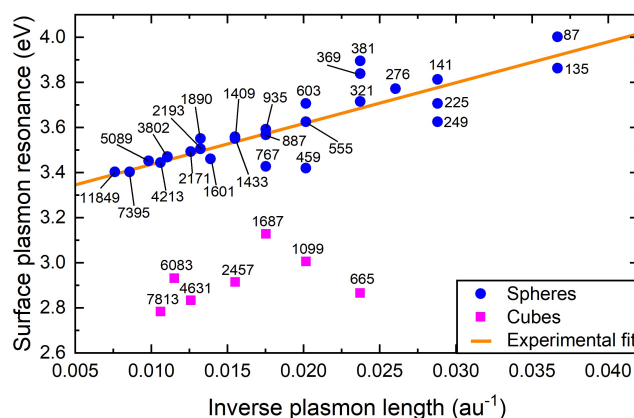

Fig. 7 SPR for sphere and cubes with different plasmon lengths. Reproduced from Ref.[75] with permission from ACS, copyright 2019.

controlled by the aspect ratio and the diameter. It is notable that refractive index of the surrounding medium plays an important role, see further below.

Summarizing - the Ex-DIM results for small nanorods agree with observation for larger particles in that for nanorods the longitudinal resonance significantly red shifts and that the transverse resonance slightly blue shifts with aspect ratio. The red shift as well as the atom polarizability correlates linearly with the aspect ratio thereby making both the peak position and magnitude controllable for these particles. For the transverse direction the slope in blue shift shows a slight dependence on their plasmon length, something also seen for gold nanorods of larger dimensions[136,137]. Here, the refractive index of the surroundings seems only to give a constant shift for the plasmon resonance [139].

Also cubes were addressed in Ref.[75] as a test bed for further exploration of the Ex-DIM model. At the time for the publication of the model Ringe et al. [117] and González et al. [140] had shown that gold cubes red shift differently than spherical clusters with the same plasmon length — with larger red shifts up to $0.2\ eV$. Silver particles shift even more than gold with respect to size, see also [141,142]. The Ex-DIM results presented in Fig. 7 predict that there is also a larger size dependence for silver particles as their cubes are red shifted around 0.6 eV in comparison to the spheres; see also results for larger particles predicted by González et al. [140]. The size-dependence of the cubes and spheres thus follow similar trends although the geometric dependence for Ag are larger than for Au.

4.2 Hollow nanoparticles

In Ref.[143] hollow nano-shells were explored by the Ex-DIM model in order to test to what extent the role of cavity versus volume size of spherical particles can be used as an additional design parameter for plasmonics generation, along with the particle size dependence. Hollow spherical nano-shells, as depicted in Figure 8 made of gold were used for that purpose. As shown in Refs.[144,145] the surface charges on the nano-shells constitute a hybridization of plasmon modes from the cavity and the shell can, in a semiclassical approach, be described as two coupled harmonic oscillators,
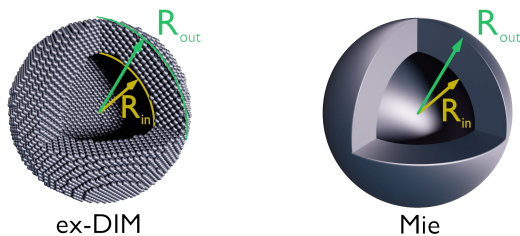
Fig. 8 Representations of R_{out} and R_{in} for Ex-DIM and Mie models of nano-shells. The Ex-DIM radius of the atoms corresponds to the effective radius. From Ref. [143]
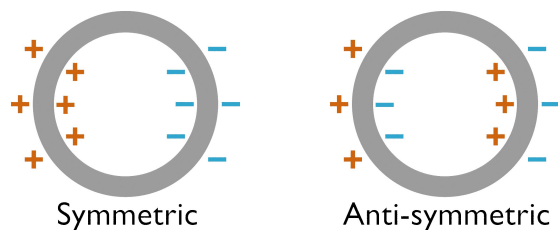

Fig. 9 Symmetrically (ω_-) and an anti-symmetrically (ω_+) coupled nano-shell plasmon modes. om Ref. [143]

Fig. 10 The spectral positions of SPRs for the symmetric and anti-symmetric modes versus R_{in}/R_{out} calculated via (a) Ex-DIM and (b) Mie theory for nano-shells with different R_{in}. The dashed line shows the spectral position of symmetric, ω_-, and anti-symmetric, ω_+, modes from Eq. (1) in Ref. [143] with (a) $\omega_B = 5.78$ eV and (b) 6.82 eV used for the fit. From Ref. [143]

as depicted in Fig. 9 It has been shown [146,147] that for larger nano-shells this approach gives both a good intuitive picture and good numerical results for the surface plasmon resonance frequencies for both small and large nano-shells. In Ref. [143] it was studied if the basic picture also holds going to ultra-fine dimensions.

In the semi-classical approach with two coupled oscillators the two SPRs are associated with red and blue shifts which depend only on the relative radius between the hole and the particle. Ex-DIM calculations largely confirm this contention, see Fig. 10a. Here, the antisymmetric mode weakly blue shifts with respect to the hole and particle radii, whereas the symmetric mode red shifts more strongly. Here it seems (Fig. 10b) that using Mie theory the forming of the resonances does not entirely follow the predicted plasmon modes from the semi-classical approximation, as well showing a too strong (R_{in}/R_{out}) dependence. Figure 11 shows the normalized imaginary polarizability calculated for nano-shells with fixed outer radius by the Ex-DIM model and by Mie theory indicate that the two theories possess similar red and blue shift trends for increasing hole size, although the numerical results are somewhat different. For a fixed inner shell radius the blue and red shifts for different (R_{in}/R_{out}) are not as distinct as for fixed outer radii. A difference between spectra for a fixed R_{out} and R_{in} is that for the fixed outer radius, the plasma frequency is the same for all clusters, while for the fixed inner radius, the plasma frequency changes with R_{in}/R_{out} where the highest ratio has the largest plasma frequency. The antisymmetric mode also becomes increasingly strong for larger ratios R_{in}/R_{out}, although still significantly weaker than the symmetric mode.

In summary, the Ex-DIM study presented in Ref. [143] could show that the prediction for larger nano-shells by the simple semi-classical harmonic oscillator model for symmetric and anti-symmetric plasmon modes holds well also for small nano-shells in the 2–13 nm range, having similar size dependence as seen for
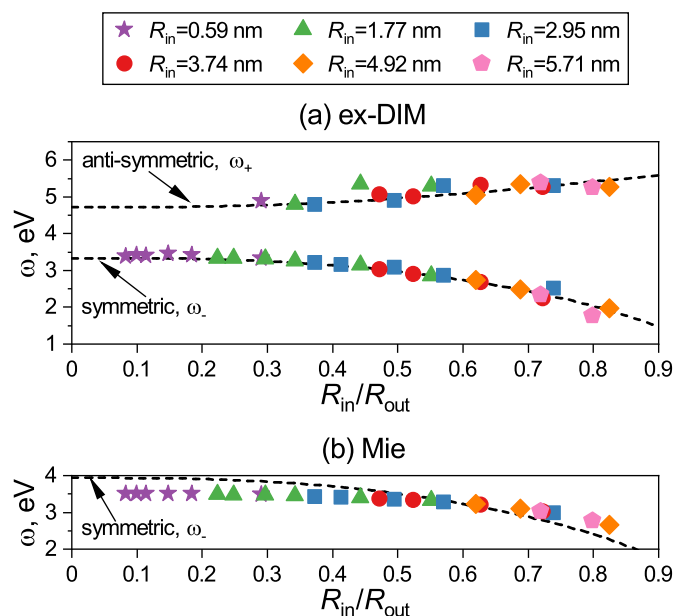
filled nanoparticles. For the extended discrete interaction model (Ex-DIM) the plasmon modes follow the same functional form predicted by the semi-classical model though with a different size-dependent plasma frequency. For the symmetric mode a significant red shift show up with increasing ratio between particle and hole ending in the regular surface plasmon resonance of a filled cluster, while the anti-symmetric mode disappears towards a filled cluster as expected.

4.3 Alloys and core shells

In addition to designing plasmonic nanoparticles by their size, shape and material, one can also consider compositions including more than one plasmonic material. Such alloy nanoparticles can be interesting for bioimaging, sensors and devices as the resonance position of the plasmon then can be adjusted over a large wavelength range just by varying the composition of the constituent metals. This gives flexibility that can serve the purpose for a particular application. Development in synthesis and characterization [148,149] have made studies of such alloyed or bimetallic nanoparticles possible through fine tuned design. Bimetallic particles formed by noble metal elements, like platinum, gold, silver and copper, stand out as the most promising candidates for such studies.

The question is, e.g. for a binary system, if the property looked for, extinction coefficient an plasmonic resonance, relates in a linear fashion or not with respect to percentage of the ingredients. Here the validity of the so-called Vegard law [150,151] has been examined for larger particles to quite some extent, which indeed overall have supported such a linear relation between resonance
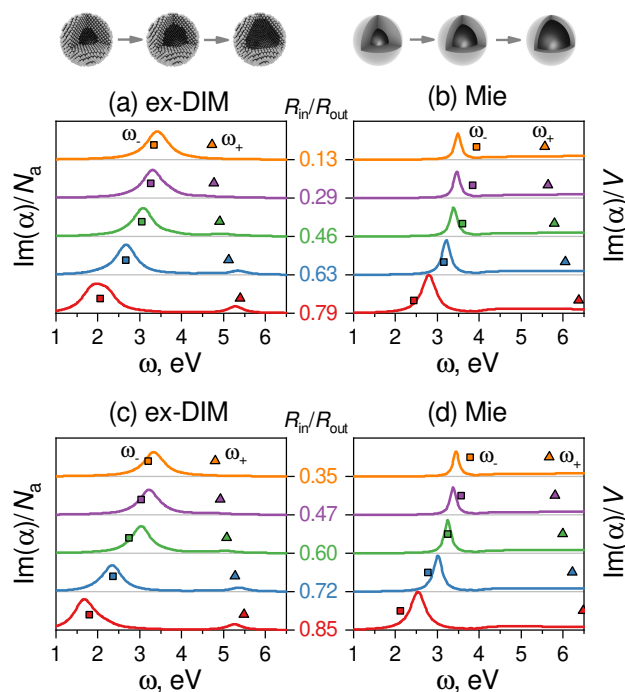
Fig. 11 Normalized imaginary polarizability from Ex-DIM model (left) and Mie theory (right) calculations for nano-shells with fixed outer radius R_{out}: 5.97 nm (top) and 7.94 nm (bottom). Squares and triangles give the positions of the symmetric (ω_-) and anti-symmetric (ω_+) modes from Eq.(1) in Ref.[143] with $\omega_B = 5.78$ eV (Ex-DIM) and $\omega_B = 6.82$ eV (Mie). From Ref.[143]

frequency and composition. Moreover, core shelling the two materials opens new flexibilities for design - which material is chosen to be core, respectively, shell and which thicknesses of the core and shell are preferable. Moreover, forming core-shell structures turns out to be an effective way to get a significant blue-shift in the surface plasmon resonance frequency.

In order to shed light on these questions for nanoparticles in the ultra-fine range a series of Ex-DIM calculations were carried out on gold-silver nanoparticle alloys in the small (1–15 nm) nanoscale regime in Ref.[149]. It could there be demonstrated that the surface plasmon resonances of these alloys and core-shell particles, and irrespective of geometry, indeed follow Vegard's law of the nanoparticle quite well, see Figs. 12a and 12b. However, it was also shown that the dependence of the polarizability with size is highly non-linear with respect to the constituent ratio and with geometry in both alloys and core-shell nanoparticles. Thus going from the case of 100% gold to 100% silver in spherical nanoparticles the polarizability curve shows a minimum at about 40% before rising to the high silver value, see Figs. 13a and 14a. In the mixed situation, with difference in polarizability of the mixing constituents, there is a quenching and increased misalignment of the dipoles due to the heterogeneity where the nearest neighbors respond differently to the external field dipoles causing misalignment and loosing the cooperative effect of having aligned dipoles. Interestingly, other shapes than spherical with a low aspect ratio showed a better linearity, see Figs. 13b and 14b for nanorods. It was furthermore demonstrated that there is only a small de-

pendence of the surface plasmon resonance on the exact atomic distribution in a nanoparticle and that the numeric standard deviation of this dependence decreases rapidly with the size of the nanoparticles.

Figs. 14c and 14d show the polarizability for the core-shell structure. A seen the response is of quite unsystematic nature making it hard to a priori design such systems and to predict their polarizability. No enhancement above the Vegard law could be observed. The Ex-DIM results for the ultra-fine alloy particles indicate that the classical methods of treating an alloy without any atomic resolution largely are valid. With appropriate correction for the dielectric constant classical methods could be recommended simulating nanoparticle alloys down to the 4–5 nm size. However, there is indeed a standing issue of the validity of current size corrections of the bulk dielectric constant for the very small particles and here direct Ex-DIM simulations of the dielectric constants could be recommended as a more precise alternative. It is clear that more irregular the shapes and more complex the elementary compositions, also will call for atomically decomposed models like Ex-DIM.

4.4 Plasmonics nanoparticles and local fields

Ref.[152] covered a broad range of geometrical structures with different symmetry and geometry in order to analyze the distributions of plasmonically generated near electric fields and the concentration of hot and cold spots around the particles, see Fig. 16. We could predict wide ramifications of these results for applications of ultra-fine plasmonic particles in the areas of imaging, sensing and energy harvesting. After the initial development and parameterization of the Ex-DIM method, and the test applications on spheres, rods, hollow particles and alloys reviewed above, a more comprehensive set of applications of the model was undertaken. Here a variety of ultra-fine gold particles were studied, focusing on different geometric shapes and symmetries and on the local distributions of the plasmonically generated electric nearfields for all these particles. Although experimental comparison often indicates that classical electromagnetic theory works well when the complex dielectric environment is well characterized and modeled, there is, as already mentioned in the introduction of this review, an open question when the particle size are diminished to the level where there are issues with using the bulk dielectric constant. This in particular when one deals with particles of complex shapes, which was the motivation for this study. One can here also question the applicability of conventional discrete dipole interaction models in this region and their capability to describe the plasmon polarizability dependence of the surface topology and their predictability of detailed field generation. With the Ex-DIM model applied in Ref.[152] it was observed that also for very small nanoparticles there are significant field localizations and charge concentrations occurring at surfaces and close to sharp edges, however, with the difference that such localizations are spatially very confined, also for particles with high symmetry, and that there are sharp geometric variations of the field amplitudes. Hot spots appear as very narrow and can rapidly, within 1 nm or less, decrease to cold spots as an effect of interference between

(a) Spherical Au/Ag alloys with 1553 atoms and 6051 atoms

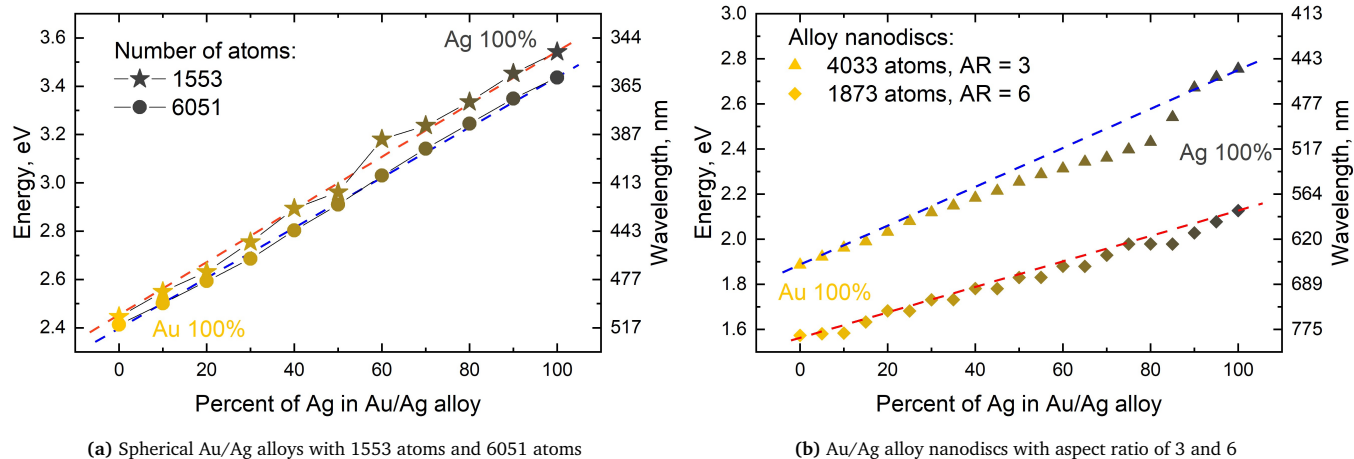**(b)** Au/Ag alloy nanodiscs with aspect ratio of 3 and 6

Fig. 12 Position of SPR versus percentage of Ag atoms for Au/Ag alloys of different geometries. Dashed lines indicate Vegard's law. Note that the frequency in wavelength scale is non-linear. From Ref. [149]
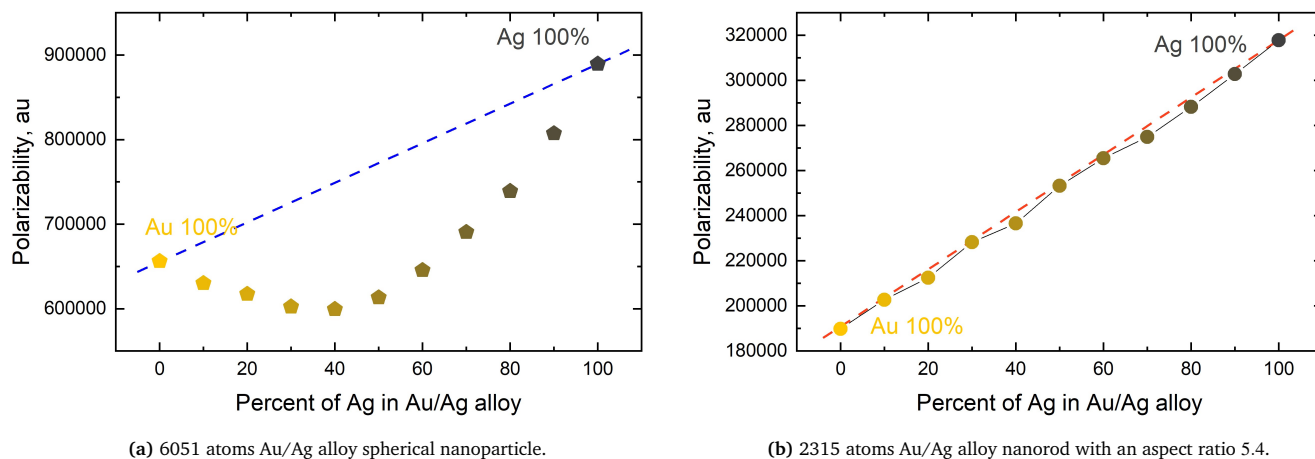

(a) 6051 atoms Au/Ag alloy spherical nanoparticle.

(b) 2315 atoms Au/Ag alloy nanorod with an aspect ratio 5.4.

Fig. 13 The polarizability at SPR maximum versus the percentage of Ag atoms for Au/Ag alloys of different geometries. Dashed lines indicate Vegard's law. From Ref. [149].

the external and generated fields. Thus when particles of this size are employed as strong field concentrators the geometric requirements are very sharp. It is here also notable that Ex-DIM makes it possible to study the role internal crystal structure on the optical response of nanoscale particles which makes it further possible to explore the external field polarization dependence of the generated local fields, something that is not achieved with the common classical models. As shown in Ref. [152] there is in general a strong deviation from the Lorentzian surface plasmon extinction spectra, typical for ideal spherical particles, for particles with sharp edges and complex shapes. These shape features can significantly change the plasmonic spectra with respect to spherical particles of comparative size. We can summarize the findings for the different shapes as:

Spherical particles - Fig. 15(a) and Fig. 15(b,c) indicate that extinction cross sections and the field distributions are largely interrelated for such particles. Because of the absence of sharp edges,

the gradients of the local field strength are smoothly varying and so is also the Lorentzian form factor of the surface plasmon extinction band. Hot and cold spots emerge at poles in the direction of polarization of the incident radiation, respectively, around the equatorial part of a sphere. The origin of the latter can be interpreted as destructive interference between the external and plasmonic fields.

Hemispherical particles — The conclusions drawn from Ex-DIM results displayed Fig. 16(a) accord qualitatively with available experimental data for larger plasmonic silver hemispheres[153], for example, that the extinction in transverse polarization is noticeably different from spherical particles (Fig. 15) and that the plasmon resonances are shifted to longer wavelengths, while for longitudinal polarization, the extinction decreases and is blue shifted, coinciding with that for the full sphere. Furthermore, the local field distribution differs from the classical picture of the dipole field of a sphere.
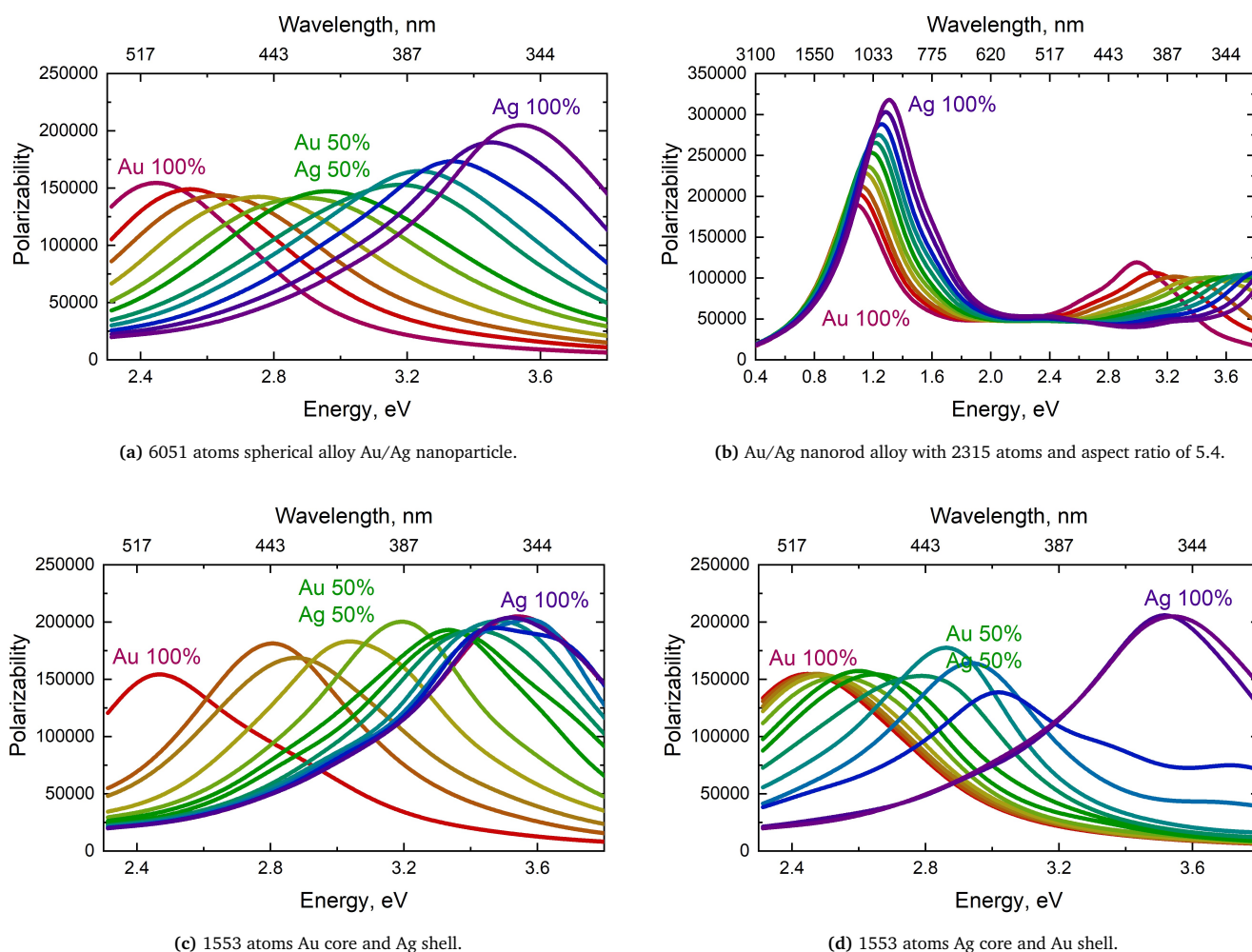
(a) 6051 atoms spherical alloy Au/Ag nanoparticle.

(b) Au/Ag nanorod alloy with 2315 atoms and aspect ratio of 5.4.

(c) 1553 atoms Au core and Ag shell.

(d) 1553 atoms Ag core and Au shell.

Fig. 14 Polarizability of Au/Ag alloys spherical nanoclusters with different geometries in **(a)** and **(d)** and for Au-Ag and Ag-Au core-shell in **(c)** and **(d)**. The frequency in the wavelength scale is non-linear. From Ref. [149].

Toroidal nanoparticles – are characterized by a smooth and wide extinction curve, shifted to longer wavelengths compared to spheres with similar widths and demonstrate a broad resonance in the visible range. [154] Ex-DIM calculations clearly predict additional resonances where one resonance is in the near-IR range Fig. 16(b). This agrees qualitatively with observations for large size tori (ca 60 nm) with varying thickness of the ring walls as presented in Ref. [155] showing substantial red shift of the extinction maximum with lowering of as the ring thickness grows. The spectra for the rings can be analyzed in terms of strong electromagnetic coupling between the inner and outer ring walls leading to mode splitting into symmetric and antisymmetric mode branches, similar to the case of hollow metal particles briefly reviewed in Sec. 4.2. Field distributions inside the nanoparticles show cold spots at the poles along the external field polarization and hot spots in the orthogonal direction. Moreover, the inner cavity is characterized by a constant depolarization field amplitude.

Conical particles — are characterized by splitting into a long-wavelength band covering the long-wavelength part of the visible range and a near-IR range feature for longitudinal polarization,

see (Fig. 16(c)) while there is a single maximum with a large amplitude for transverse polarization. The inhomogeneous local field distribution is, as expected, concentrated near the sharp edges and is especially pronounced near the cone tips. Here the hot spots can be found, while cold spots appear near the flat surfaces. The strong fields appear to be spatially limited and outside these hot spots the field amplitudes decrease rapidly and even create cold spots due to destructive interference between the generated and the external fields. The distance between hot and cold spots is only at the order of 1 nm, producing challenging geometric requirements when these particles are used for detection and sensing surrounding media. The longitudinal polarization extinction spectrum of the truncated cone in Fig. 16(d) is transformed into a mono-resonant peak with a large amplitude. The presence of two peaks for transverse polarization refers to the radii of the upper cut and the base of the cone, where the field is also highly concentrated.

Truncated double cones - Although these particles show plasmonic spectra that resemble those of the truncated cone shape particles, see Fig. 16(e), their optical properties differ signifi-
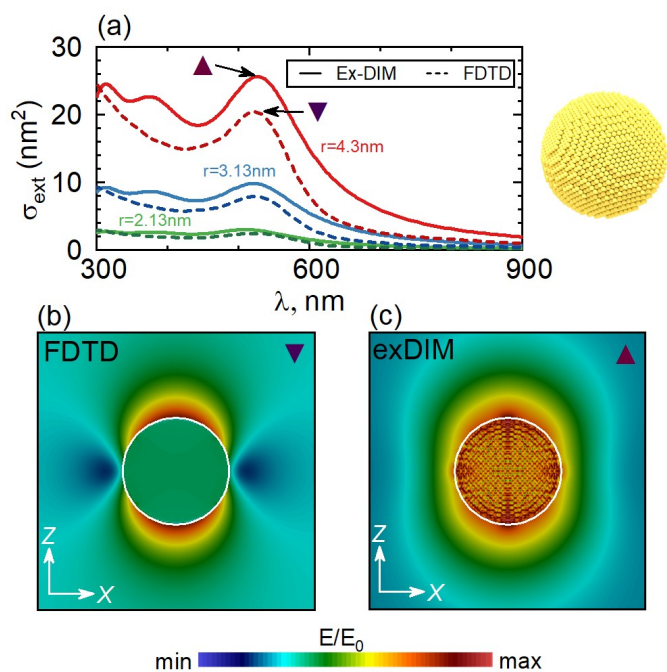
Fig. 15 Extinction cross section spectra for spherical Au nanoparticles of different sizes in aqueous medium calculated by the Ex-DIM (solid lines) and by the FDTD method (dashed lines) – (a); Configuration of local electric field calculated for spherical particle with r=4.3 nm using FDTD method – (b) and Ex-DIM – (c) for Au spherical particle at the wavelength $\lambda = 525$ nm. Reproduced from Ref. [152] with permission from ACS, copyright 2021.

cantly. For longitudinal polarization, there is a mono-resonant long-wavelength extinction band with a large amplitude, while in the transverse polarization, the maximum resides at considerably shorter wavelengths and with smaller amplitudes following an increase in the aspect ratio. The position of the maximum in the extinction spectrum of the double cone strongly depends on both the aspect ratio and the radius of curvature of the tips. The extinction spectrum maximum shifts to the short wavelength range along with bigger cuts of the tip. Compared to bipyramids,[41,42,156] the radius of a cut rounded tip results in a blue-shifted longitudinal plasmonic maximum peak, shifting linearly if the length of the biprymid is constant. Conversely, having a constant radius of tip curvature red-shifting occurs for longer particle lengths. These results are in line with the Ex-DIM findings in Ref.[152] referring to the sensitivity of the plasmonic spectra towards how the tip of the cone is cut. It is clear that the smaller the curvature radius and the volume of the tip, the higher is the longitudinal polarization field strength.

Tubular Particles form another set of particles explored in Ref.[152]. They receive interest from the fact that they can be exploited in theranostic applications that integrate targeting, imaging, and photothermal therapy [157] and for applications also in biosensing, protein transportation [158] and SERS imaging [159]. This owes much to open-ended nature of the nanotubes with large inner voids that can act as containers, but also because, compared to their spherical counterparts, these nanostructures have extinction bands in the spectral range of transparency of hemoglobin

making it possible to use them for laser photothermal therapy. A particular Au nanotube with an outer radius of 3.4 nm, an inner radius of 1.56 nm, and a height of 6.8 nm was studied by Ex-DIM in Ref.[152] Fig. 16(f) shows that the extinction band maxima in the spectra of this nanotube for longitudinal as well as for transfer polarization reside above 660 nm, corresponding to the short wavelength onset of the hemoglobin transparency range [22]. The local field in the nanotubes is concentrated around the outer and inner sharp edges just like for truncated cones.

Tetrapodic nanoparticles – can in principle generate a multimode response because of the presence of several resonator configurations similar to a connection of four rods. However, Ex-DIM calculations indicate that all three orthogonal polarization orientations have approximately the same response in the Au structures, see Fig. 16(g). A strong field localization occurs near the limbs oriented along the polarization of the external field while in the orthogonal direction a cold spot can be observed.

Cross-shaped particles – demonstrate a broadened resonant band in the visible red or near IR part with transverse polarization, while with longitudinal polarization a much narrower maximum located with comparable amplitude. The field shows pronounced cold spots at a distance of several nanometers observed in one polarization direction, see Fig. 16(h).

4.5 Red shifts

As mentioned in the introduction of this review, and which also has served as a motivation to derive the Ex-DIM model is that the ultra-fine regime 1–10 nm provides both challenges and opportunities for plasmonic research: Challenges, because this size regime is in between the applicability of quantum mechanical methods and classical electromagnetic theory: Opportunities as it can account for the most important aspects of both theories. Being semi-empirical yet based on atomic resolution, Ex-DIM, like other discrete interaction models, provide the possibility to address this size regime. Opportunities, because of the great number of applications such particles bring about, in particular for biosensing in the biomedical area where ultra-fine plasmonic particles provide a number of distinct advantages like reduced interference with the research object, size compatibility of small clefts, pockets and other compartments of the target biostructures. There are primarily two such factors that make plasmonic ultra-fine nanoparticles different from larger ones, namely enhanced surface effects due to the increased ratio of surface to bulk atoms, and the limited validity of using bulk dielectric constants. It is therefore imperative for a discrete interaction model to find quantitative relationships between structure and the plasmonic properties which remediate these two challenging factors.

The red shift of the plasmonic response is one of these factors that needs to be scrutinized when going ultra-fine. This red shift with respect to nanoparticle size is an important factor in the design of the particle to operate in certain wavelength regions for sensing or imaging. A linear relationship between shift and size has for long been assumed and applied as the prime design criterion. It was, however, recently contested in some recent reports not to hold for ultrafine particles. Piella et al[121] could show that
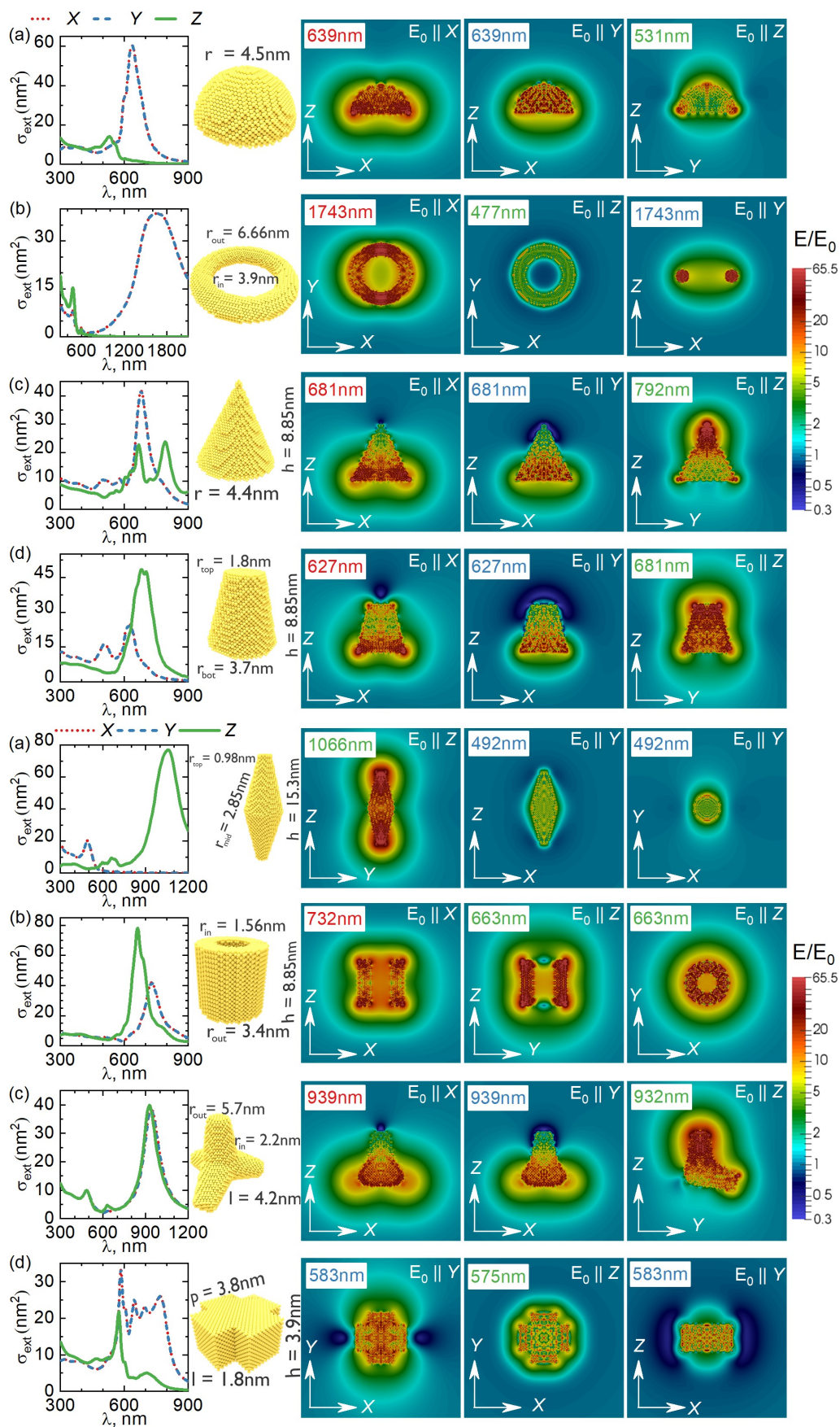
Fig. 16 Plasmonic electric fields from polarized external electric fields together spectra for ultra-fine plasmonic nanoparticles of different shape. Reproduced from Ref. [152] with permission from ACS, copyright 2021.
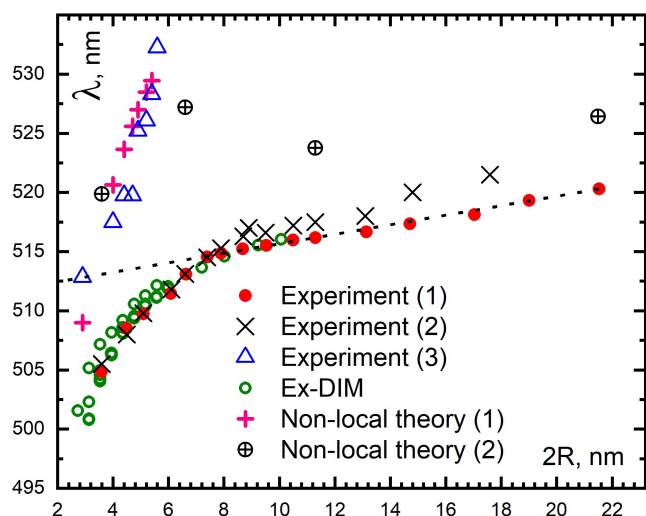
Fig. 17 Comparison of the size dependence for the maximum absorption spectra of Au nanoparticles in aqueous medium with dielectric constant $\varepsilon=1.78$ obtained by Ex-DIM in the size range 3–10 nm (hollow green circles) and experimental data (1) — red circles from [121], and (2) — crosses from [135]. The experimental inflection point is established for a particle diameter of 8 nm. Dashed line shows a general trend in the red-shift size dependence for Au nanoparticles in the size range 8–22 nm. Data on the non-local theory (1) — pink crosses were taken from Ref. [160] for comparison with experimental data (3) — blue triangles from Ref. [118], and the non-local theory (2) — black circled plus from Ref. [130] for comparison with experimental data (1) from Ref. [121] (red circles). Reproduced from Ref. [161] with permission from ACS, copyright 2022.

there is an inflexion point at about 8 nm in the red shift dependence for gold nanoparticles, above which the red shift retains its common linear behavior, while below it becomes non-linear with a stronger dependence on size; Haiss et al[135] observed a significant variation in size dependency of the red shift at about 10 nm; Peng et al observed a corresponding shift at about 12 nm for colloidal silver nanoparticles[162]. Their classical modelling approach agreed excellently with the linear dependency above this limit, but broke down below. The inflection point for the red shift indicates a change of physics. For the larger particles the so-called retardation effect has served as the underlying explanation, while for the ultra-fine regime one can suspect surface induced effects playing the dominating role. As the classical physics may break down the use atomistic based descriptions are called for, something that was the case in the recent Ex-DIM work presented in Ref.[161]. Here the role of surface layers on the dependence of the red shift of plasmon resonance on the particle size was analyzed, from which a quantitative relation was derived and compared with available experimental data. Two key notions were introduced to unravel the surface effects — the anisotropy factor and the chaotization factor.

The anisotropy factor is defined by the positions of surrounding atoms around each arbitrary atom of the crystal lattice and the radial dependence of this factor[163]. The local anisotropy of atoms near the surface increases due to breaking and deforming the crystal lattice near the surface. It has been shown that the local anisotropy factor strongly correlates with the local electromagnetic response. The chaotization factor refers to the degree

of disorder of the atomic light-induced dipoles when interacting with each other, combined with the dispersion of their amplitudes. Both the anisotropy and the chaotization factors are mathematically defined in Ref.[161] and Figure17 summarizes the main result of the paper.

The inflexion point at about 8 nm for the red shift dependence versus size is clearly seen in accordance with two recent experiments, while some work, both experimental and theoretical, are at odds with this finding. The common view of the source of the linearity for the larger particles is due to an increase in the total effective (inertial) mass of electrons in a particle upon increasing particle size[164]. A depolarizing field inside the particle is created due to collective oscillations of conduction electrons and local charge redistribution in the plasmonic nanoparticle. An electrical capacitive restoring force appears resonating with the inductive conduction of electron mass.[164] The red shift then appears by an increase in the electromagnetic inertial mass of the conduction electrons in the nanoparticles. The increase in the inertial mass is in turn caused by inductive loading of magnetic fields inside and outside the nanoparticle. The inertial mass of electrons in the small sized particles is much reduced and would point at a reduced red shift dependence, quite opposite to what is observed in Fig. 17. Thus other concurrent processes, come into play, namely those taking place at the surface. We then enter into a range where traditional Mie theory or other classical approximations are too limited to be applied. Here we turn to the Ex-DIM results displayed in Fig. 18 referring to the radial dependencies of the local anisotropy factor; the degree of chaotization of atomic dipoles; the real part of atomic dipole moment distribution in a particle; and field distribution images for four different ultra-fine particles of size ranging from 3 to 6 nm.

Fig. 19 gives a comparison between the ideal case of complete orientational ordering of identical dipoles with equal amplitude and the effect of non-collinearity for an Au nanoparticle with a diameter of 3.13 nm. The chaotization effect in a surface layer of the field distribution inside and outside a particle for same size parameters and ambient medium can in this way be visualized in Fig. 19.

The nonlinear and stronger red shift dependence for small smaller particles can be explained by the local anisotropy of the crystal lattice, and caused by the chaotization of light-induced atomic dipoles near the particle boundary, and furthermore by the field inhomogeneities arising near the surface. We here see that for all particles both anisotropy and chaotization factors are localized to the surface, but also that they spread inwards towards bulk, more so for the smaller particles. This is also reflected by the dipole moment distribution, which spreads the most for the smallest particles and also with weaker generated plasmonic fields and weaker hot spots. It is seen that the distribution of the field strength modulus and field direction inside the nanoparticles are strongly inhomogeneous with a weakening of the local field strength towards the surface layer, as well as a concentration of field minima near the the poles. These field minima are actually located below the surface in a thin layer. Cold spots of the field appear at the particle poles and intensify when the particle is embedded in a dielectric medium (not shown).
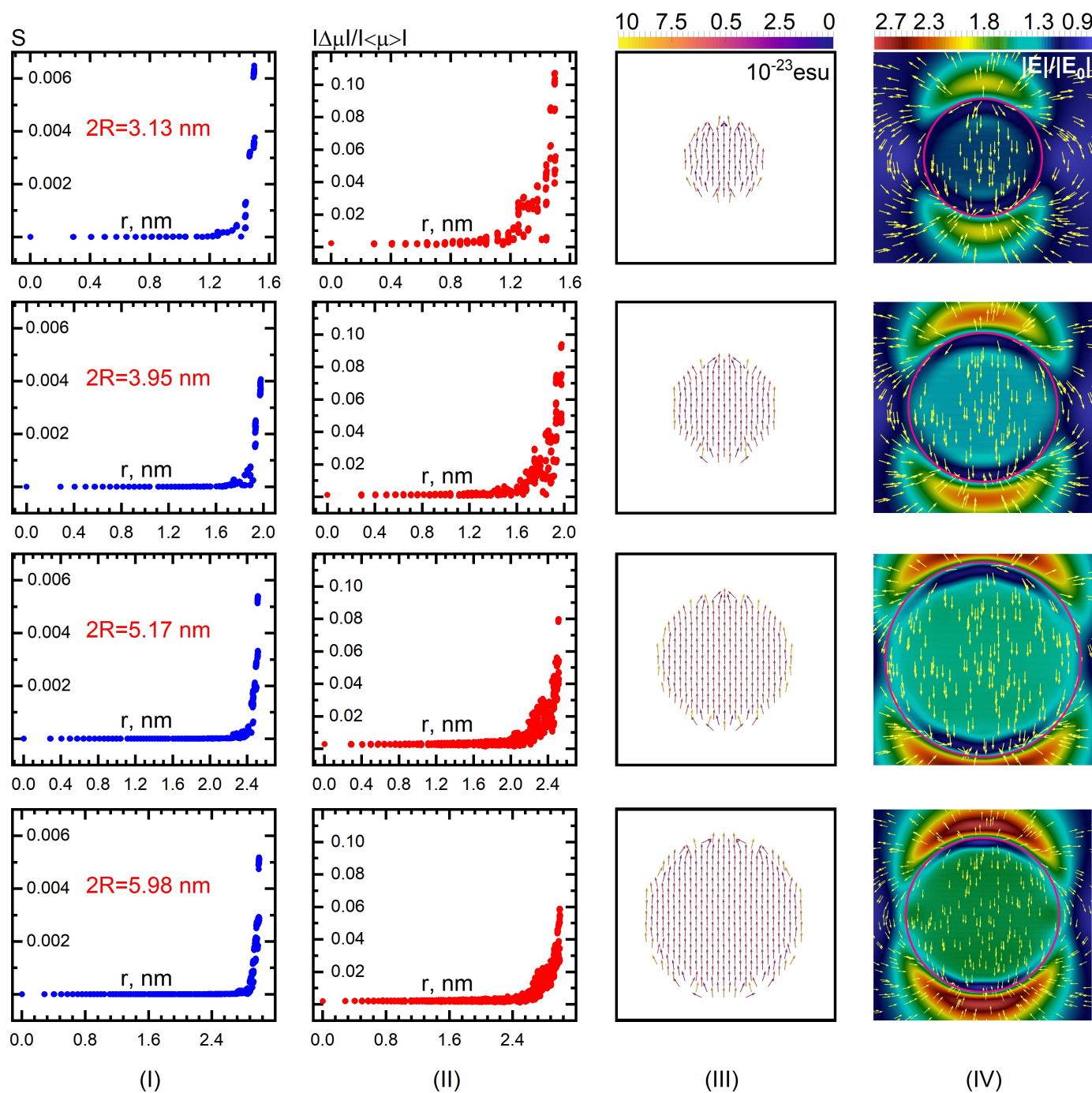
Fig. 18 Radial dependencies of local anisotropy factor (I), chaotization of atomic dipoles (II); distribution of the atomic dipole moment (real part) in a particle (III), distribution of the maximum field strength modulus ($|E|/|E_0|$) and field directions inside and around the Au nanoparticles with diameter 3.13, 3.95, 5.17, 5.98 nm in aqueous medium with refractive index $n=1.33$ at the wavelength of SPR maximum for vertical polarization (IV). The largest particle with a diameter of 5.98 nm with the field distribution image is reduced in order to cover the field distribution pattern (the pink circles around the particles indicate the positions of their boundaries). Reproduced from Ref. [161] with permission from ACS, copyright 2022.
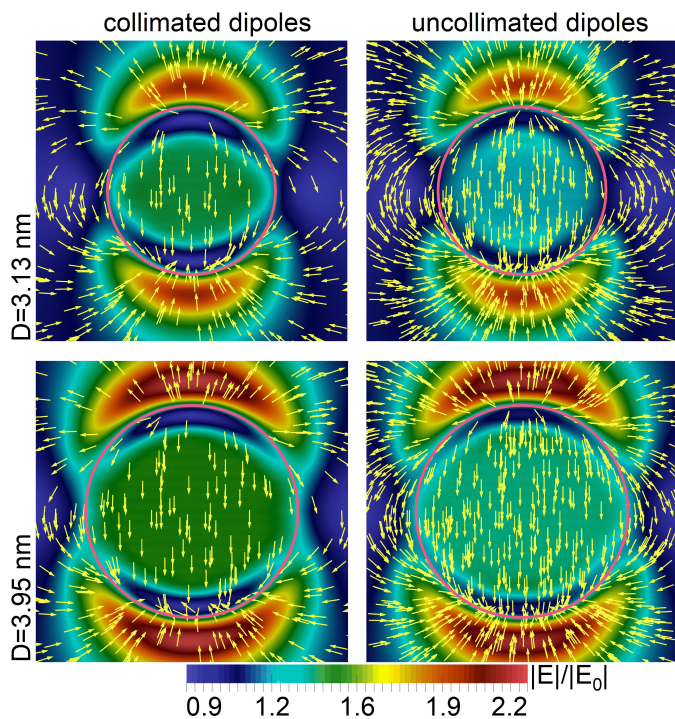
Fig. 19 The maximum field strength modulus and the field direction inside and around the Au nanoparticles with diameter 3.13 and 3.95 nm in the aqueous medium with refractive index $n=1.33$ at the wavelength of SPR. On the left: all dipoles in a particle are collimated, on the right: non-collimated dipoles. Polarization is vertical. Reproduced from Ref. [161] with permission from ACS, copyright 2022.

All the above reviewed features can be referred to the fact that the relative, but not the absolute, size of the surface layer of the particles strongly depends on the particle size for a given local environment. In actuality it is the ratio of the volume of the surface layer to its entire volume that is the physically important factor, rather than the particle's surface-to-volume ratio, as is commonly considered. Thus, the red shift mechanisms in the extinction spectra for ultra-fine nanoparticles are associated with a significant increase in the surface layer volume with decreasing particle size. We may conclude that processes at the surface layer can be represented by a local anisotropy factor describing the arrangement of atoms that, upon interaction with an incident radiation, leads to a chaotization of the light-induced dipoles in this layer, which implies a lowering of their orientational ordering and dispersion of amplitudes. The chaotization reduces the strength of the resonant interaction between the atomic light-induced dipoles, thereby lowering the total polarizability. This in turn increases the plasmon frequency and the red shift compared to larger particles.

4.6 Medium shifts

The strongest applied feature of plasmonic nanoparticles is their ability to generate ultra strong electric fields for sensing objects in the neighborhood, so strong in fact as to make it possible to detect single molecules. However, plasmonic particles can also be used to probe their environment by means of how the plasmon exci-

tation itself is perturbed by its surrounding. Here the refractive index sensitivity is an important concept whereby the environment and its refractive index is sensed by the shift of the plasmon resonance. The early variants of surface plasmon resonance devices relied on the generation of surface plasmons in thin metallic films which were used as indicators of the changes in the refractive index of the close environment or ligands to surface binding. Thus that the plasmon maxima and extinction coefficient are sensitive to the dielectric properties, n.b. refractive index, of the materials close to the particle surface.[118,165–179]. Subsequently it was shown that the use of plasmons emerging from nanoparticles could give even higher sensitivity than biosensing devices based on thin film generated plasmons[180]. It has been possible to settle that the plasmon frequency in general changes in a regular manner upon change of the refractive index changes, and also that the size and shape of the particle matter a lot for how strong this dependency appears, where larger particles tend to increase the dependency and so also shaped particles compared to spherical ones.[181–183] Many recent articles are now available that explore and analyze these dependencies, using different methods, see e.g.[184,184–187].
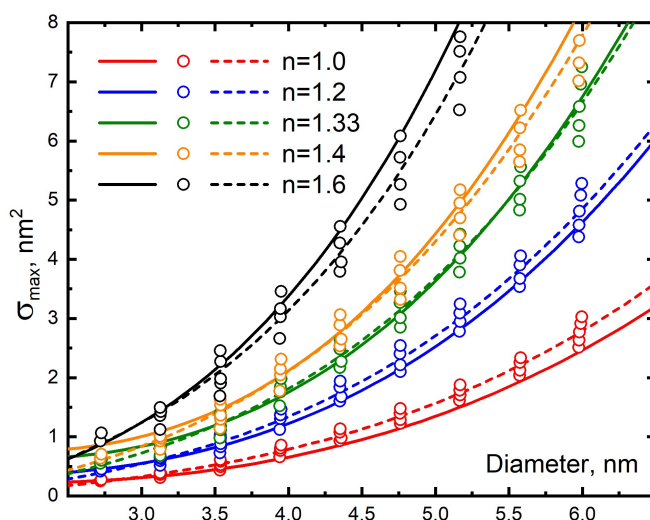

Fig. 20 Comparison of results from Mie theory and Ex-DIM model calculations of the SPR maximum as a function of Au nanoparticle size for different refractive indices of the ambient medium. Mie theory calculations obtained with size correction for the dielectric constant of Karimi[130] are given as solid lines. Discrete Ex-DIM data are given as hollow circles and approximating functions are marked as dashed lines. From Ref.[124]

It can in this context be relevant to recall some facts from classical dielectric theory assuming a bulk dielectric constant. According to this theory the frequency of the plasmon resonance of a metal particle ω_{pl} (the first dipole resonance) in a small sphere depends on the real dielectric constant of the ambient medium (ε_m) as $\omega_{pl} = \omega_p / \sqrt{\varepsilon_{ib} + 2\varepsilon_m}$. The parameter ε_{ib} reflects the contribution of interband transitions to the dielectric function, ω_p is the plasma frquency. This simple relation tells that the surface plasmon resonance experiences a red shift increasing with increasing dielectric constant of the medium. In the dipolar approximation the extinction cross section of a metal nanoparticle

with dielectric constant $\varepsilon' + i\varepsilon''$ and radius R increases with ε_m (λ is the light wavelength) [176,188]

$$\sigma_{ext} = 24\pi^2 R^3 \varepsilon_m^{3/2} \varepsilon'' / \lambda [(\varepsilon' + 2\varepsilon_m)^2 + 2\varepsilon''^2]. \qquad (32)$$

Thus in Ref. [124] it was studied to which extent these relationships hold in the small size range, below 10nm. Figure 20 indicates that the maximum shows an accelerated growth as the medium refractive index grows for any given particle size in this region. Also Mie theory data, taking into account of a size correction to the dielectric constant [130,189], are shown in Fig. 20. A general correlation emerges between Ex-DIM and the Mie theory, albeit with a small, discrepancy for higher refractive indices.
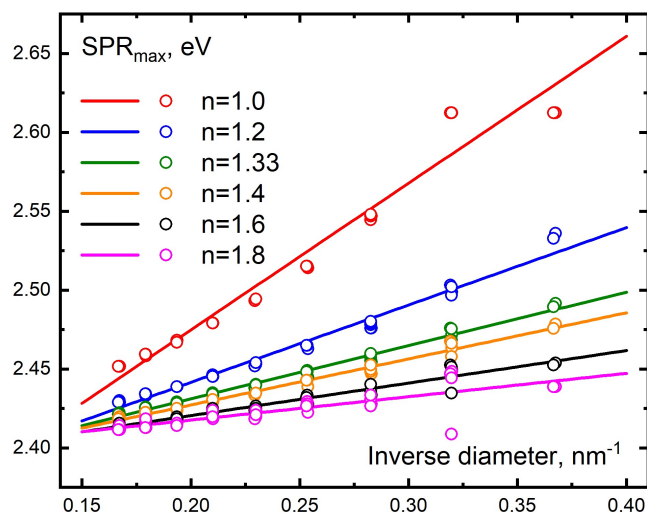
Fig. 21 SPR maximum of Au nanoparticles (in eV) versus their inverse diameter at different values of the refractive index of an ambient medium – discrete Ex-DIM data (hollow circles) and approximating functions (solid lines).From Ref. [124]

Fig.21, demonstrating plots of absorption band maximum on the inverse particle diameter at various values of the refractive index where only small deviations from linearity for the high index data are observed. Thus the classical relation above basically also holds for the small sizes. As the particle size increases, the influence of the medium increases the maximum extinction cross section and decreases red shift. Thus wee see regular trends for these aspects. Fig. 22 shows the dependence of the plasmon resonance maximum on the refractive index of the environment for different particle sizes. One notices an increase of the red shift with increase of refractive index of the medium, with the red shift becoming anomalously strong in this small size range size for a given medium, much stronger than for larger particles beyond 8 nm. As discussed in the previous section this observation can be referred to the chaotization of atomic dipoles of the surface volume and that the surface volume to total volume ratio becomes essentially larger.

4.7 Refractive index sensitivity

The refractive index sensitivity (RIS), defined by the ratio of the resonance wavelength shift to the change of refractive index of
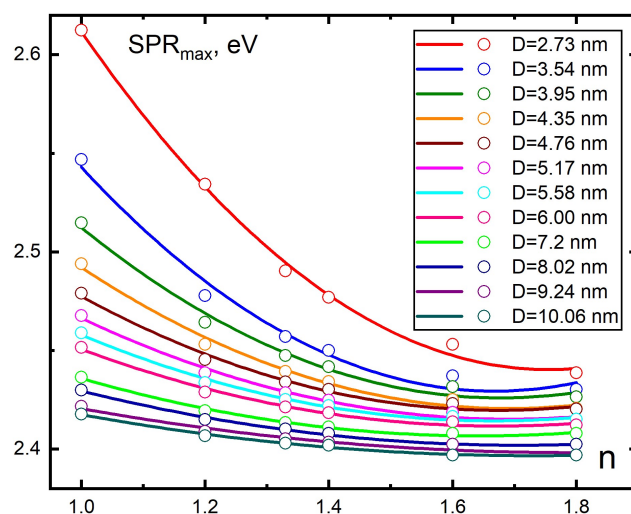

Fig. 22 SPR maximum of Au nanoparticles (in eV) versus the refractive index of an ambient medium for Au nanoparticle sizes in the range 2.73 – 10.6 nm: discrete Ex-DIM data (hollow circles) and approximating functions (solid lines). From Ref. [124]

surrounding medium, is an important concept for biosensing using plasmonic particles with numerous applications. Here the character of this factor for small particles becomes extra important to scrutinize owing to the above commented great utility of small particles in the context of biostructures like protein pockets, cell channels etc. As already stressed in this review we then enter into a surface physics domain and a domain where the mean free path of the conduction electrons may exceed the particle size and therefore is associated with limited applicability of using the bulk dielectric constants.

Mie theory results in Fig. 23 shows the dependence RIS on Au particle diameter for an aqueous medium. The size correction of the Mie theory for the Au dielectric constants was taken from Karimi[130]. Two opposite trends are found:— a decrease in RIS in the ultra-fine size range and an increase in RIS in the large particle range, with a minimum at 10 nm. These two trends converge at the minimum. It is to be noted that the anomaly in the ultra-fine range holds only at small values of the refractive index values $n \leq 1.33$. Fig. 24 demonstrates the corresponding results using Ex-DIM dependence of RIS on the particle diameter for aqueous media in the ultra-fine particle range. The difference for RIS magnitudes for 8–10 nm particles between Ex-DIM and Mie can probably be related to differences in the physical mechanisms underlying the models. The results of Fig. 23 and 24, showing RIS anomaly for small size particles finds an explanation in that the relative extent of its surface layer ($\Delta R/R$) rapidly decreases with particle growth. Here the extent ΔR weakly depends on the radius at a given value n[124]. This means that the contribution of the surface layer reduces with increasing particle radius.

The results of Ex-DIM calculations of the local fields inside and around nanoparticles of different sizes in the surrounding dielectric medium are collected in the figure 25 with refractive index values in the range n = 1.0–1.8. This figure demonstrates that the field strength grows with increasing refractive index, as well
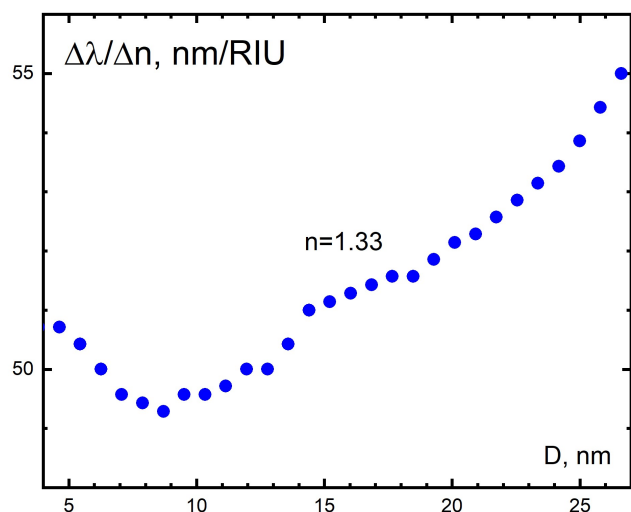
Fig. 23 Dependence of the refractive index sensitivity (RIS) of Au nanoparticles with sizes 5–27 nm at the refractive index of aqueous medium (n=1.33). The Mie theory calculations with size correction for the Au dielectric constants by Karimi [130]. From Ref. [124]
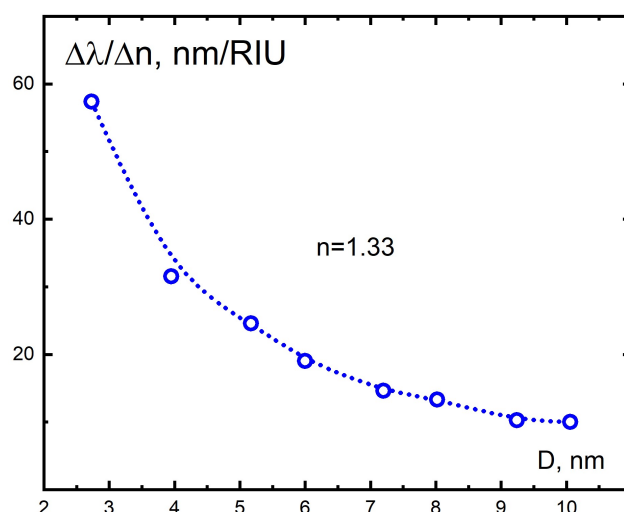

Fig. 24 Refractive index sensitivity (RIS) of Au nanoparticles versus nanoparticle size in the range 2.73 – 10 nm (an enlarged fragment of Fig. 23 in the ultra-fine size range 5–10 nm) at the refractive index of aqueous medium (n=1.33). Ex-DIM calculations. From Ref. [124]

as with particle size. (see also Fig. 10 in Ref. [124]). However, the increase in field strength with growing particle size is less pronounced. That is, the effect of the medium is dominant. The results of calculations for vacuum (n=1) in Fig. 25 demonstrate the minimum variation of field strength as a function of size (note the different colourbar scales for different sizes).

The figure also indicates that the field strength receives a maximum at a distance above the poles of the particle, while it is weaker right at the surface and also that with larger refractive index of the surrounding medium the localization of that maximum moves farther from the surface.

In conclusion, from the work in Ref. [124] it is clear that a plasmonic nanoparticle reacts to its environment by shifting the plasmon resonance towards longer wavelengths and by increasing its amplitude thus following the general trend for larger particles [173–178]. This is due to the formation of a dipole-polarised layer of molecules on the inner surface of the dielectric cavity in which the nanoparticle is immersed and an increase in the local field inside this cavity.

With a larger refractive index of the dielectric medium this field increases, creating a higher polarization of the molecules in the medium at the wavelength of the plasmon resonance. As discussed, there is a relation between this medium effect and the trend for the spectral red shift, but in both cases there is an accelerating effect for smaller particles (see Fig. 3 in Ref. [124]) It is noteworthy that with the growth of the refractive index of the ambient medium, the perturbed part of the surface layer of particles expands (see Fig. 8 in Ref. [124]).

Following the results of Ref. [124] it is clear that for the ultra-fine particle regime the contribution to the local field enhancement is dominated by the medium effect in comparison to the size effect, as manifested by the red-shift.

When the local field is enhanced inside the spherical cavity the induced atomic dipoles increase their amplitudes, so strengthen-

ing the dipole interactions with an additional chaotization at the surface layer. This contributes in turn to the penetration of chaotization into deeper layers of the particle. Interestingly the behavior changes trend at the 10 nm region. As discussed in Sec. 4.6 the change in red shift behavior – in that a anomalous red shift is introduced below this size. This seems to hold also for the medium effect – in fact in Ref. [124] a corresponding anomaly for the refractive index sensitivity was predicted and that this factor changes its trend from decreasing to increasing passing through a minimum, see Figure 24. Again this must be associated to change in the physics when the relative volume of the surface layer compared to the full volume of the particles increases . In this case, the sensitivity to the refractive index reaches a minimum value in the size range of 8–10 nm. According to the available data, e.g. [173,176], with further growth of particle sizes up to 20–30 nm and much above, the sensitivity to increasing refractive index grows again due to enhancement of the local field in the dielectric cavity with increasing refractive index and strengthening of the processes responsible for the red shift of the plasmon resonance maximum in the "large" particle range [164].

4.8 Thermoplasmonics

Thermoplasmonics constitutes one of the most attended application areas for nanoparticle plasmonics. The ability to generate extremely intense near-fields that produce concentrated local heating has a number of implications within biotechnology. One of the most prominent implications being the ability to break membranes of "bad" cells or bacteria. The therapeutic effects are here obtained by means of hydrodynamical effects generating vaporization bubble pressure from the heated nanoparticles when bound to malignant cell membranes or malignant neoplasms. The use of nanoparticles significantly reduces the intensity threshold of pulsed laser radiation to avoid damage effects on normal cells, and to localize the destructive temperature field near the

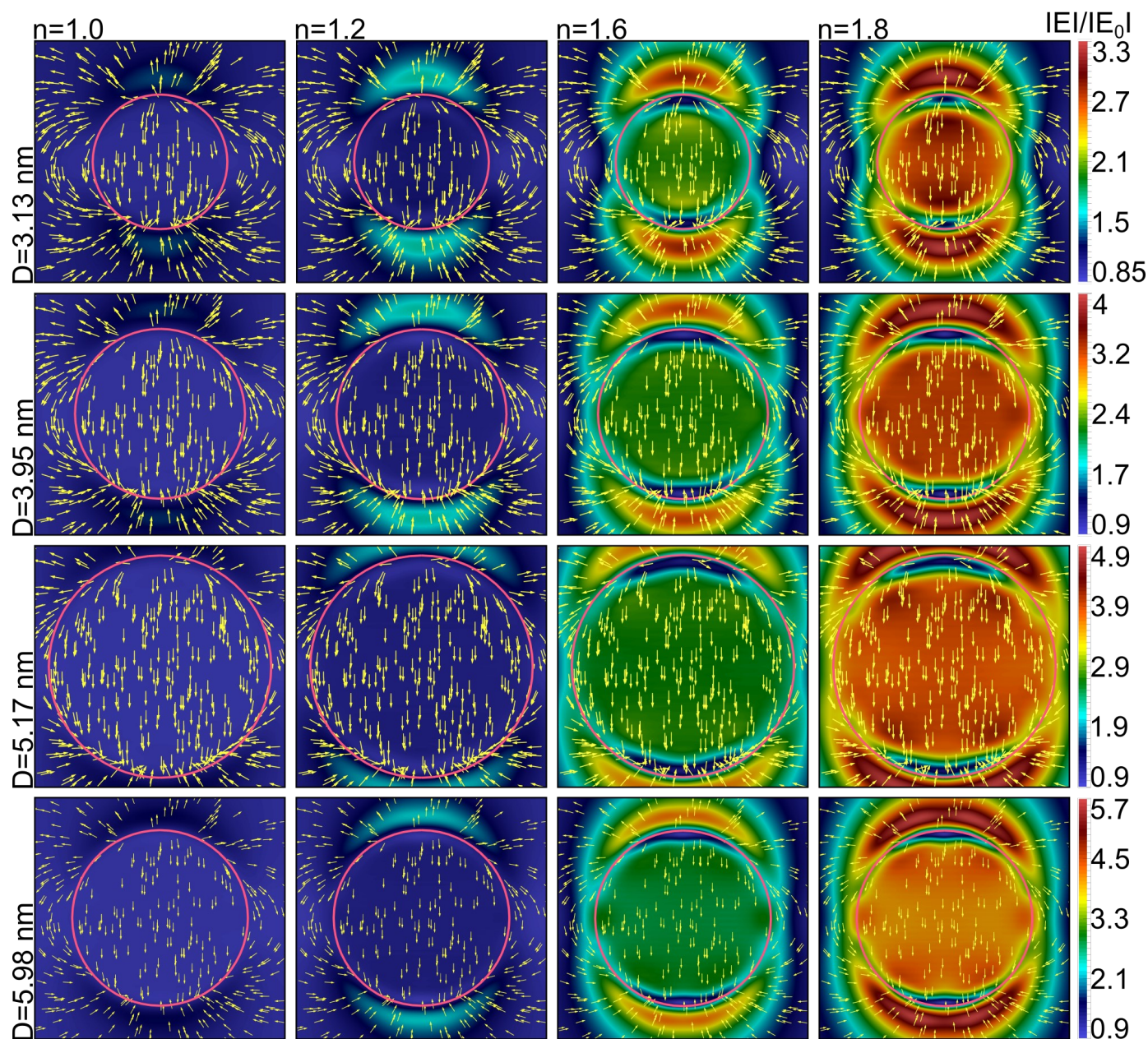Physical Chemistry Chemical Physics Accepted Manuscript

Fig. 25 Distribution of the field strength modulus ($|E|/|E_0|$) and the field directions inside and around the Au nanoparticles with diameters of 3.13, 3.95, 5.17, 5.98 nm as function of the refractive index of the ambient media $n=1.0$; 1.2; 1.6; 1.8 at the wavelength of the SPR maximum. The largest particle with a diameter of 5.98 nm with the field distribution image (in the bottom row) is reduced in order to cover the field distribution pattern around the particle. Polarization is vertical. Color bars used are different for the different sizes due to the large variation in the field amplitudes. From Ref. [124]

particle. Anticancer therapy by thermoplasmonics has thus generated a manifold of biomedical studies, see reviews in [190–192]. Thermoplasmonics has found important applications also in other areas, like nanosensorics, plasmonically enhanced Raman scattering, waveguiding, photoacoustic imaging and near-field heat transfer using nanoparticles. However, "thermoplasmonics" can also have a somewhat different meaning, namely how temperature perturbs the properties of nanoparticles, like crystal structure, particle shape or the light matter interaction that generates the plasmon resonances. This is important knowledge as when the particle is heated too much it may weaken or even completely loose its plasmonic property. The heating is caused mainly by the exciting laser light but also by that the heated medium surrounding the nanoparticle by the super concentrated near-field can further warm to the particle itself. Thus for each experimental setup there is an optimum laser effect for using nanoparticle plasmonics that is important to identify.
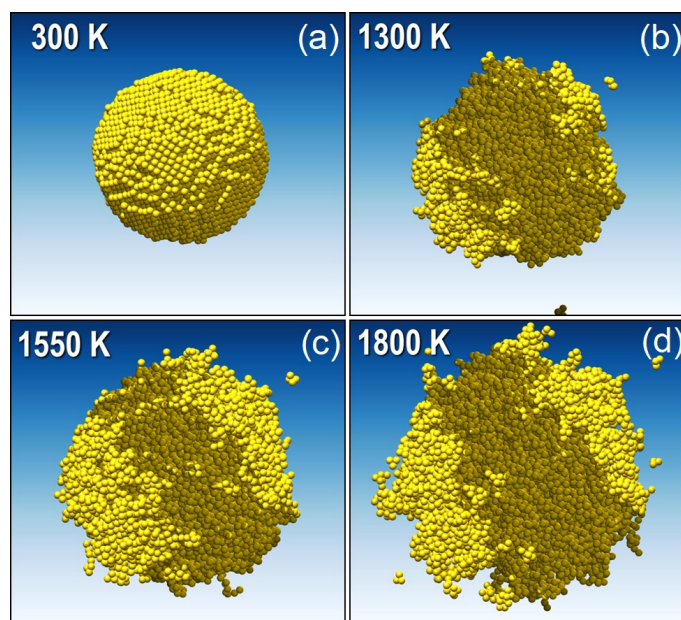

Fig. 26 Reactive force field molecular dynamics simulations of the evolution of the Au nanoparticle shape upon temperature growth – from the initial state at room temperature (D=6 nm) directly to extremely high temperature values much above the melting point. From Ref. [193].

A particularly important scenario takes place when the nanoparticles transfer into the liquid state as a result of intense laser radiation [194–196]. Quite drastic change can then be expected for the optical properties, which also can become non-linear in this temperature regime [197]. Moreover, the melting nanoparticles can then react with the heated environment generating crucial side effects. Motivated by these facts, Ex-DIM calculations were carried and analyzed in Ref. [193] in order to find the underlying causes for temperature changes of the plasmonic properties and to establish correlations between structural modification of the crystal lattices, the dynamics and the phonon relaxation with the plasmonic generation covering a variety of temperatures up to melting and beyond as seen in Fig. 26.

Here structural data were obtained by means of molecular dy-

namics and a semi-empirical theory for relaxation constants of the plasmonic excitation states was employed, making also comparisons with multilayered Mie theory.

Much of the underlying features behind the Ex-DIM analysis of the thermoplasmonics for ultra small nanoparticles can be found in Figure 27 (I, III), displaying temperature dependencies of the atomic mobility in a gold nanoparticle, the spectral density of states and distributions of the local fields inside the particle and near its surface with rising temperature. Furthermore the figure demonstrates the chaotization of the crystal lattice structure and the increase of vibrational amplitude with growing mobility of atoms. It is clear that rising temperature gives a geometry change that involves a randomization of the lattice and an increase in the crystal lattice constant. The effect of structural change and randomization of the crystal lattice on the extinction spectrum is shown in Figure 28(a,b) where the room temperature relaxation is kept constant. It is clear from Figure 28 that the structural change and randomization of the crystal lattice effect from the temperature is almost negligible. The relaxation factor is here clearly the most important mechanism. However, both factors should still be kept in mind in order to interpret the overall results presented in Figures 29 and 30.

As can be seen from the series of images obtained from Ex-DIM in Figure 27 (IV), there is an inhomogeneous local field distribution inside the heated particle and near its surface. The maximum values inside the particle resides near its poles for the ordered crystal lattice at cold temperature, but as the temperature rises, the pole fields decrease and deviates from a classic spherical configuration. Here the internal local fields inside the particle experience a decrease in the amplitude with increasing temperature. Figure 29 clearly demonstrates the suppression of the surface plasmon resonance with increasing temperatures up to melting temperature (which in Ref. [193] is calculated to 1130 K from the Gibbs-Thomson equation). From Fig. 30 it is seen that the suppression of the surface plasmon resonance with increasing temperatures behaves in a similar fashion independent of the particle size. Compared to multilayered Mie theory the Ex-DIM model predicts faster decrease of the SPR maximum at lower temperatures see Figure 31, with a more linear correlation between the maximum plasmon extinction coefficient and temperature being predicted. A better visibility of the temperature suppression is given by the differential spectra between the going from solid to melted particle shown in Figure 29(c,d) which also displays the small red shifting of the resonance with temperature.

An experimental validation is given in Figure 31 which demonstrates a comparison between Ex-DIM (6 nm particle), Mie theory (40 nm particle) experimental data (40 nm particle) for plasmon maximum extinction coefficients with rising temperature. It is notable here that despite the large difference in particle size (6 vs 40 nm) there is a better representation of Ex-DIM with respect to Mie theory concerning both the slope of the curves and the melting points with complete plasmon depletion.

In conclusion, it is clear that the heating of plasmonic nanoparticles generates and enhanced electron-phonon scattering with entailed increased plasmon relaxation and a change of dielectric constant. There are also strong structural variations, both for
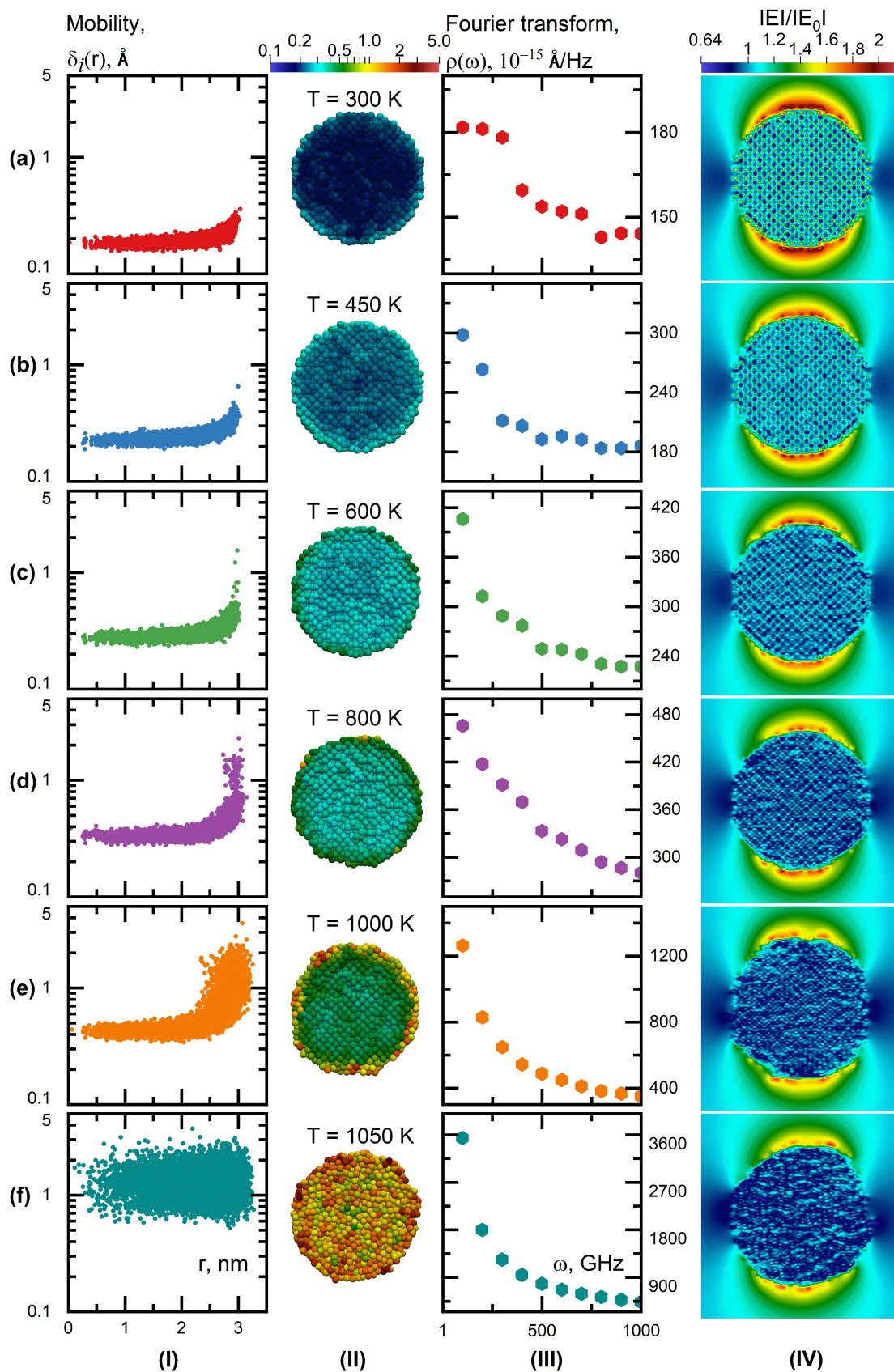
Fig. 27 Temperature dependencies (columns I, II, III, IV) of the atomic mobility in an Au nanoparticle with radius R=3 nm (I), view of this mobility in the particle cross-section with internal structure (II), the Fourier transform of the time dependent modulus of the i-th atom coordinate ($|\mathbf{r_i(t)}|$) as a spectral density of states in a unit range $\Delta\omega_i$ within in the frequency range up to 10^{12} Hz (III), and distribution of the local field inside the particle and near its surface with rising temperature (for vertical polarization) (IV). From Ref. [193]

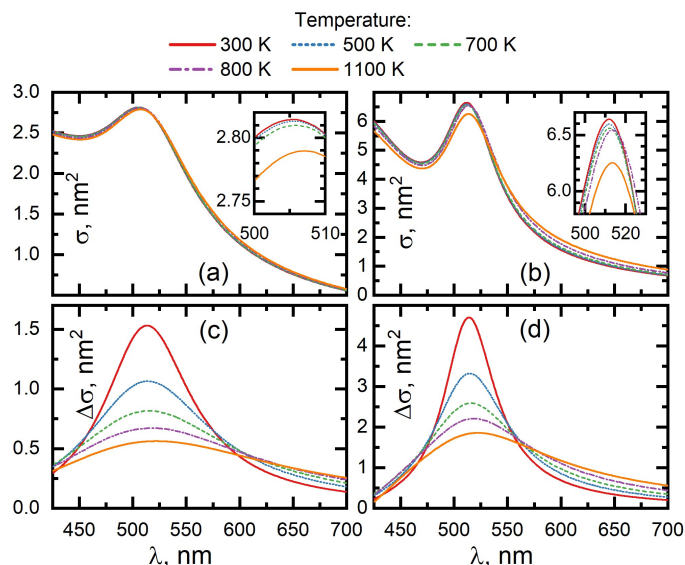Physical Chemistry Chemical Physics Accepted Manuscript

Fig. 28 Structure effect on the extinction spectra for the 6 nm Au nanoparticle from Ex-DIM calculations. Geometries are taken at different temperatures but with relaxation constant fixed at the room temperature — $\Gamma_i(T = 300\ K)$. Insets show the enlarged fragments of spectral curves near the surface plasmon resonance maximum. Plasmonic absorption spectra of the 6 nm Au nanoparticle with subtracted interband absorption band of gold at different temperatures. (a,c) — in vacuum ($n_0 = 1$), (b,d) — in medium with a refractive index of $n_0 = 1.33$. From Ref. [193]
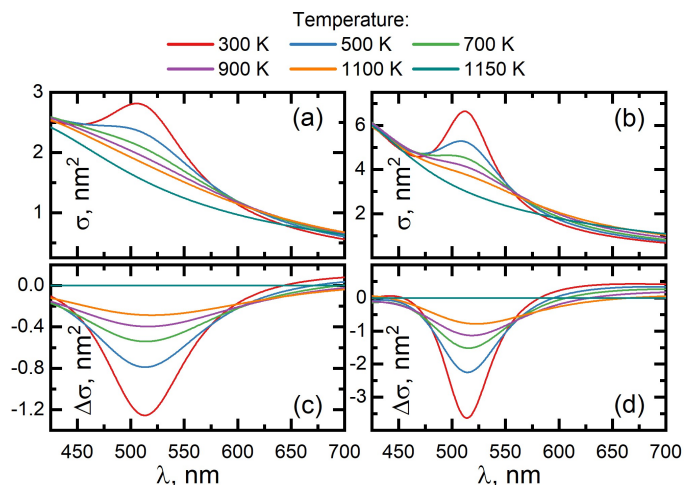

Fig. 29 Extinction spectra variation for the 6 nm Au nanoparticle with suppression of surface plasmon resonance in the temperature range 300 — 1150 K (Ex-DIM calculations). Variation of differential extinction spectra with suppression of surface plasmon resonance in for temperatures 300 — 1150 K (all curves were subtracted from the spectral dependence for $T = 1150$ K). (a,b) — in vacuum, (b,d) — in medium with refractive index n_0=1.33 (b) From Ref. [193]

the inner lattice atoms and for the overall shape of the particles, the latter becoming chaotic towards melting. For more complex particle shapes additional resonances are acquired as a result of shape change also at lower temperatures, which will appear as an overall broadening of the plasmonic spectrum. It could be established that the radial dependence of the mobility is much higher near the particle surface than in the central part, reflecting that the melting starts from the surface and progresses inwards. It is also clear that the surface melting occurs at a much lower temperatures than core melting, corroborating with experiment [128]. At melting the mobility becomes homogenized over the particle volume before the particle totally disintegrates. In between, however, the mobility demonstrates staged features thus increasing towards melting in a non-monotonous way. The study in Ref. [193] could numerically establish the depletion of the plasmonic generation with rising temperature by means of Ex-DIM calculations. That was also corroborated from analysis of Fourier spectra representing the average amplitude of phonon oscillations with respect to frequency. It could thus be concluded that it is the electro-phonon coupling, which increase the relaxation constant, that is the major reason for the plasmon depletion. The electro-phonon coupling thereby being significantly more important than the chaotization of the internal nanoparticle structure. The suppression of the plasmon starts at temperatures well below the melting point going up to full suppression at melting, something that equate with the importance of the surface for plasmon generation and that the surface melts at smaller temperatures than what the full particle does. These are thus important features to learn in order to understand the plasmon behaviour of ultra-fine

nanoparticles at shifting temperatures.

5 Discrete interaction models versus classical models for plasmonics

The finite difference time domain (FDTD) method [47] is one of the key methods for describing the optical properties of nanostructures. This method has been developed since the middle of the 20th century and has become one of the most popular methods of numerical electrodynamics. The method is based on a discretization of Maxwell's equations written in differential form. Unlike other methods, such as the coupled dipole approximation, the mathematical model underlying FDTD does not use approximations and is accurate for classical electrodynamics. The equations are solved by the finite difference method on two nested structured rectangular grids, one of which is used for calculating electric fields and the other for magnetic fields. The method makes it possible to obtain in one calculation the transmission and reflection spectra and the field distribution in the computational region, taking into account both the complex composite structure of the system under study and the optical properties of the materials used. The possibility of using periodic boundary conditions and optimization by taking into account the symmetry of the unit cell of the periodic structure can significantly speed up the calculation process. Also, the method allows parallel computations using high-performance cluster systems.

COMSOL Multiphysics [48] is based on Maxwell's equations, calculated in the frequency domain, and can be used for computing optical properties, including the absorption and scattering cross sections of plasmonic nanoparticles of arbitrary shape. In contrast to FDTD, the calculation of optical properties of nanoparticles with strongly nonspherical shapes containing sharp corners are more accurate due to the use of trigonal meshes in this method. This makes it possible to understand how the optical properties
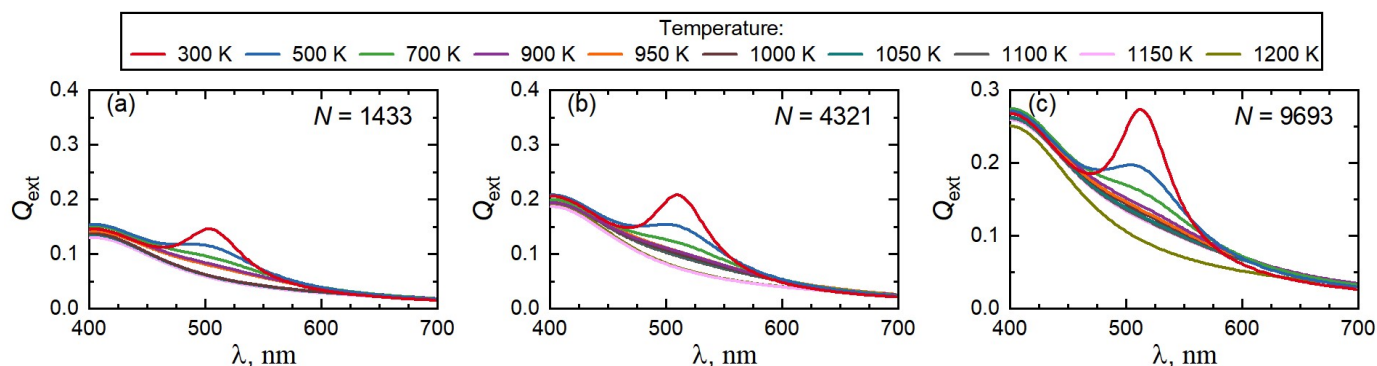
Fig. 30 The plasmonic resonance as a function of temperature for three particles with 1433, 4321 and 9693 atoms. The melting temperatures of the particles are 977 K, 1103 K and 1160 K, respectively. From Ref. [193]
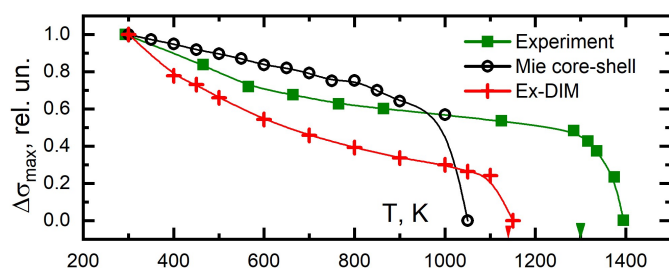

Fig. 31 Suppression rate for SPR maximum versus temperature growth calculated by the multilayered Mie theory in the case of inhomogeneous radial dependencies of the dielectric constant in a 6 nm Au nanoparticle (circles), by Ex-DIM with homogeneous radial dependencies of dielectric constant (cross dots) – both in vacuum ($n_0=1$), and an experimental extinction spectrum of 40 nm Au nanoparticles on quartz substrate (square dots) [198]. Arrows on the temperature scale show the melting points for the 6 nm and 40 nm nanoparticles. From Ref. [193]

of a nanoparticle depend on its size and changes in the local environment, as well as how the near-field enhancement is affected by the plasmonic interaction of nearby nanoparticles.

The discrete dipole approximation (DDA), briefly reviewed already in Sec. 2 is a method for computing scattering of radiation by particles of arbitrary shape and often by periodic structures. Given a target of arbitrary geometry, one seeks to calculate its scattering and absorption properties by an approximation of the continuum target by a finite array of small polarizable dipoles, e.g. [112,199,200]. Light-induced dipoles interact with each other, which is described by the coupled dipole approximation (CDA), e.g. [201]. This technique is used in a variety of applications including nanophotonics.

Discrete medium description methods such as DDA make it possible to investigate arbitrary shapes as well as the possibility of introducing anisotropy within the nanoparticle. However, this approach has some limitations in the number of dipoles used, which reduces the accuracy of the representation of complex shapes. An alternative approach is to numerically solve the electromagnetic scattering equations using the boundary element method (BEM) [202]. BEM, in general, is a numerical computational method for solving linear partial derivative equations that have been reformulated as integral equations defined at the boundary of the system. Ultimately, it allows for greater control over the details

of the object under study – see e.g. Ref. [203]. As an example, BEM has been successfully used to study the radiative properties of plasmonic core-shell nanowire resonators [204], and for modeling multiple scattering of plasmonic nanowires [205].

The T-matrix method has proved to be highly efficient and is widely used in the calculation of electromagnetic scattering of single and composite particles. This method is one of the most powerful and widely used tools for accurately computing light scattering by non-spherical particles, based on directly solving Maxwell's equations, see e.g. [206,207].

The generalized many-particle Mie theory [208,209] is often used to calculate the interaction of plane electromagnetic waves with systems of spherical particles. Compared to general methods for solving an electromagnetic problem (for example, FDTD, COMSOL), Mie's theory allows for faster solutions and often more accurately but only for spherical particles. The basis of the many-particle Mie theory lies in classical one-particle theory. It is based on expanding the solution of the wave equation in a homogeneous medium in vector spherical functions. The electromagnetic field is presented in three components: the incident and scattered waves outside the particle and the field inside the particle. The solution to the scattering and absorption problem is achieved by fulfilling the boundary conditions at the particle/environment interface.

The many-particle Mie theory considers the interaction of a plane electromagnetic wave with a system of spherical particles. The calculation of the electromagnetic response of each particle is similar to the single-particle Mie theory, but the wave incident on a given particle is the sum of the external wave and waves scattered by other particles in the system and can be carried out using, for example, the Gaunt coefficients. Thus, the solution of the scattering and absorption problems is given by the solution of the system of linear algebraic equations [210,211].

As for theoretical models in general, discrete interaction models, including their extended versions, are associated with merits and limitations. There are some particular advantages with the DIM models over classical models that consider the nanoparticle material as a continuous medium. Here, the Ex-DIM model makes it possible to study the properties of arbitrarily shaped particles and makes it possible to obtain information on the detailed distribution of local electromagnetic fields inside the particle - liter-

ally around each atom, as well as around arbitrary defects, and to evaluate how these defects affect the optical properties and the ability to enhance local electromagnetic fields. In continuum models, these fields are visualized as a continuous homogeneous background inside the particle, whereas in reality this is clearly not the case.

In particular, DIMs make it possible to detect the surface layer of atoms in a nanoparticle, which exhibits strong inhomogeneities of the local field due to the anisotropic surrounding of each atom by neighboring atoms. This distinguishes the surface layer from the inner regions of the nanoparticle, where the environment of each atom is isotropic. In addition, Ex-DIM makes it possible to study the influence of lattice defects or its partial chaotization on the optical properties of the nanoparticles, their ability to enhance the local field, which is impossible in the case of continuous medium models, in which the influence of chaotization cannot be taken into account if interatomic bonds are preserved. Besides that, when investigating the use of SERS to detect impurity molecules in the presence of plasmonic particles, Ex-DIM reveals an important feature namely that the maximum enhancement of the local field near the surface of particles is shown to take place not on the surface of the particle itself, but somewhat further from its geometric surface, which is not detected using classical methods.

Figure 32 illustrates a comparison between the results obtained from calculating the local field distribution around a gold nanotetrahedron using FEM implemented in COMSOL Multiphysics [48] and Ex-DIM. The figure depicts a matching pattern of field distribution with only a slight difference in amplitude, which is not fundamental when considering the normalized values.
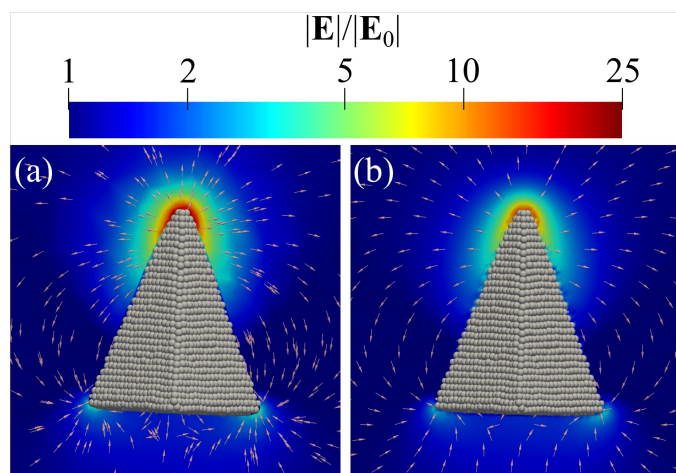

Fig. 32 Comparison of the local field distribution around a gold nanotetrahedron consisting of 26000 atoms (normalisation to the incident field strength), calculated with finite element method (COMSOL) – (a) and Ex-DIM – (b). Polarisation direction from the top to the middle of the bottom.

It is also worthwhile noting the possibilities that Ex-DIM provides for the study of alloys and mixtures of atoms capable of forming crystal lattices with an arbitrary ratio of the number of different atoms. Obviously, when using classical models, experimental data on optical constants of alloys with arbitrary ratio

of fractions of different atoms are necessary to solve Maxwell's equations. New opportunities of Ex-DIM are opened when it is combined with the use of molecular dynamic simulations, e.g. the LAMMPS (Large-scale Atomic/Molecular Massively Parallel Simulator) software [212]. This provides information on the stability of the crystal lattice composed of different atoms (alloys) and also opens up the possibility of studying the optical properties of amorphous and porous metals, as well as metallic foams [213]. In addition, Ex-DIM makes it possible to study the effect of external mechanical impact on nanoparticles, namely their one-dimensional stretching or compression deformation on optical properties.

All that is said above refer to metallic plasmonic nanoparticles, but the same tasks can be investigated with the help of Ex-DIM in dielectric nanoparticles, including studies of both optical properties and the possibility of use in tasks of photovoltaics. We can foresee a multitude of applications of DIMs as well as development of the models and merging to other models, classical or quantum, in a multiscale setting. Below we present an outlook that shortly speculates on a few possible lines of development and applications which seem extra promising.

6 Outlook - Opportunities and challenges for ultra-fine particle plasmonics

6.1 Ex-DIM thermodynamic models for plasmonic heat generation

As discussed in section 4.8 a very useful aspect of metal nanoparticles is that the enhanced light-matter interaction at their plasmonic resonance induces very high temperature increments, highly localized in space and time. Such increments can actually be created with moderate light intensity without thermobleaching or photobleaching of the absorbers. [214] The ability to release heat on the nanoscale has impacted a broad range of research activities, from biomedicine and imaging to solar light harvesting and catalysis. [215] Plasmonic photothermal therapy can be promoted by thermally selective laser irradiation of biostructures, like malignant tumor cells, when labeled with plasmonic nanoparticles. Here one can suggest the selective exposure to be based on either employing DNA aptamers or antibodies attached to the surface of the plasmonic nanoparticles, which allows them to bind to specific membrane proteins of the malignant cells. The use of nanoparticles significantly reduces the intensity threshold of pulsed laser radiation to avoid damage effects on normal cells, and to localize the destructive temperature field near the particle [22,25,26]. The advancement in theory of ultra-fine plasmonics will enable to more precisely define the nanoparticles for plasmonic field distributions and hot spots with optimum heating of the cell membrane, but at the same time avoiding to deplete the plasmon excitation itself by heat – thus to optimize the heat effect on the plasmonic nanoparticle for given laser characteristics - intensity, wavelength and pulse duration. [22,216,217] We see opportunities in joining Ex-DIM method with thermodynamic models which can make it possible to solve the dynamic problem of heating by the plasmonic nanoparticles taking into account not only their special characteristics but also the parameters of the laser pulses [218]. The energy of electromagnetic radiation absorbed by
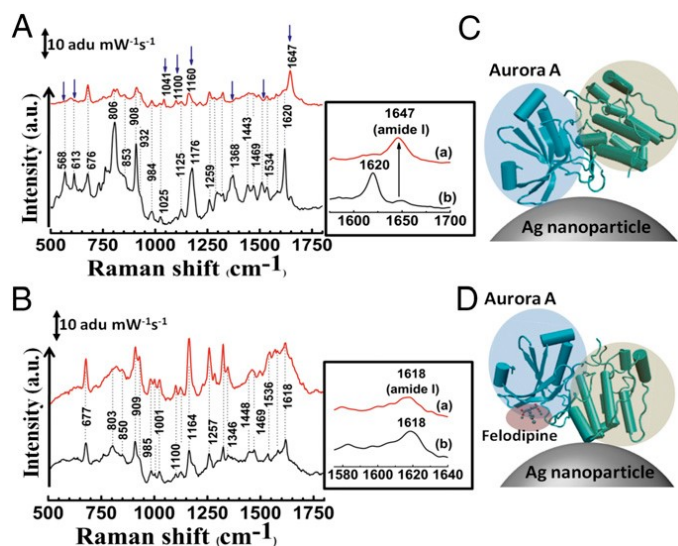
Fig. 33 SERS study of specific binding of felodipine to Aurora A. (A) SERS spectrum of Aurora A (black) and Aurora A complexed with felodipine (red). (B) SERS spectrum of Aurora B (black) and after treatment with felodipine (red). Reproduced from Ref. [226] with permission from PNAS, copyright 2014.

Fig. 34 Schematic overview of TERS. Reproduced from Ref. [230] with permission from IEEE, copyright 2017.

the particle is then predicted using the Ex-DIM module by calculating its temperature dependent absorption cross section and then transferred to the heat exchange module as input parameter along with the external radiation intensity. New possibilities for experiments on hypothermia of malignant cell membranes are here opened by using strongly non-spherical particles, e.g., plasmon stars[219].

6.2 Ultra-fine Plasmonic Nanoparticles for Enhanced Photoacoustic Imaging

Photoacoustic imaging[220] involves non-ionizing laser pulses delivered into biological tissues that are absorbed and converted into heat, leading to transient thermoelastic expansion and therefore wideband ultrasonic emission. As a result, the magnitude of the ultrasonic emission, reveals physiologically specific optical absorption contrast.[221,222] One can here foresee multiple advantages of using ultra-fine nanoparticles, namely to focus heat, to navigate in the tight biostructural environments, and being easier to rinse from tissue and body than larger nanoparticles. The control of heat is necessary and to establish a balance between action of heat (i.e. the photoinduced thermal increase of target volume) and the destructive action on both the environment and the nanoparticle plasmon generation. We can anticipate applications in many areas, for instance in tracing early stages of neurodegenerative disease, which are governed by brain proteinopathies, where the authors have been active.[223–225]. Here one can apply simulation guided ultra-fine plasmonic nanoparticles that are conjugated to targeting biomarker probes that bind to protein, plaques or proto-fibrils.
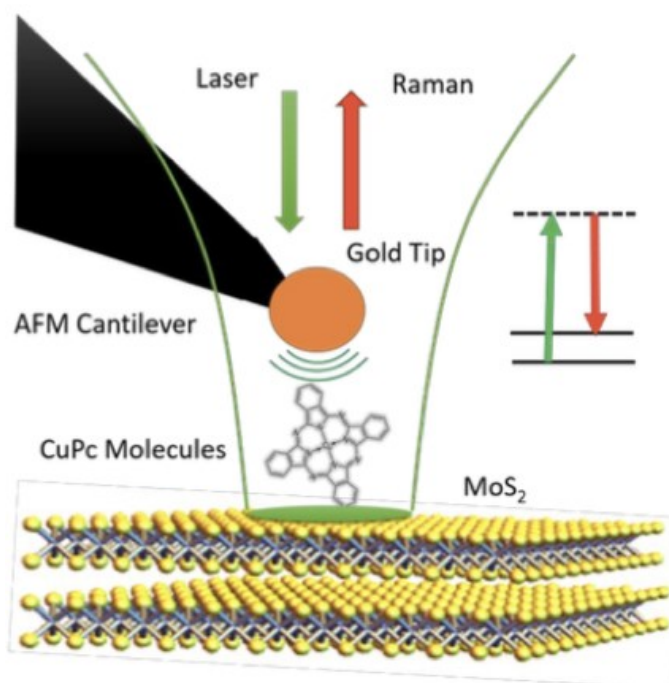
6.3 SERS — Surface Enhanced Raman Scattering

SERS constitutes perhaps the most well-known application of plasmonics and has been a frequently used tool for identifying the binding sites of small molecules on therapeutically important proteins[227–229]. As SERS can be performed for proteins at extremely low concentrations in their active state, the competitive binding versus noncompetitive binding and specific changes in the proteins upon ligand binding can be targeted. One can here foresee the use of Ex-DIM in the design of bioconjugated SERS reporter systems for binding to, and detection of, cancer cells or protein fibrils that are early hallmarks of neurodegenerative diseases. The full effect, thus plasmonic field enhancement and shifts in Raman signals and spectra, may in the future be simulated using multiscale techniques, taking account of the main interactions in the compound systems in addition to the light-matter interaction. In addition to the action of a plasmonic particle, it is relevant to trace the structural refinement when the biomarker approaches the protein and also the effect of the various binding situations on the actual Raman spectra, see Fig. 33. A developed combined SERS-simulation protocol may thus help converge potential of ultra-fine nanoparticles for diagnostic and therapeutic applications.

6.4 TERS — Tip Enhanced Raman Scattering

Sub-nanometer resolution under local plasmonic excitation can nowadays be obtained by the tip-enhanced Raman scattering (TERS) technique.[231] Its physical origin can be understood by a quantum mechanical interaction between a molecule and a highly confined plasmonic field, see the schematics in Fig. 34 (see[230]). Using the capability of designing ultra-fine plasmonic structures,
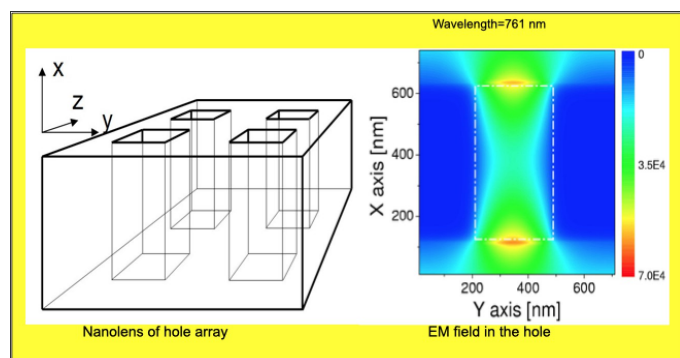
Fig. 35 (Left) thin film with holes working as a nanolens. (Right) the enhanced electric field at the top and bottom of a hole. Courtesy of Dr. Ying Fu
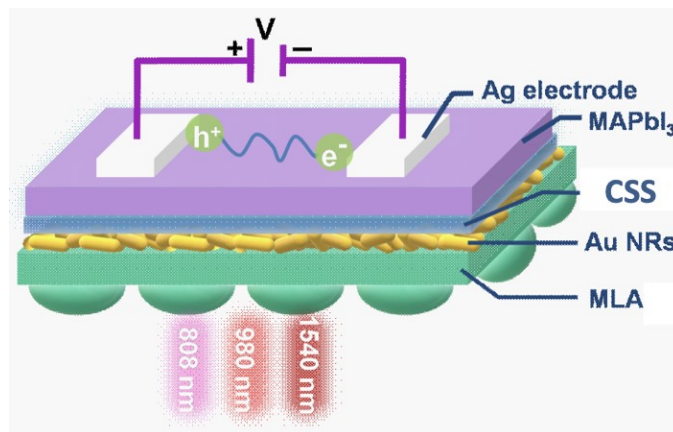

Fig. 36 Schematic illustration of a selective multispectral narrowband NIR photodetector at 808 nm, 980 nm and 1540 nm based on a hybrid structure. Reproduced from Ref. [233] with permission from Springer Nature, copyright 2020.

we aim to cope with the current possibilities for local plasmonic enhanced Raman images of single molecules where the spatial distribution of the plasmonic field is comparable to the size of the molecule. Here one takes account of the very subtle variations of the field distribution that emerge from the tip metal, and optimize the shape/size/material of the tip as well as the geometric configuration of the molecule surface complex. One thus designs the plasmonic particles and their confined super enhanced fields and hot spots at the sub-nanometer scale and calculate the Raman spectra induced by the field accounting also for the interactions with the substrate environment. Here one can with advantage apply the Raman theory and code accounting for confined position-dependent electromagnetic fields as derived by Duan et al.[232].

6.5 Plasmonic cascading

Plasmonic cascading is a concept that offers new opportunities in nanophotonics like in the area of IR solar cell harvesting and photodetection at the ultrasmall nanoscale. An example is to combine plasmonics with upconversion and microlens technologies [233]- either plasmonically enhanced fields by nanoparticles or by nanohole perforated thin films.

6.5.1 Plasmonic nanohole assisted IR upconversion

In a landmark experiment Ebbesen *et al.* [234] could observe an extraordinary increase in optical transmission for circular hole arrays in silver films for holes much narrower than the wavelength, in fact, the transmission exceeded orders of magnitude from what one can expect from the sum of the individual hole transmissions.[235,236].

In order to shed light on the issue for super transmission through hole perforated thin films, and in order to design nanodevices of applicable value, one can here consider the emergence of plasmon excitation in these systems when the dimensions are small, thus when dimensions of films and holes go below the limit where classical dielectric descriptions do not apply. In this limit an atomic scale interaction model is called for, thus suitable for our unique Ex-DIM code. The wave propagation in these perforated nanohole systems can so be optimized both for material and geometric configurations of the thin film. Here one can aim to couple these arrays with microlens upconversion technology,

to obtain a super concentrated upconversion, leading to a proof-of-principle that can be used both in photodetectors and for solar cell harvesting.

Another, related, prospect is to use DIM models for designing so-called picocavities. Benz et al demonstrated [237] that individual atomic features inside the gap of plasmonic nano-assemblies can localise light to volumes well below 1 nm^3, enabling optical experiments on the atomic scale, and could show that such atomic features can be dynamically formed and disassembled by laser irradiation. According to the authors such picocavity formation can access sub-molecular dynamics and open new possibilities for high precision sensors and single-photon strong-optomechanical coupling.

6.5.2 Plasmonic particle assisted IR upconversion

In Ref. [233] an optical cascade amplification strategy was used to overcome current shortages of individual IR photodetector amplifiers. Here multi-wavelength responsive core-shell structured UCNPs built for photodetection utilizing the cascade UCL amplification emit visible light under excitation of several IR wavelengths. One can thus cascade the superlensing effect and the plasmonic effect of dielectric microlens arrays and gold nanorods, respectively. In this way an upconversion luminescence enhancement by more than four orders of magnitude has already been demonstrated, see Figure 36. One can here seek to optimize the cascade function with respect to device configuration, structure and plasmonic material taking notice also of the effect of the strong local heat generation. Other plasmonic materials, like TiN [238] with more optimal heat endurance, lower loss and lower cost can be tested.

6.6 Optical forces

Optical force or optical force density give fundamental information on kinetic motion of condensed matter and of various optomechanical phenomena [239–242]. Such forces have an impact on
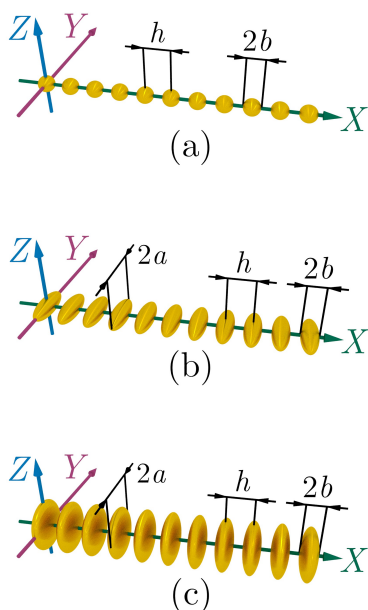
Fig. 37 Schematic representation of chained plasmonic nanoparticle waveguides consisting of (a) spheres, (b) prolate spheroids, and (c) oblate spheroids. Reproduced from Ref. [243] with permission from Elsevier, copyright 2018.

solid state systems whenever momentum is transferred from photon to material, like membranes, beams, cantilevers, waveguides, optical switches. They can be important in general for silicon devices and communication systems. Here we foresee that classical electro-magnetic theory can with advantage be joined with the Ex-DIM model to explore the action of optical forces at the very nano scale where the concept of a homogenized dielectric constant is no longer valid.

6.7 Plasmonic Waveguides

Because of the high confinement of electromagnetic energy, propagating surface plasmon polaritons (SPPs) have been considered to represent one of the best potential ways to construct next-generation ultra-small circuits that use light to overcome the limits of speed and energy consumption in electronics[244,245]. Being fabricated at the nanoscale they can be superior to chains of all-dielectric particles which have a much larger cross-sectional size and approach the size of a conventional optical fiber. By means of ultra-fine plasmonic particles, designed by Ex-DIM, it may be possible to significantly increase the transmission coefficient the chains of particles by putting them as close to each other as possible. In this case, the excitation and transfer interactions of at least a few higher-order multipoles, which rapidly attenuate with distance from the particle, should be taken into account, something that earlier has been neglected using the simplified dipole models. Here multipole decomposition could be derived directly from the Ex-DIM model. The optical properties of the waveguide including the dielectric permittivity of the nanoparticle material, are obtained from the solution of a self-consistent equation. As a complement, the optical properties of a plasmonic waveguide can then be obtained using the Generalized multi-particle Mie

theory[208] for spherical particles or the Finite Difference Time Domain method as well as COMSOL Multiphysics for the particles of arbitrary shape.

These are only a few highlighted examples out of many possible, that illustrate the great potential of discrete interactions models and their extensions for future collaborative studies with experiment and with wide ramifications in a diverse set of application fields.

Conflict of interest

There are no conflicts of interest to declare.

Acknowledgement

Notes and references

1 S. M. Morton, D. W. Silverstein and L. Jensen, *Chemical Reviews*, 2011, **111**, 3962–3994.

2 L. M. Liz-Marzán, C. Murphy and J. Wang, *Chem. Soc. Rev.*, 2014, **43**, 3820– 38222.

3 S. Maier, *Plasmonics: Fundamentals and Applications*, Springer, New York, NY, 2007.

4 M. E. Stewart, C. R. Anderton, L. B. Thompson and J. A. R. R. N. J Maria S K Gray, *Chem. Rev.*, 2008, **108**, 494– 521.

5 N. Jiang, X. Zhuo and J. Wang, *Chem. Rev.*, 2018, **118**, 3054– 3099.

6 G. Shvets and I. Tsukerman, *Plasmonics and plasmonic metamaterials: Analysis and applications*, World Scientific, 2012, vol. 4.

7 R. M. Stöckle, Y. D. Suh, V. Deckert and R. Zenobi, *Chemical Physics Letters*, 2000, **318**, 131–136.

8 S. Duan, G. Tian, Y. Ji, J. Shao, Z. Dong and Y. Luo, *Journal of the American Chemical Society*, 2015, **137**, 9515–9518.

9 G. Sun and J. Khurgin, *Plasmonics and Plasmonic Metamaterials*, 2011.

10 R. B. Schasfoort, *Handbook of surface plasmon resonance*, Royal Society of Chemistry, 2017.

11 V. Amendola, R. Pilot, M. Frasconi, O. M. Maragò and M. A. Iatì, *Journal of Physics: Condensed Matter*, 2017, **29**, 203002.

12 M. I. Stockman, *Optics express*, 2011, **19**, 22029–22106.

13 C. David and F. J. G. de Abajo, *The Journal of Physical Chemistry C*, 2011, **115**, 19470–19475.

14 A. S. Thakor, J. Jokerst, C. Zavaleta, T. F. Massoud and S. S. Gambhir, *Nano Letters*, 2011, **11**, 4029–4036.

15 X. Huang, P. K. Jain, I. H. El-Sayed and M. A. El-Sayed, *Nanomedicine*, 2007, **2**, 681–693.

16 J. R. Navarro, F. Lerouge, C. Cepraga, G. Micouin, A. Favier, D. Chateau, M.-T. Charreyre, P.-H. Lanoë, C. Monnereau, F. Chaput, S. Marotte, Y. Leverrier, J. Marvel, K. Kamada, C. Andraud, P. L. Baldeck and S. Parola, *Biomaterials*, 2013, **34**, 8344–8351.

17 O. Glembocki, S. Prokes, H. Szmacinski, J. Liu, F. Kub and C. Kub, Nanosensing: Materials and Devices II, 2005, p. 600809.

18 M. E. Stewart, C. R. Anderton, L. B. Thompson, J. Maria, S. K. Gray, J. A. Rogers and R. G. Nuzzo, *Chem. Rev.*, 2008, **108**, 494–521.

19 P. Anger, P. Bharadwaj and L. Novotny, *Physical review letters*, 2006, **96**, 113002.

20 B. Saute and R. Narayanan, *Analyst*, 2011, **136**, 527–532.

21 E. C. L. Ru, J. Grand, I. Sow, W. R. C. Somerville, P. G. Etchegoin, M. Treguer-Delapierre, G. Charron, N. Félidj, G. Lévi and J. Aubard, *Nano Letters*, 2011, **11**, 5013–5019.

22 A. S. Kostyukov, A. E. Ershov, V. S. Gerasimov, S. A. Filimonov, I. L. Rasskazov and S. V. Karpov, *Journal of Quantitative Spectroscopy and Radiative Transfer*, 2019, **236**, 106599.

23 L. H. Madkour, *Pharm. Pharmacol. Int. J.*, 2018, **6**, 157–174.

24 E. Y. Lukianova-Hleb, X. Ren, R. R. Sawant, X. Wu, V. P. Torchilin and D. O. Lapotko, *Nat. Med.*, 2014, **20**, 778–784.

25 A. S. Kostyukov, I. L. Isaev, A. Ershov, V. Gerasimov, S. Polyutov and S. V. Karpov, *J. Phys. D Appl. Phys.*, 2022, **55**, 175401.

26 A. S. Kostyukov, I. L. Isaev, A. Ershov, V. Gerasimov, S. P. Polyutov and S. V. Karpov, *J. Phys. D Appl. Phys.*, 2022, **55**, 175402.

27 N. J. Halas, *Proceedings of the National Academy of Sciences*, 2019, **116**, 13724–13726.

28 S. Linic, P. Christopher and D. B. Ingram, *Nature materials*, 2011, **10**, 911–921.

29 C. Dhand, N. Dwivedi, X. J. Loh, A. N. J. Ying, N. K. Verma, R. W. Beuerman, R. Lakshminarayanan and S. Ramakrishna, *RSC Advances*, 2015, **5**, 105003–105037.

30 G. Yang, *Progress in Materials Science*, 2007, **52**, 648–698.

31 P. Lorazo, L. J. Lewis and M. Meunier, *Physical review letters*, 2003, **91**, 225502.

32 T. Tsuji, D.-H. Thang, Y. Okazaki, M. Nakanishi, Y. Tsuboi and M. Tsuji, *Applied Surface Science*, 2008, **254**, 5224–5230.

33 T. Tsuji, Y. Okazaki, Y. Tsuboi and M. Tsuji, *Japanese Journal of Applied Physics*, 2007, **46**, 1533–1535.

34 B. M. DeVetter, B. E. Bernacki, W. D. Bennett, A. Schemer-Kohrn and K. J. Alvine, *JoVE (Journal of Visualized Experiments)*, 2017, e56204.

35 B. J. Y. Tan, C. H. Sow, T. S. Koh, K. C. Chin, A. T. S. Wee and C. K. Ong, *The Journal of Physical Chemistry B*, 2005, **109**, 11100–11109.

36 D. Brodoceanu, C. Fang, N. H. Voelcker, C. T. Bauer, A. Wonn, E. Kroner, E. Arzt and T. Kraus, *Nanotechnology*, 2013, **24**, 085304.

37 C.-W. Kuo, J.-Y. Shiu, Y.-H. Cho and P. Chen, *Advanced Materials*, 2003, **15**, 1065–1068.

38 K. Loza, M. Heggen and M. Epple, *Advanced Functional Materials*, 2020, **30**, 1909260.

39 L. K. Sørensen, A. D. Utyushev, V. I. Zakomirnyi and H. Ågren, *Phys. Chem. Chem. Phys.*, 2021, **1**, 173–185.

40 L. S. Slaughter, W.-S. Chang, P. Swanglap, A. Tcherniak, B. P. Khanal, E. R. Zubarev and S. Link, *The Journal of Physical Chemistry C*, 2010, **114**, 4934–4938.

41 D. Chateau, A. Liotta, F. Vadcard, J. R. G. Navarro, F. Chaput, J. Lermé, F. Lerouge and S. Parola, *Nanoscale*, 2015, **7**, 1934–1943.

42 D. Château, S. David, G. Berginc, C. Lopes, F. Chaput, F. Lerouge, A. Désert, C. Andraud and S. Parola, *ACS Applied Nano Materials*, 2022, **5**, 3773–3780.

43 B. Yang, G. Chen, A. Ghafoor, Y. Zhang, Y. Zhang, Y. Zhang, Y. Luo, J. Yang, V. Sandoghdar, J. Aizpurua, Z. Dong and J. G. Hou, *Nature Photonics*, 2020, **14**, 693–699.

44 G. Mie, *Annalen der Physik*, 1908, **330**, 377–445.

45 B. T. Draine and P. J. Flatau, *J. Opt. Soc. Am. A*, 1994, **11**, 1491.

46 P. Waterman, *Proc. IEEE*, 1965, **53**, 805–812.

47 *Lumerical Solutions, "FDTD Solutions"*, 2020, www.lumerical.com/tcad-products/fdtd/.

48 *COMSOL Multiphysics*, 2015.

49 J. Hesthaven and T. Warburton, *Algorithms, Analysis, and Applications*, Springer, Berlin, 2007.

50 P. Drude, *Annalen der Physik*, 1900, **306**, 566–613.

51 W. Zhu, R. Esteban, A. G. Borisov, J. J. Baumberg, P. Nordlander, H. J. Lezec, J. Aizpurua and K. B. Crozier, *Nature Communications*, 2016, **7**, 1–14.

52 N. A. Mortensen, P. A. D. Gonçalves, F. A. Shuklin, J. D. Cox, C. Tserkezis, M. Ichikawa and C. Wolff, *Nanophotonics*, 2021, **10**, 3647–3657.

53 P. E. Stamatopoulou and C. Tserkezis, *Optical Materials Express*, 2022, **12**, 1869.

54 S. Palomba, L. Novotnyb and R. Palmer, *Opt. Commun*, 2008, **281**, 580–483.

55 A. Boardman, *Electromagnetic Surface Modes*, John Wiley & Sons Ltd, 1982.

56 N. Mortensen, S. Raza, M. Wubs, T. Sondergaard and S. Bozhev, *Nat. Commun.*, 2014, **5**, 3809.

57 W. P. Halperin, *Rev. Mod. Phys.*, 1986, **58**, 533–606.

58 E. D. Palik, *Handbook of optical constants of solids*, Academic Press, 1998.

59 S. Grimme, J. Antony, S. Ehrlich and H. Krieg, *J. Chem. Phys.*, 2010, **132**, 154104.

60 Zhao, L. Jensen and G. C. Schatz, *J. Am. Chem. Soc.*, 2006,

Physical Chemistry Chemical Physics Accepted Manuscript

128, 2911–2919.

61 H.-C. Weissker and X. Chitl Ló Pez-Lozano, *PCCP*, 2015, **17**, 28379–28386.

62 M. Stener, A. Nardelli, R. De Francesco and G. Fronzoni, *J. Phys. Chem. C*, 2007, **111**, 11862–11871.

63 J. Stanton and R. Bartlett, *J. Chem. Phys.*, 1993, **98**, 7029–7039.

64 E. Salpeter and H. Bethe, *Phys. Rev.*, 1951, **84**, 1232.

65 E. Runge and E. Gross, *Phys. Rev. Lett.*, 1984, **52**, 997.

66 P. Salek, O. Vahtras, T. Helgaker and H. Ågren, *J. Chem. Phys.*, 2002, **17**, 9630.

67 F. Della Sala, R. Pachter and M. Sukharev, *The Journal of Chemical Physics*, 2022, **157**, 1–7.

68 F. Della Sala, *J. Chem. Phys.*, 2022, **157**, 104101.

69 T. Giovannini, L. Bonatti, P. Lafiosca, L. Nicoli, M. Castagnola, P. G. Illobre, S. Corni and C. Cappelli, *ACS Photonics*, 2022, **9**, 3025–3034.

70 D. Beck, *Phys. Rev. B*, 1984, **30**, 6935.

71 D. V. Chulhai and L. Jensen, *J. Phys. Chem. A*, 2014, **118**, 9069–9079.

72 D. V. Chulhai and L. Jensen, *J. Phys. Chem. A*, 2015, **119**, 5218–5223.

73 Z. Hu, D. V. Chulhai and L. Jensen, *J. Chem. Theory Comput.*, 2016, **12**, 5968–5978.

74 Z. Hu and L. Jensen, *J. Chem. Theory Comput.*, 2018, **14**, 5896–5903.

75 V. I. Zakomirnyi, Z. Rinkevicius, G. V. Baryshnikov, L. K. Sørensen and H. Ågren, *The Journal of Physical Chemistry C*, 2019, **123**, 28867–28880.

76 T. Giovannini, M. Rosa, S. Corni and C. Cappelli, *Nanoscale*, 2019, **11**, 6004–6015.

77 P. Lafiosca, T. Giovannini, M. Benzi and C. Cappelli, *The Journal of Physical Chemistry C*, 2021, **125**, 23848–23863.

78 S. Morton and L. Jensen, *J. Chem. Phys.*, 2010, **133**, 15697–15703.

79 S. Morton and L. Jensen, *J. Chem. Phys.*, 2011, **135**, 134103.

80 J. L. Payton, S. M. Morton, J. E. Moore and L. Jensen, *J. Chem. Phys.*, 2012, **136**, 214103.

81 J. L. Payton, S. M. Morton, J. E. Moore and L. Jensen, *Acc. Chem. Res.*, 2014, **47**, 88–99.

82 X. Chen, J. E. Moore, M. Zekarias and L. Jensen, *Acc. Chem. Res.*, 2015, **6**, 8921.

83 L. Nicoli, P. Lafiosca, P. Grobas Illobre, L. Bonatti, T. Giovannini and C. Cappelli, *Frontiers in Photonics*, 2023, **4**, 1199598.

84 F. Gray., *Phys. Rev.*, 1916, **7**, 472–488.

85 R. R. Birge, *J. Chem. Phys.*, 1980, **72**, 5312–5319.

86 B. Thole, *Chem. Phys.*, 1981, **59**, 341–350.

87 L. Jensen, P.-O. Åstrand, K. O. Sylvester-Hvid and K. V. Mikkelsen, *J. Phys. Chem. A*, 2000, **104**, 1563–1569.

88 L. Jensen, O. H. Schmidt, K. V. Mikkelsen and P.-O. Åstrand, *J. Phys. Chem. B*, 2000, **104**, 10462–10466.

89 L. L. Jensen and L. Jensen, *J. Phys. Chem. C*, 2008, **112**, 15697–15703.

90 P. Pyykkö and M. Atsumi, *Chem. - A Eur. J.*, 2009, **15**, 186–197.

91 X. Chen, J. E. Moore, M. Zekarias and L. Jensen, *Nature communications*, 2015, **6**, 8921.

92 L. Jensen, P.-O. Åstrand and K. V. Mikkelsen, *Journal of Computational and Theoretical Nanoscience*, 2009, **6**, 270–291.

93 A. D. Buckingham, in *Permanent and Induced Molecular Moments and Long-Range Intermolecular Forces*, John Wiley & Sons, Ltd, 1967, pp. 107–142.

94 L. L. Jensen and L. Jensen, *Journal of Physical Chemistry C*, 2009, **113**, 15182–15190.

95 X. Chen, J. E. Moore, M. Zekarias and L. Jensen, *Nature Communications*, 2015, **6**, 8921.

96 B. Shanker and J. Applequist, *The Journal of Chemical Physics*, 1996, **104**, 6109–6116.

97 M. L. Olson and K. R. Sundberg, *The Journal of Chemical Physics*, 1978, **69**, 5400–5404.

98 Z. Rinkevicius, M. Kaminskas, P. Palevičius, M. Ragulskis, K. Bočkutė, M. Sriubas and G. Laukaitis, *Phys. Chem. Chem. Phys.*, 2022, **24**, 27731–27741.

99 A. H. Baker, E. R. Jessup and T. Manteuffel, *SIAM Journal on Matrix Analysis and Applications*, 2005, **26**, 962–984.

100 L. Silberstein, *The London, Edinburgh, and Dublin Philosophical Magazine and Journal of Science*, 1917, **33**, 521–533.

101 P. T. van Duijnen and M. Swart, *The Journal of Physical Chemistry A*, 1998, **102**, 2399–2407.

102 S. Luo, R. P. Misra and D. Blankschtein, *ACS Nano*, 0, **0**, null.

103 E. D. Larsson, P. Reinholdt, E. D. Hedegård and J. Kongsted, *The Journal of Physical Chemistry B*, 2023, **127**, 9905–9914.

104 J. M. Litman, C. Liu and P. Ren, *Journal of Chemical Information and Modeling*, 2022, **62**, 79–87.

105 C. Feng, J. Xi, Y. Zhang, B. Jiang and Y. Zhou, *Journal of Chemical Theory and Computation*, 2023, **19**, 1207–1217.

106 A. Mayer, *Phys. Rev. B*, 2005, **71**, 235333.

107 A. Mayer, *Phys. Rev. B*, 2007, **75**, 045407.

108 S. Zhao, H. Wei, P. Cieplak, Y. Duan and R. Luo, *Journal of Chemical Theory and Computation*, 2022, **18**, 3654–3670.

109 N. Legenski, C. Zhou, Q. Zhang, B. Han, J. Wu, L. Chen, H. Cheng and R. C. Forrey, *Journal of Computational Chemistry*, 2011, **32**, 1711–1720.

110 H. DeVoe, *The Journal of Chemical Physics*, 1964, **41**, 393–400.

111 H. DeVoe, *The Journal of Chemical Physics*, 1965, **43**, 3199–3208.

112 E. M. Purcell and C. R. Pennypacker, *Astrophys. J.*, 1973, **186**, 705.

113 M. A. Yurkin, in *Discrete dipole approximation*, Elsevier, 2023, p. 167–198.

114 J. I. Rodríguez, J. Autschbach, F. L. Castillo-Alvarado and M. I. Baltazar-Méndez, *The Journal of Chemical Physics*, 2011, **135**, 034109.

115 J. I. Rodríguez, M. I. Baltazar-Méndez, J. Autschbach and F. L. Castillo-Alvarado, *Eur. Phys. J. D*, 2013, **67**, 109.

Physical Chemistry Chemical Physics Accepted Manuscript

116 J. Dong, W. Zhang and L. Liu, *Opt. Express*, 2021, **29**, 7690–7705.

117 E. Ringe, M. R. Langille, K. Sohn, J. Zhang, J. Huang, C. A. Mirkin, R. P. Van Duyne and L. D. Marks, *The Journal of Physical Chemistry Letters*, 2012, **3**, 1479–1483.

118 U. Kreibig and M. Vollmer, *Optical Properties of Metal Clusters*, Springer Berlin Heidelberg, Berlin, Heidelberg, 1995, vol. 25.

119 J. Tiggesbäumker, L. Köller, K.-H. Meiwes-Broer and A. Liebsch, *Phys. Rev. A*, 1993, **48**, R1749–R1752.

120 N. G. Bastús, J. Comenge and V. Puntes, *Langmuir*, 2011, **27**, 11098–11105.

121 J. Piella, N. G. Bastús and V. Puntes, *Chemistry of Materials*, 2016, **28**, 1066–1075.

122 S. Link and M. A. El-Sayed, *The Journal of Physical Chemistry B*, 1999, **103**, 4212–4217.

123 J. A. Scholl, A. L. Koh and J. A. Dionne, *Nature*, 2012, **483**, 421–427.

124 S. L.K., D. Khrennikov, V. Gerasimov, E. A.E., P. S.P., S. Karpov and Å. H., *Phys. Chem. Chem. Phys.*, 2022, **24**, 24062–24075.

125 K. Ujihara, *Journal of Applied Physics*, 1972, **43**, 2376–2383.

126 A. Ershov, V. Gerasimov, A. Gavrilyuk and S. V. Karpov, *Appl. Phys. B*, 2017, **123**, 182.

127 F. Font and T. G. Myers, *J Nanopart Res*, 2013, **15**, 2086.

128 R. Kofman, P. Cheyssac, A. Aouaj, Y. Lereah, G. Deutscher, T. Ben-David, J. Penisson and A. Bourret, *Surface Science*, 1994, **303**, 231–246.

129 S. Zhu, T. Chen, Y. Liu, Y. Liu and S. Fung, *Journal of Nanoparticle Research*, 2012, **14**, 856.

130 S. Karimi, A. Moshaii, S. Abbasian and M. Nikkhah, *Plasmonics*, 2019, **14**, 851.

131 S. Babar and J. H. Weaver, *Appl. Opt.*, 2015, **54**, 477–481.

132 H.-J. Hagemann, W. Gudat and C. Kunz, *J. Opt. Soc. Am.*, 1975, **65**, 742–744.

133 K. M. McPeak, S. V. Jayanti, S. J. P. Kress, S. Meyer, S. Iotti, A. Rossinelli and D. J. Norris, *ACS Photonics*, 2015, **2**, 326–333.

134 P. B. Johnson and R. W. Christy, *Physical Review B*, 1972, **6**, 4370–4379.

135 W. Haiss, N. T. K. Thanh, J. Aveyard and D. G. Fernig, *Analytical Chemistry*, 2007, **79**, 4215–4221.

136 L. S. Slaughter, W.-S. Chang, P. Swanglap, A. Tcherniak, B. P. Khanal, E. R. Zubarev and S. Link, *The Journal of Physical Chemistry C*, 2010, **114**, 4934–4938.

137 *Gold nanorods spr vs. aspect ratio*, https://www.nanopartz.com/gold-nanoparticles-properties-nanorods-spr-aspect-ratio.asp.

138 O. Pena-Rodríguez, P. Diaz-Nunez, G. Gonzalez-Rubio, V. Manzaneda-Gonzalez, A. Rivera, J. M. Perlado, E. Junquera and A. Guerrero-Martínez, *Scientific Reports*, 2020, **10**, 5921.

139 A. Jakab, C. Rosman, Y. Khalavka, J. Becker, A. Trügler,

140 U. Hohenester and C. Sönnichsen, *ACS Nano*, 2011, **5**, 6880–6885.

140 A. L. González, C. Noguez, J. Beránek and A. S. Barnard, *The Journal of Physical Chemistry C*, 2014, **118**, 9128–9136.

141 D. C. Tzarouchis, P. Ylä-Oijala, T. Ala-Nissila and A. Sihvola, *Applied Physics A*, 2016, **122**, 298.

142 A. A. Ashkarran and A. Bayat, *International Nano Letters*, 2013, **3**, 50.

143 V. I. Zakomirnyi, I. L. Rasskazov, L. K. Sørensen, P. S. Carney, Z. Rinkevicius and H. Ågren, *Physical Chemistry Chemical Physics*, 2020, **22**, 13467–13473.

144 G. Mukhopadhyay and S. Lundqvist, *Il Nuovo Cimento B*, 1975, **27**, 1–18.

145 G. Mukhopadhyay and S. Lundqvist, *J. Phys. B*, 1979, **12**, 1297–1304.

146 E. Prodan and P. Nordlander, *Nano Letters*, 2003, **3**, 543–547.

147 E. Prodan, C. Radloff, N. Halas and P. Nordlander, *Science*, 2003, **302**, 419–422.

148 N. G. Khlebtsov, L. A. Dykman and B. N. Khlebtsov, *Russ. Chem. Rev.*, 2022, **91**, 2–29.

149 L. K. Sørensen, A. D. Utyushev, V. I. Zakomirnyi and H. Ågren, *PCCP*, 2021, **23**, 173–185.

150 L. Vegard, *Z. Physik*, 1921, **5**, 17–26.

151 A. R. Denton and N. W. Ashcroft, *Phys. Rev. A*, 1991, **43**, 3161–3164.

152 L. K. Sørensen, A. D. Utyushev, V. I. Zakomirnyi, V. S. Gerasimov, A. E. Ershov, S. P. Polyutov, S. V. Karpov and H. Ågren, *The Journal of Physical Chemistry C*, 2021, **125**, 13900–13908.

153 G. J. Lee, J. J. Kim, C. K. Hwangbo, J. Kim, I. Park and Y. P. Lee, *Journal of Nanoscience and Nanotechnology*, 2013, **13**, 568–571.

154 A. Mary, D. Koller, A. Hohenau, J. Krenn, A. Bouhelier and A. Dereux, *Physical Review B*, 2007, **76**, 245422.

155 J. Aizpurua, P. Hanarp, D. S. Sutherland, M. Käll, G. W. Bryant and F. J. García de Abajo, *Phys. Rev. Lett.*, 2003, **90**, 057401.

156 N. K. Geitner, A. Doepke, M. A. Fickenscher, J. M. Yarrison-Rice, W. R. Heineman, H. E. Jackson and L. M. Smith, *Nanotechnology*, 2011, **22**, 275607.

157 S. Ye, G. Marston, J. R. McLaughlan, D. O. Sigle, N. Ingram, S. Freear, J. J. Baumberg, R. J. Bushby, A. F. Markham, K. Critchley, P. L. Coletta and S. D. Evans, *Advanced Functional Materials*, 2015, **25**, 2117–2127.

158 Y.-l. Liu, J. Zhu, G.-j. Weng, J.-j. Li and J.-w. Zhao, *Microchimica Acta*, 2020, **187**, 1–24.

159 J. Chen, F. Saeki, B. J. Wiley, H. Cang, M. J. Cobb, Z.-Y. Li, L. Au, H. Zhang, M. B. Kimmey, X. Li and Y. Xia, *Nano Letters*, 2005, **5**, 473–477.

160 F. J. G. de Abajo, *The Journal of Physical Chemistry C*, 2008, **112**, 17983–17987.

161 L. K. Sørensen, D. E. Khrennikov, V. S. Gerasimov, A. E. Ershov, S. P. Polyutov, S. V. Karpov and H. Ågren, *The Journal*

of Physical Chemistry C, 2022, **126**, 16804–16814.

162 S. Peng, J. M. McMahon, G. C. Schatz, S. K. Gray and Y. Sun, *Proceedings of the National Academy of Sciences*, 2010, **107**, 14530–14534.

163 S. V. Karpov, V. S. Gerasimov, I. L. Isaev and V. A. Markel, *Physical Review B*, 2005, **72**, 205425.

164 W. T. Doyle, *Journal of the Optical Society of America A*, 1985, **2**, 1031.

165 V. Klimov, *Nanoplasmonics*, Jenny Stanford Publishing, 2014.

166 M. M. Miller and A. A. Lazarides, *J. Phys. Chem.*, 2003, **109**, 21556–21565.

167 M. M. Miller and A. A. Lazarides, SPIE Proceedings, 2005.

168 T. Jensen, M. Malinsky and C. H. R. van Duyne, *J. Phys.Chem. B*, 2000, **104**, 10549–10556.

169 M. D. Malinsky, K. L. Kelly, G. C. Schatz and R. P. V. Duyne, *Journal of the American Chemical Society*, 2001, **123**, 1471–1482.

170 N. Nath and A. Chilkoti, *Analytical Chemistry*, 2001, **74**, 504–509.

171 A. J. Haes, S. Zou, G. C. Schatz and R. P. V. Duyne, *The Journal of Physical Chemistry B*, 2004, **108**, 6961–6968.

172 A. Gole and C. J. Murphy, *Chemistry of Materials*, 2005, **17**, 1325–1330.

173 N. G. Khlebtsov, L. A. Trachuk and A. G. Mel'nikov, *Optics and Spectroscopy*, 2005, **98**, 77–83.

174 M. K. Hongxing Xu, *Sensors and Actuators B*, 2002, **87**, 244–249.

175 B. N. Khlebtsov and N. G. Khlebtsov, *Journal of Quantitative Spectroscopy and Radiative Transfer*, 2007, **106**, 154–169.

176 M. A. Garcia, *Journal of Physics D: Applied Physics*, 2011, **44**, 283001.

177 F. Qin, X. Cui, Q. Ruan, Y. Lai, J. Wang, H. Ma and H. Q. Lin, *Nanoscale*, 2016, **8**, 17645.

178 K. L. Kelly, E. Coronado, L. L. Zhao and G. C. Schatz, *The Journal of Physical Chemistry B*, 2002, **107**, 668–677.

179 C. Noguez, *The Journal of Physical Chemistry C*, 2007, **111**, 3806–3819.

180 J. J. Mock, D. R. Smith and S. Schultz, *Nano Lett.*, 2003, **3**, 4.

181 H. Chen, X. Kou, Z. Yang, W. Ni and J. Wang, *Langmuir*, 2008, **24**, 5233–5237.

182 A. D. McFarland and R. P. V. Duyne, *Nano Lett.*, 2003, **3**, 1057–1062.

183 F. Qin, X. Cui, Q. Ruan, Y. Lai, J. Wang, H. Ma and H. Q. Lin, *Nanoscale*, 2016, **8**, 17645.

184 C. Yu, R. Schira, H. Brune, B. von Issendorff, F. Rabilloud and W. Harbich, *Nanoscale*, 2018, **10**, 20821–20827.

185 A. Shafiqa, A. A. Aziz and B. Mehrdel, *Journal of Physics: Conference Series*, 2018, **1083**, 012040.

186 H. B. Jeon, P. V. Tsalu and J. W. Ha, *Scientific Reports*, 2019, **9**, 13635.

187 A. Yuksel, M. Cullinan, E. T. Yu and J. Murthy, *Journal of Quantitative Spectroscopy and Radiative Transfer*, 2020, **254**, 107207.

188 N. G. Khlebtsov, L. A. Dykman and B. N. Khlebtsov, *Russian Chemical Reviews*, 2022, **91**, RCR5058.

189 N. A. Mortensen, S. Raza, M. Wubs, T. Søndergaard and S. I. Bozhevolnyi, *Nature Communications*, 2014, **5**,.

190 B. S. Luk'yanchuk, A. E. Miroshnichenko, M. I. Tribelsky, Y. S. Kivshar and A. R. Khokhlov, *New Journal of Physics*, 2012, **14**, 093022.

191 G. Baffou, P. Berto, E. B. Ureña, R. Quidant, S. Monneret, J. Polleux and H. Rigneault, *ACS Nano*, 2013, **7**, 6478–6488.

192 A. D. Phan, T.-L. Phan and L. M. Woods, *Journal of Applied Physics*, 2013, **114**, 214306.

193 L. K. Sørensen, D. E. Khrennikov, V. S. Gerasimov, A. E. Ershov, M. A. Vysotin, S. Monti, V. I. Zakomirnyi, S. P. Polyutov, H. Ågren and S. V. Karpov, *Nanoscale*, 2022, **14**, 433–447.

194 A. P. Gavrilyuk and S. V. Karpov, *Applied Physics B*, 2009, **97**, 163–173.

195 A. Gavrilyuk and S. Karpov, *Applied Physics B*, 2011, **102**, 65–72.

196 A. Ershov, A. Gavrilyuk, S. Karpov and P. Semina, *Applied Physics B*, 2014, **115**, 547–560.

197 A. Alabastri, A. Toma, M. Malerba, F. De Angelis and R. Proietti Zaccaria, *ACS Photonics*, 2015, **2**, 115–120.

198 V. S. Gerasimov, A. E. Ershov, A. P. Gavrilyuk, S. V. Karpov, H. Ågren and S. P. Polyutov, *Optics Express*, 2016, **24**, 26851.

199 K. Bagi, in *Computational Modeling of Masonry Structures Using the Discrete Element Method*, IGI Global, 2016, pp. 90–102.

200 M. A. Yurkin and A. G. Hoekstra, *J. Quant. Spectrosc. Radiat. Transf.*, 2011, **112**, 2234–2247.

201 S. Sukhov, D. Haefner and A. Dogariu, *Phys. Rev. E Stat. Nonlin. Soft Matter Phys.*, 2008, **77**, 066709.

202 A. Amirjani, P. Z. Abyaneh, P. A. Masouleh and S. K. Sadrnezhaad, *Plasmonics*, 2022, **17**, 1095–1106.

203 J. Marcheselli, D. Chateau, F. Lerouge, P. Baldeck, C. Andraud, S. Parola, S. Baroni, S. Corni, M. Garavelli and I. Rivalta, *Journal of Chemical Theory and Computation*, 2020, **16**, 3807–3815.

204 C. E. Hofmann, F. J. García de Abajo and H. A. Atwater, *Nano Letters*, 2011, **11**, 372–376.

205 C. Mystilidis, X. Zheng, A. Xomalis and G. A. E. Vandenbosch, *Advanced Theory and Simulations*, 2023, **6**, 2200722.

206 M. I. Mishchenko, L. D. Travis and D. W. Mackowski, *J. Quant. Spectrosc. Radiat. Transf.*, 1996, **55**, 535–575.

207 M. I. Mishchenko, L. D. Travis and D. W. Mackowski, *J. Quant. Spectrosc. Radiat. Transf.*, 2010, **111**, 1700–1703.

208 Y.-l. Xu, *Applied Optics*, 1995, **34**, 4573.

209 Y.-L. Xu and B. Å. S. Gustafson, *J. Quant. Spectrosc. Radiat. Transf.*, 2001, **70**, 395–419.

210 Y.-L. Xu, *Math. Comput.*, 1996, **65**, 1601–1613.

211 Y.-L. Xu and B. Å. S. Gustafson, *J. Quant. Spectrosc. Radiat. Transf.*, 2001, **70**, 395–419.

212 "*LAMMPS Molecular Dynamics Simulator*, 2022, `www.`

`lammps.sandia.gov`.

213 J. Banhart, *Prog. Mater. Sci.*, 2001, **46**, 559–632.

214 G. Huttmann and R. Birngruber, *IEEE Journal of Selected Topics in Quantum Electronics*, 1999, **5**, 954–962.

215 G. Baffou, F. Cichos and R. Quidant, *Nature Materials*, 2020, **19**, 946–958.

216 A. E. Ershov, A. P. Gavrilyuk, S. V. Karpov and P. N. Semina, *Appl. Phys. B*, 2014, **115**, 547–560.

217 A. E. Ershov, V. S. Gerasimov, I. L. Isaev, A. P. Gavrilyuk and S. V. Karpov, *Chin. Physics B*, 2020, **29**, 037802.

218 A. E. Ershov, V. S. Gerasimov, A. P. Gavrilyuk and S. V. Karpov, *Appl. Phys. B*, 2017, **123**, 182.

219 N. G. Khlebtsov, L. Lin, B. N. Khlebtsov and J. Ye, *Theranostics*, 2020, **10**, 2067–2094.

220 M. Xu and L. V. Wang, *Review of Scientific Instruments*, 2006, **77**, 041101.

221 D. Razansky, J. Klohs and R. Ni, *Eur J Nucl Med Mol Imaging*, 2021, **48**, 4152–4170.

222 Y. Mantri and J. V. Jokerst, *ACS Nano*, 2020, **14**, 9408–9422.

223 N. Murugan, K. Chiotis, E. Rodriguez-Vieitez, L. Lemoine, H. Ågren and A. Nordberg, *Eur J Nucl Med Mol Imaging*, 2019, **46**, 1369–1382.

224 G. Kuang, N. A. Murugan, Y. Zhou, A. Nordberg and H. Ågren, *ACS Chemical Neuroscience*, 2020, **11**, 900–908.

225 Y. Zhou, G. Kuang, J. Li, C. Halldin, A. Nordberg, B. Långström, Y. Tu and H. Ågren, *RSC Adv.*, 2021, **11**, 3942–3951.

226 D. Karthigeyan, S. Siddhanta, A. H. Kishore, S. S. R. R. Perumal, H. Ågren, S. Sudevan, A. V. Bhat, K. Balasubramanyam, R. K. Subbegowda, T. K. Kundu and C. Narayana, *PNAS*, 2014, **111**, 10416–10421.

227 S. Nie and S. Emory, *Science*, 1997, **275**, 1102–1106.

228 A. Kopwitthaya, K. Yong, A. Kuzmin, W. Law, A. Pliss, L. A. Vathy, I. Roy and P. Prasad, *Plasmonics*, 2012, **8**, 313–318.

229 B. N. Khlebtsov, A. M. Burov, S. V. Zarkov and N. G. Khlebtsov, *Phys. Chem. Chem. Phys.*, 2023, **25**, 30903–30913.

230 Z. He, D. V. Voronine, A. M. Sinyukov, Z. N. Liege, B. Birmingham, A. V. Sokolov, Z. Zhang and M. O. Scully, *IEEE Journal of Selected Topics in Quantum Electronics*, 2017, **23**, 113–118.

231 R. M. Stöckle, Y. D. Suh, V. Deckert and R. Zenobi, *Chem. Phys. Lett.*, 2000, **318**, 131–136.

232 S. Duan, G. Tian, Y. Ji, J. Shao, Z. Dong and Y. Luo, *JACS*, 2015, **137**, 9515–9518.

233 J. Yang, C. Qian, X. Xie, K. Peng, S. Wu, F. Song, S. Sun, J. Dang, Y. Yu, S. Shi, J. He, M. J. Steer, I. G. Thayne, B.-B. Li, F. Bo, Y.-F. Xiao, Z. Zuo, K. Jin, C. Gu and X. Xu, *Light Sci Appl*, 2020, **9**, 81.

234 T. Ebbesen, H. Lezec, H. Ghaemi, T. Thio and P. A. Wolff, *Nature*, 1998, **391**, 667–669.

235 Z. M. Abd El-Fattah, V. Mkhitaryan, J. Brede, L. Fernandez, C. Li, Q. Guo, A. Ghosh, A. R. Echarri, D. Naveh, F. Xia, J. E. Ortega and F. J. Garcia de Abajo, *ACS Nano*, 2019, **13**, 7771–7779.

236 J. B. Pendry, L. Martín-Moreno and F. J. Garcia-Vidal, *Science*, 2004, **305**, 847–848.

237 F. Benz, M. K. Schmidt, A. Dreismann, R. Chikkaraddy, Y. Zhang, A. Demetriadou, C. Carnegie, H. Ohadi, B. de Nijs, R. Esteban, J. Aizpurua and J. J. Baumberg, *Science*, 2016, **354**, 726.

238 V. I. Zakomirnyi, I. L. Rasskazov, V. S. Gerasimov, A. E. Ershov, S. P. Polyutov, S. V. Karpov and H. Ågren, *Photonics and Nanostructures*, 2018, **30**, 50–56.

239 L. A. Jakob, W. M. Deacon, Y. Zhang, B. de Nijs, E. Pavlenko, S. Hu, C. Carnegie, T. Neuman, R. Esteban, J. Aizpurua and J. J. Baumberg, *Nature Communications*, 2023, **14**, 3291.

240 K. J. Webb, *Phys. Rev. B*, 2022, **106**, 155423.

241 A. Kostyukov, V. Gerasimov, A. Ershov, E. Bulgakov and A. Sadreev, *Optics and Lasers in Engineering*, 2023, **171**, 107797.

242 A. E. Ershov, A. P. Gavrilyuk, S. V. Karpov and P. N. Semina, *Applied Physics B*, 2013, **115**, 547–560.

243 V. I. Zakomirnyi, I. L. Rasskazov, V. S. Gerasimov, A. E. Ershov, S. P. Polyutov, S. V. Karpov and H. Ågren, *Photonics Nanostruct.*, 2018, **30**, 50–56.

244 I. L. Rasskazov, S. V. Karpov and V. A. Markel, *Opt. Lett.*, 2013, **38**, 4743–4746.

245 I. L. Rasskazov, S. V. Karpov and V. A. Markel, *Physical Review B*, 2014, **90**, 075405.

Physical Chemistry Chemical Physics Accepted Manuscript

Development of Discrete Interaction Models for Ultra-fine Nanoparticle Plasmonics

Lasse K. Sørensen, Valeriy S. Gerasimov, Sergey V. Karpov and Hans Ågren*

E-mail: lasse.kragh.soerensen@gmail.com

Physical Chemistry Chemical Physics

Data Availability Statement

No new data were created or analysed during this study except for Figure 32. Since similar data are shown in Figures 15,16,18,19,25 and 27 the data for Figure 32 are not publicly available.

Physical Chemistry Chemical Physics Accepted Manuscript